CARBON NANOPIPETTES FOR ADVANCED CELLULAR PROBING AND MICROINJECTION

Sean E. Anderson

A DISSERTATION

in

Mechanical Engineering and Applied Mechanics

Presented to the Faculties of the University of Pennsylvania in
Partial Fulfillment of the Requirements for the
Degree of Doctor of Philosophy

2015

Haim H. Bau
Supervisor of Dissertation
Professor, Mechanical Engineering and Applied Mechanics

Prashant Purohit
Graduate Group Chairperson
Associate Professor, Mechanical Engineering and Applied Mechanics

Dissertation Committee

Howard H. Hu Professor Mechanical Engineering and Applied Mechanics	Barry S. Cooperman Professor Chemistry	David Issadore Assistant Professor Bioengineering, Electrical and Systems Engineering

CARBON NANOPIPETTES FOR ADVANCED CELLULAR PROBING AND MICROINJECTION

To my parents, Andrew and Patricia.

In memory of Charles Agricola, Sean Finnegan, and Kevin Flatley.

Acknowledgements

I would like to first thank my advisor, Haim H. Bau, for his advice, wisdom, and trust over the past six years. This work would not have been completed without his guidance and experience. I would also like to thank my collaborators and committee members: Howard Hu, David Issadore, Barry Cooperman, Ian Farrell, Jill Venton, Hillary Rees, and Eve Privman.

This work was made possible by generous funding from the NIH (1R21EB016343-01), the Commonwealth of Pennsylvania under the Ben Franklin Technology Development Authority and the Nanotechnology Institute, the Department of Education GAANN program (P200A120237), the NSF (DMR08-32802), the NSEC - Nano/Bio Interface Center, the University of Pennsylvania Ashton Fellowship and the MEAM Departmental Fellowship. I would also like to acknowledge all of the labs that provided assistance with materials, equipment, or general advice, including D. Meaney, I. Dmochowski, G. Friedman, Y. Gogotsi, N. Dun, E. Brailiou, C. Lanci, G. Nonglaton, F. Vinet, P. Arratia, M. Yim, B. Kothman, and any other staff, students, professors, and post-docs who may have aided this work, including Maryeileen Banford Griffith, Sue Waddington-Pilder, Olivia Brubaker, Desirae Cesar, Nora Powell, Peter Litt, and Crystal Peterkin in the MEAM office.

I would also like to thank my labmates in the Bau and Hu labs, past and present, for their camaraderie throughout the years, including J. Yuan,

N. Schneider, B. Shaparenko, M. Norton, J. Grogan, J. Thompson, C. Liu, M. Qin, T. Gao, R. Hart, M. Sadik, H.-S. Chuang, R. Zhang, W. Lee, J. Song, C. Qi, S. Liao, S. Badin, E. Reeves, C. Robinson, R. Winter, E. Reilly, X. Qiu, D. Chen, M. Mauk, and X. Yan.

A PhD is a long and difficult endeavor, and I would not have made it through these past 6 years were it not for my amazing friends and family. My parents, Andrew and Patricia, my sister Lindsay, and my girlfriend Lauren, have always supported me in everything I do. My good friends Michael Artuso, Dana Rae Vessio, Anthony Orefice, Mark Miccio, Peter Fetzer, Allison Robb, Christopher Viemeister, Joseph Macaluso, Christopher Durando, Abigail Shaheen, Erica Tabakin, Karen Wolff, and James Hoepleman, among others, have always been there for me, no matter how busy we are or how infrequently we may see one another. Special thanks to Void and Venus, the men's and women's Ultimate teams at Penn, for giving me a family in Philadelphia and keeping me healthy in mind and body. I would also like to thank my cat, Miley, for being generally pleasant and meowing at me on occasion.

ABSTRACT

CARBON NANOPIPETTES FOR ADVANCED CELLULAR PROBING AND MICROINJECTION

Sean E. Anderson

Prof. Haim H. Bau

Carbon nanopipettes (CNPs) consist of a pulled-quartz micropipette with a thin layer of amorphous carbon deposited along its entire interior surface via chemical vapor deposition. The micropipette maintains a continuous fluidic pathway from its nanoscopic tip to its distal macroscopic end, while the insulated carbon film provides an electrical path to the tip that can be used as a working electrode. The quartz at the tip of the CNP can be chemically etched to expose a desired length of a carbon pipe to control the size and characteristics of the electrode. CNPs are inexpensive, batch-fabricated, and can be made hollow or solid. They can be used as nanoelectrodes, nanoinjectors, or both simultaneously, with improved durability and biocompatibility compared with glass micropipettes. Here, I will describe work stemming from CNP technology. We have developed an impedimetric AC technique for detecting cellular and nuclear penetration during microinjection and cellular probing with CNPs. The technique has submicron spatial and millisecond temporal resolution. Signal magnitude can be used to discern between penetration into the cytoplasm or nucleus, and using the CNPs as nanoelectrodes, we find a monotonic dependence of the

signal on penetration depth. The behavior of this system is well-predicted by an equivalent circuit model, and could be used to provide electrical feedback during single-cell microinjection, nanosampling, or electrochemical studies. Using solid CNP electrodes (CNPEs), we have also characterized CNPs for use in fast-scan cyclic voltammetry to measure neurotransmitter concentrations in the brain of *Drosophila melanogaster* (fruit fly). CNPEs are sharper and smaller than commonly used carbon-fiber microelectrodes (CFMEs), allowing them to penetrate the tough glial sheath of the fly brain and perform more localized measurements. CNPEs are also easier to batch fabricate and have better dimensional control than CFMEs. As a target biological application of microinjection, we are using injection of fluorescently labeled tRNA to monitor subcellular tRNA dynamics in real time. We have developed a simple model to capture trafficking dynamics, and fit our model to experimental data for the measurement of nuclear/cytoplasmic trafficking kinetics of tRNA during nutrient deprivation of mouse embryonic fibroblasts. This data confirms that cells have mechanisms for the regulation of tRNA transport, and suggests that we can use our microinjection technique to perform quantitative studies of tRNA trafficking. In order to facilitate microinjection studies such as these, we have developed an adaptable Matlab-based semi-automated injection system. We have incorporated our electrical feedback signal, with the goal of improving success rates and throughput of microinjection, while minimizing difficulty and user error.

Table of Contents

COPYRIGHT iii

Acknowledgements iv

ABSTRACT vi

Table of Contents viii

List of Figures xiii

Chapter 1: Introduction 1

1.1: Carbon Nanopipettes 1

1.2: Microelectrode Techniques for Single-Cell Studies 6

1.3: Microinjection for Single-cell Studies 25

Chapter 2: CNPs for Cellular Probing and Microinjection 29

2.1: Background 29

2.2: Experimental 30

2.2.1 Cell Culture and Imaging 30

2.2.2 CNP Fabrication 31

2.2.3 Impedance Measurements 32

2.2.4 Micromanipulation and Cell Experiments 34

2.3: Results and Discussion 37

2.3.1 A Simplified Circuit Model 37

2.3.2 Cell Penetration Detection 41

2.3.3 Continuous Flow Microinjection 48

2.3.4 Effect of Solution's Ionic Strength on ΔCeq 50

2.3.5 Pulsed Microinjection 51

2.3.6 Cytoplasm vs. Nucleus Penetration 56

2.3.7 Effect of Penetration Depth 58

2.3.8 Effect of Pressure on CNP Capillary Uptake 62

2.4: Conclusions 64

Chapter 3: CNP Electrodes (CNPEs) for Neurotransmitter Detection in *Drosophila Melanogaster* 67

3.1 Attribution 67

3.2: Background 68

3.3: Experimental 71

3.3.1 Solutions and Chemicals 71

3.3.2 Carbon Nanopipette Electrode Fabrication 72

3.3.3 Scanning Electron Microscopy 74

3.3.4 Instrumentation and Electrochemistry 75

3.3.5 Endogenous Dopamine Evoked by CsChrimson Channelrhodopsin Stimulation 76

3.3.6 Statistics 77

3.4: Results and Discussion 77

3.4.1 Fabrication of Carbon Nanopipette Electrodes 79

3.4.2 Comparison of CNPEs and CFMEs 80

3.4.3 CNPE Stability Over Time 87

3.4.4 CNPE Characterization 89

3.4.5 Measurements of Endogenous Dopamine in Drosophila Evoked by CsChrimson Stimulation 91
3.5: Conclusions 93
Chapter 4: Carbon Nanopipette-Based Automated Injection System 95
4.1: Attribution 95
4.2: Background 95
4.3: Experimental 99
4.3.1 Microinjection System and Computer Interface 99
4.3.2 CNP Fabrication 101
4.3.3 Matlab Code 101
4.3.4 Cell Culture 102
4.3.5 Microinjection Studies 102
4.3: Results and Discussion 106
4.4.1 Matlab Graphical User Interface 106
4.4.2. Calibration 108
4.4.3. Semi-Automated Cellular Microinjection with Electrical Feedback 112
4.4: Conclusions 117
Chapter 5: Microinjection of fl-tRNA for Studies of tRNA Subcellular Dynamics 121
5.1: Background 121
5.2: Experimental 124

5.2.1 Injection Method 124
5.3: Results and Discussion 125
5.3.1 Simple Kinetic Model for Membrane Transport 125
5.3.2 tRNA Dye Effects 128
5.3.3 tRNA Localization During Nutrient Deprivation 132
5.3.4 tRNA Localization During Cell Death 141
5.4: Conclusions 142
Chapter 6: Conclusions 144
6.1 Summary of Research 144
6.2 Future Possibilities 146
6.2.1 Automated Micropipette and Microelectrode Schemes 146
6.2.2 Functionalized Carbon Nanopipettes 147
6.2.3 Cellular Nanosampling 150
6.3.4 Multiplexed Electrodes 150
6.2.5 Process Modeling 151
6.2.6 tRNA Studies 153
6.2.7 Concentric Pipettes 154
Appendix A: CNP Fabrication Protocol 157
A.1 Materials 157
A.2 Method 157
A.2.1 Pulling Pipettes 157
A.2.2 Loading the Furnace 158

A.2.3 Furnace Operation 162
A.2.4 Etching Pipettes 168
Appendix B: CNP Characterization 171
B.1 Materials 171
B.2 Methods 171
B.2.1 Optical Microscopy 171
B.2.2 Electron Microscopy 172
B.2.3 Capacitance Characterization 176
Appendix C: Cell Culture Protocol 179
C.1 Materials 179
C.2 Methods 179
C.2.1 Sterile Technique 179
C.2.2 Media Preparation 181
C.2.3 Starting a Culture 181
C.2.4 Splitting Cells 182
C.2.5 Freezing Cells 183
Bibliography 184

List of Figures

Figure 1. CNPs. (A) Tip profile schematic. (B) Photo, dime for scale. (C) SEM of CNP tip profile with Carbon and Quartz clearly delineated. (D) SEM of CNP tip, 10^{o} off-axis. (E) SEM of CNP tip, axial view. Interface of (C) and (D) delineated with dotted line.....2

Figure 2. Voltage stability over time of a typical CNP in 100mM KCl solution. (a) CNP held stationary. (b) Signal during CNP motion, large spikes corresponding to movement on the order of 10's of microns with the micromanipulator. Standard deviations are shown. The CNP was pressurized to minimize fluctuations due to capillary rise. The system was shielded by a copper-mesh Faraday cage on a vibration-damping table. Measurements were carried out with a HEKA EPC 10 patch clamp amplifier with a headstage impedance of 0.5 GΩ.....3

Figure 3. Silver Deposition onto Carbon Nanopipettes. (A) SEM image of Ag-electroplated CNP under standard electroplating conditions. The electroplating solution is 1.0mM AgNO3 + 0.1M KNO3. Double-pulse method is used: E1=- 400mV, t1=20 ms, E2=- 30mV, t2=2000ms. (B) SEM image of the silver layer by double pulse potentiostatic deposition method in Technic Silver Cyless II solution, E1=-900mV, t1=400ms, E2= -600mV, t2=100s. (C) SEM back scattered image of silver deposited by pulse-current deposition at $200A/dm^2$, 10Hz, 2% duty cycle for 2s.....5

Figure 4. Current-potential curves for ideal (a) polarizable and (b) nonpolarizable electrodes. Dashed lines show behavior of actual electrodes that approach the ideal behavior over limited ranges of current or potential. Reproduced with permission, license number 360538108268 (Bard & Faulkner, 2000). 11

Figure 5. (a) A view of the differential capacitance in the Gouy-Chapman-Stern (GCS) model as a series network of Helmholtz- layer and diffuse-layer capacitances. (b) Potential profile through the solution side of the double layer according to GCS theory. Calculated for 10^{-2} M 1:1 electrolyte in water at 25°C. Reproduced with permission, license number 3605381008268 (Bard & Faulkner, 2000). 15

Figure 6. EDL capacitance (C_{EDL}) schematic. C_S is the Stern layer capacitance and C_{DL} is the diffuse layer capacitance.....16

Figure 7. Randle's circuit. C_{EDL} is the double layer capacitance, R_{CT} is the charge transfer resistance and R_S is the series or solution resistance. ...21

Figure 8. A schematic depiction of a CNP penetrating an adherent cell with the equivalent circuit model overlaid. HEKA EPC 10 patch clamp amplifier shown. C and R denote, respectively, capacitors and resistors. Subscripts o, i, and j designate, respectively, extracellular, intracellular, and inner-pipette circuit components. Superscripts designate the following: S - Stern layer (capacitance), s- series (resistance), d – diffuse layer, n – nuclear membrane, m – cellular membrane, t – charge

transfer. When modeling cytoplasm probing, the nuclear circuit elements (Cin and Rin) are omitted. (A) Complete circuit model. (B) Extracellular circuit approximation, only capacitors are included. (C) Intracellular (cytoplasm) circuit approximation, only capacitors are included. For cell probing without an internal fluid interface in the CNP the inner-pipette circuit components are not included. 40
Figure 9. Cell penetration impedance detection with an empty (pressurized to 300 kPa) CNP. (A) Micrographs of probing the cell cytoplasm. (i) The CNP is outside of the cell, (the nucleus outlined with a red line). (ii) The CNP has just contacted the cell membarne. (iii) The CNP lowered into the cell. (B) Probing the cell nucleus. (i) The CNP is outside of the cell, (the nucleus outlined with a red line). (ii) The CNP has just contacted the cell. (iii) The CNP has been lowered into the nucleus. Membrane contact/penetration is indicated by the bright spot at the pipette's tip due to the phase contrast filter, enhancing the contrast at the deformed membrane cleft. The CNP tip is identified with red arrows. Scale bar 10μm. (C) Schematics showing the CNP's tip positions: in the extracellular solution (EC, left), in the cell cytoplasm (C, middle), in the cell nucleus (N, right). (D) The measured capacitance as a function of time before, during, and after penetration into the cell cytoplasm and the nucleus. (E) The capacitance (Top) and the normalized capacitance time derivative (Bottom) as functions of time for cytoplasmic (C) and nuclear (N) probing events in different cells with the same CNP. (F) Re(Z) (Top) and its normalized time-derivative (Bottom) as functions of time for the same probing events in panel C. The dashed lines in (E) and (F) represent possible threshold values for identifying cytoplasmic and nuclear penetration..... 46
Figure 10. (A) The change in the CNP's capacitance, ΔC_{eq} (red trace, left axis), and the change in the CNP's resistance, ΔRe(Z) (blue trace, right axis), upon penetration into and withdrawal from various cells when operating in continuous-flow microinjection mode (pressure 1-4 kPa, and 100mM KCl injection solution). (B) The normalized change in capacitance $\Delta C_{eq}/C_0$ upon cell penetration as a function of the square root of the injection solution's (KCl) ionic strength. C_0 is the CNP capacitance when in the extracellular solution. The symbols represent the average of N measurements and the vertical bars represent one standard deviation. The solid line is a linear best-fit. R^2=0.80. Each data point corresponds to a distinct CNP. All the data was acquired from the same cell culture on the same day, with the exception of the data point to the far right, which was obtained with two different CNPs and two different cell petri dishes. 49
Figure 11. Concurrent penetration and microinjection detection. Control pressure: 10hPa. Injection pulse: 125hPa for 0.3s. (A) Micrographs of the cell: CNP in extracellular solution (i); CNP's tip inside the cytoplasm (ii);

injection of 150mM KCl into the cytoplasm (iii-iv); CNP tip withdrawn from the cell (v). (B) ΔCeq (lower red trace) and ΔRe(Z) (upper blue trace) as functions of time during cytoplasmic penetration and microinjection events. (C) Micrographs of the CNP tip position relative to the cell nucleus: CNP outside (above) the cell (i); CNP's tip in the nucleus (ii); nucleus is injected with 150mM KCl solution (iii-iv); CNP withdrawn from the cell (v). (D) ΔCeq (lower red trace) and ΔRe(Z) (upper blue trace) as functions of time during the nuclear penetration and injection. The cell (A) and the nucleus (C) are outlined with dotted lines for better visibility. 53

Figure 12. Distribution histograms of cellular probing data (bars) for cytoplasm (N=138) (A) and nucleus (N=133) (B) with Gaussian fits (solid lines). (C) Comparison between the Gaussian fits from (A) and (B). The y-axis data is normalized to produce a probability density function and the x-axis is the square root of the capacitance change. 57

Figure 13. The real part of the change in the impedance ΔRe(Z) (blue triangles, empty CNP, n=10), ΔC_{eq} (red hollow squares, empty CNP, N=10), and ΔC_{eq} (red stars, liquid-filled CNP, N=1) are depicted as functions of the cell penetration depth (d μm) into the cytoplasm. The symbols and lines represent, respectively, experimental data and theoretical predictions. 60

Figure 14. The equivalent CNP's capacitance Ceq as a function of P^{-2}, where P is the control pressure. The symbols and the line represent, respectively, experimental data and the best linear fit. 64

Figure 15.Preliminary CNP FSCV data, 5μM dopamine in PBS1X. Dopamine introduced at t=10s, and stopped at t=25s. (A) Color plot of dopamine detection, red is the oxidation current, blue is the reduction current. (B) Sample cyclic voltammogram demonstrating peaks near +400mV and -75mV vs. Ag/AgCl/Cl^-. (C) Oxidative peak current over time, which is proportional to dopamine concentration. 78

Figure 16. Carbon Nanopipette Electrodes (CNPE). (A) A schematic of the CNPE fabrication process. (i) Quartz/glass pipette is pulled to form a template. (ii) The pulled pipette is placed in a furnace in the presence of precursor hydrocarbons and carbon is deposited selectively along the pipette's interior surface for a sufficient amount of time until the tip is sealed with carbon. No catalyst was used. (iii) The glass/quartz at the tip is wet-etched to expose a desired length of the underlying carbon. (B) SEM image of the CNPE tip profile. (C) Enhanced SEM view of the quartz/carbon interface. (D) Enhanced SEM view of the CNPE tips. (i) Tip diameter 50 nm. (ii) Tip diameter 365 nm (same CNPE as in (B) and (C)). The tip and edges appear brighter due to SEM charging effects. 80

Figure 17. Example data for a 150 μm long CNPE (red dashed line) and a 50 μm long CFME (black line) with the 1.0 V and 1.3 V waveforms. Background-subtracted cyclic voltammograms for 1 μM dopamine are

shown for (A) the 1.0 V waveform and (B) the 1.3 V waveform. Normalized current versus time plots at peak oxidation voltage for (C) the 1.0 V and (D) 1.3 V waveforms. 82
Figure 18. Example data of octopamine and serotonin detection using a 150 μm long CNPE. Background-subtracted cyclic voltammograms for 1mM octopamine are shown for (A) the 1.3 V (Dopamine) waveform and (B) the positive waveform, 0.1 to 1.4 V and back at 600 V/s. Background-subtracted cyclic voltammograms for 1 μM serotonin are shown for (C) the 1.3 V (dopamine) waveform and (D) the serotonin waveform, 0.1 to 1.0 to -0.1 to 0.1 V at 1000 V/s. The insets show current versus time plots of the main peak oxidation currents for each waveform.....86
Figure 19. Stability of CNPEs over three hours at the 1.0 V waveform (black circles) and 1.3 V waveform (red triangles) (n=4 electrodes). Insets show example cyclic voltammograms for both waveforms at initial measurements and after three hours. 89
Figure 20. Electrochemcial characterization of CNPE. (A) Normalized peak oxidative current for 1 μM dopamine vs scan rate. The plot is linear for CNPEs (n=4) showing the kinetics are adsorption-controlled. (B) Peak oxidative current vs concentration (n=3). CNPEs show a linear response in current up to 10 μM. Solid lines are best fits of the data. 90
Figure 21. Example CNPE measurement of endogenous dopamine evoked by a 5 second continuous red light stimulation. (A) Background-subtracted cyclic voltammagram of evoked dopamine. (B) SEM of a short CNP like the one used *in vivo*. (C) Color plot showing stimulated dopamine in a *Drosophila* larval ventral nerve cord. Red light was applied from 5 to 10 seconds. (D) Extracellular concentration of dopamine over time as red light stimulates release (red line). 92
Figure 22. Semi-automated CNP injection system overview, depicting the interaction between the GUI, amplifier, microinjection equipment, and microscope imaging.....100
Figure 23. Microinjection logic flow chart. “Cap.” is an abbreviation for capacitance, and “Trav.” is an abbreviation for traveling. Abnormal and Normal refer to the capacitance relative to the reference extracellular state. A large deviation from this reference state is indicative of pipette breakage or clogging. 106
Figure 24. Matlab-based semi-automated GUI. Various sections are outlined in color for emphasis. (A) Camera controls for gain, contrast, and image/video acquisition. (B) Live camera window with cells and CNP visible. (C) Injection parameters (substrate datum, speed, angle, pull-back delay). (D) Pump parameters for control pressure, injection pressure, injection time, and clean function. (E) Information display board and additional connection parameters (COM ports etc…).....108
Figure 25. GUI calibration and injection routine. (A) Sub-GUI for Injection. (B) X/Y calibration step 1: the pipette is moved to the upper right of the

field of view and the user identifies the location of the pipette tip. (C) X/Y calibration step 2, the pipette is moved to the lower left of the field of view and the user selects the tip via crosshair. Red arrows in (B) and (C) indicate crosshair and tip location. (D) After calibration the user selects the injection points via mouse crosshair. Injection points are tagged with a red star. (E) Z-datum injection with optimized injection path shown. Numbers have been reproduced and enlarged for visibility. (F) Microinjection with electrical feedback. Cell numbers have been reproduced and enlarged for visibility. Inset displays the capacitance measurement (red star) as well as the extracellular capacitance threshold (blue line). When the capacitance drops below a percentage threshold below the blue line, injection will be triggered. 111

Figure 26. Semi-automated cell injection with electrical feedback. (A) Injection coordinates selected for the three numbered cells. (B) The injection path during the automated microinjection is shown with a red line. The capacitance is monitored in the display window in the lower right of the panel. (C)(i) Capacitance trace as a function of time during automated microinjection. A clear capacitance drop is seen for each of the three cells. Arrows indicate the point of penetration for each of the three cells (numbered). (ii) Inset shows three cells fluorescing after successful injection with FITC-dextran. 116

Figure 27. Spinning disc confocal microscopy with stage incubation and microinjection capabilities. 125

Figure 28. tRNA dye effects. (A) MEF cells coinjected with 25μM CCT Cy3 tRNA and (B) 25μM CCG Rhodamine tRNA. Both CCT and CCG are Arginine isoacceptors. (C) MEF cells coinjected with 25μM Cy3 dye (no tRNA) and (D) 25μM Rhodamine 110 dye (no tRNA). (E) MEF cells coinjected with 12.5 μM Cy3 bulk tRNA and (F) 12.5 μM Rhodamine bulk tRNA. (G) MEF cells coinjected with 25μM Phenylalanine Alexa 555 tRNA and (H) 25μM Phenylalanine Alexa 488 tRNA. 129

Figure 29. Rhodamine-labeled bulk tRNA localization during nutrient deprivation of MEF cells. (A) Immediately after microinjection with tRNA. (B) 30 minutes after microinjection w/ tRNA. (C) Higher resolution image after localization. This is a different cell than the one pictured in (A) and (B), but it is from the same experiment. tRNA accumulates in nuclear periphery, granular regions in the nucleus, and in fibrous regions in the cytoplasm believed to be endoplasmic reticulum or microtubules. We can observe localization and trafficking dynamics. 133

Figure 30. tRNA Nutrient Deprivation Kinetics. (A) Sample curve fit of the ratio between nuclear and cytoplasmic mean intensity during nutrient deprivation and tRNA nuclear accumulation. Symbols represent experimental data and the red line is the Mathematica curve fit to our model. (B) Natural logarithm of the kinetic parameters extracted from

nutrient deprivation. Histogram represents experimental data for k_{in} and k_{out} for both Rhodamine (magenta and green, respectively), and Cy3 (blue and red, respectively). The curves are the best Gaussian fit to a lognormal distribution. The triangles correspond to k_{in}, and the crosses to k_{out} for the two dyes, N=34. The k_{in} distribution is shifted to the right relative to the k_{out} distribution indicating nuclear accumulation. (C) Histogram of the ratio of k_{in}/k_{out} for individual cells during the same nutrient deprivation experiment in (B) for Rhodamine (red) and Cy3 (blue). k_{in}/k_{out} values >1 indicate nuclear accumulation. Curves represent best Gaussian fit for Rhodamine (blue asterisks), and Cy3 (red crosses). 137

Figure 31. Reversibility of tRNA localization during nutrient deprivation. (A) MEF cells coinjected with 25μM Cy3 bulk tRNA and (B) 25μM Rhodamine 110 bulk tRNA. Cell of interest is indicated with a white arrow pointing towards its nucleus. (i) Cells one hour after injection in normal media. (ii) After one hour in normal media, the cells are switched to nutrient-deprived (amino-acid free DMEM) media for 50 minutes. Some nuclear localization is seen. (iii) Media replenished and within 10 minutes the tRNA is seen redistributing. (C) Ratio of nuclear to cytoplasmic mean intensity for the cell indicated with the white arrow in (A) and (B) for Rhodamine (green) and Cy3 (orange). The ratio was taken after 60 minutes in normal media ("Normal"), after 50 minutes in amino-acid deprived media ("Deprived"), and 6 minutes after media replenishment ("Replenished"). 140

Figure 32. tRNA accumulates in the cell nucleus during cell death. (A) HeLa cells, injected with Cy5-tRNA at time 0. (B) Within 15 minutes, tRNA has clearly accumulated in the nucleus. (C) Within 25 minutes, signs of cell death are present, including shriveling, shrinking and rounding of the nuclear profile, and membrane blebbing. 142

Figure 33. Concentric CNP concept. Not to scale. 155

Figure 34. Sutter P-2000 Pipette Puller. 158

Figure 35. Loading the CVD Furnace. (A) Micropipettes, tweezers and quartz boats appropriately stacked and ready to load. (B) Loading micropipettes into boat. (C) Adjusting micropipettes in the boat to the desired location, (D). (E) CVD Furnace with inlet/outlet couplings, boat, and welding rod labeled. 161

Figure 36. (A) Vent status light and gas tanks (Argon and Methane are used). (B) Flow control panel and furnace controller. Settings shown are during CVD of carbon. 168

Figure 37. CNP Etch Process. (A) Researcher wearing appropriate PPE working in fume hood with Hydrofluoric Acid. (B) Etch setup. Manipulator holds a friction grip with 14 CNPs and lowers them into a container of HF Acid. A warning sign is present to notify other workers in the lab of the presence of HF. 170

Figure 38. Optical microscopy characterization of CNPs. (A) CNP tip with quartz and carbon labeled. (B) Higher magnification micrograph of same CNP in (A), with quartz/carbon interface labeled. 172
Figure 39. Effect of accelerating voltage on charging and surface detail. Fouled CNP tip shown. (A) 30 keV. (B) 15 keV. (C) 5 keV. The low accelerating voltage provides the best surface detail and least amount of charging. 173
Figure 40. Sample CNP SEM image of a ~10μM exposed CNPE tip of 180nm tip diameter. There is clear contrast between the bright quartz and dark carbon. 176
Figure 41. Capacitance characterization setup. A CNP is mounted on a HEKA headstage which is mounted on a micromanipulator which is mounted on an inverted microscope. The pipette coupling is connected to a microinjection pump and the ground is connected to a reference/counter electrode in solution. The CNP tip is immersed in a petri dish filled with PBS or other simple salt solution such as KCl. 178

Chapter 1: Introduction

1.1: Carbon Nanopipettes

Carbon Nanopipettes (CNPs) were recently developed at the University of Pennsylvania (Kim, Murray, & Bau, 2005; Schrlau, Falls, Ziober, & Bau, 2008; Singhal et al., 2010). These nanopipettes consist of a pulled-quartz micropipette with a thin layer of carbon deposited along its interior via chemical vapor deposition (CVD) with a carbon precursor gas. The carbon precursor decomposes at high temperatures and selectively deposits on the interior of the quartz micropipettes due to a confinement effect (Singhal et al., 2010). The quartz at the tip can be wet-etched away in buffered Hydrofluoric acid to leave only the carbon at the tip exposed. The tip dimensions are controlled by pipette puller parameters, the carbon thickness is controlled via CVD parameters, and the exposed electrode length is linearly related to the etch time due to the linearly increasing quartz thickness near the tip and the isotropic etch. The result is a nanoscopic, hollow or solid carbon electrode incorporated within a macroscopic handle. There is simple access for electrical connections to the conductive carbon layer, as well as for fluidic connections from the distal end. CNPs are batch fabricated, and compatible with commercial electrophysiology equipment such as micromanipulators, patch-clamp amplifiers, and all standard micropipette fittings. CNPs are depicted in Figure 1.

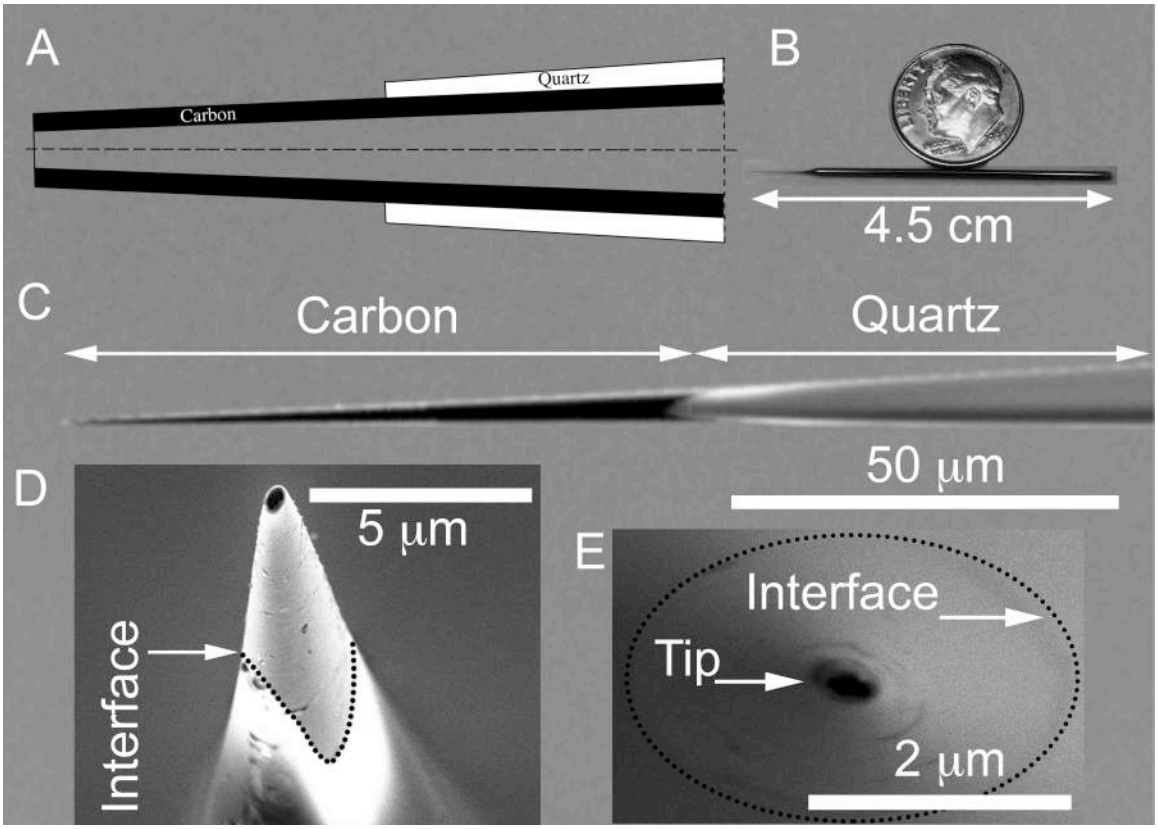

Figure 1. CNPs. (A) Tip profile schematic. (B) Photo, dime for scale. (C) SEM of CNP tip profile with Carbon and Quartz clearly delineated. (D) SEM of CNP tip, 10° off-axis. (E) SEM of CNP tip, axial view. Interface of (C) and (D) delineated with dotted line.

CNPs have two primary target applications: cellular microinjection and microelectrode techniques. It has been demonstrated that CNPs are smaller, less invasive, less susceptible to clogging, and more biocompatible than available glass micropipettes (Singhal et al., 2010). This gives them a distinct advantage for microinjection, as demonstrated by the characterization of Ca^{2+} release signals in breast cancer cells (Schrlau, Brailoiu, et al., 2008) and the injection of *C. Elegans* embryos, which are

tough to inject with glass micropipettes (Brennan et al., 2013). The most interesting feature of CNPs however, is that the carbon can be used simultaneously or independently as an electrode. To date, it has been demonstrated that CNPs are capable of recording cell membrane potentials for detection of cellular penetration, and monitoring of cell polarization responses to external stimuli (Schrlau, Dun, & Bau, 2009). Potentiometry with CNPs is not ideal however, and is very noisy. Even with a high-impedance measurement system, the potential tends to fluctuate by several mV, and was seen to be affected by capillary rise in the pipette and movement of the pipette in solution (Figure 2).

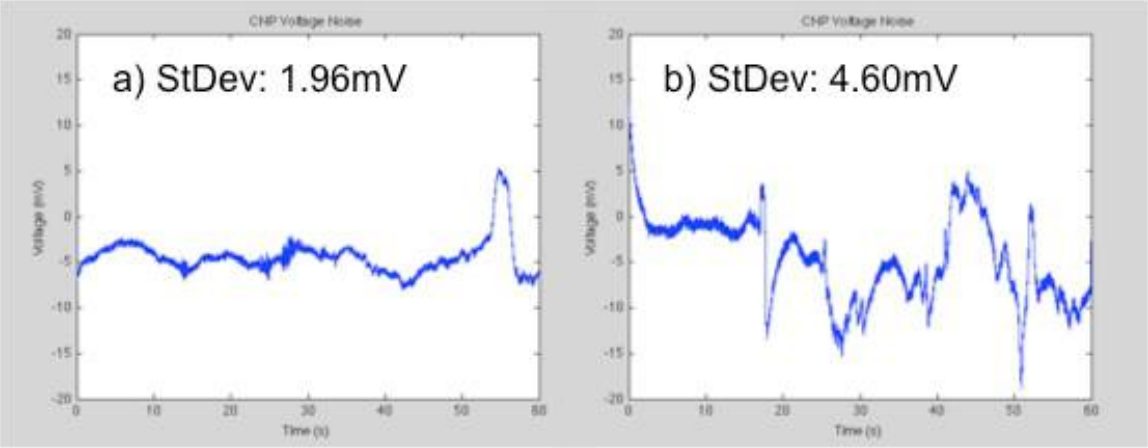

Figure 2. Voltage stability over time of a typical CNP in 100mM KCl solution. (a) CNP held stationary. (b) Signal during CNP motion, large spikes corresponding to movement on the order of 10's of microns with the micromanipulator. Standard deviations are shown. The CNP was pressurized to minimize fluctuations due to capillary rise. The system was shielded by a copper-mesh Faraday cage on a vibration-damping table. Measurements were carried out with a HEKA EPC 10 patch clamp amplifier with a headstage impedance of 0.5 GΩ.

Patch pipettes by comparison are reported to be stable within 1mV over long times and in response to electrode movement due to the stabilized Ag/AgCl/Cl^- interface within the pipette. Electrodeposition of platinum black onto carbon nanopipettes improved the potentiometric characteristics of CNPs, allowing for them to be used in Scanning Electrochemical Microscopy (SECM) (Hu et al., 2013). Electroplating is an attractive option for a number of applications, because CNPs can be used as a template to produce nanoscale metallized electrodes with the same tunable geometry and form-factor as CNPs. Metallized electrodes may have improved kinetics (Polk, Stelzenmuller, Mijares, MacCrehan, & Gaitan, 2006), desirable surface chemistry (Katz & Willner, 2003), and characteristics for surface-enhanced Raman Spectroscopy (Meyer & Smith, 2011; Singhal et al., 2011; Vitol et al., 2009). We have experimented with silver electrodeposition onto CNPs using both double-pulse, and pulsed current methods, demonstrating good surface nucleation density and size distribution (Figure 3). Even with electroplating however, CNPs are not ideal for potentiometry, and nanoelectrodes typically fare better for SECM when a redox mediator was used in solution in an amperometric method (Sun et al., 2008).

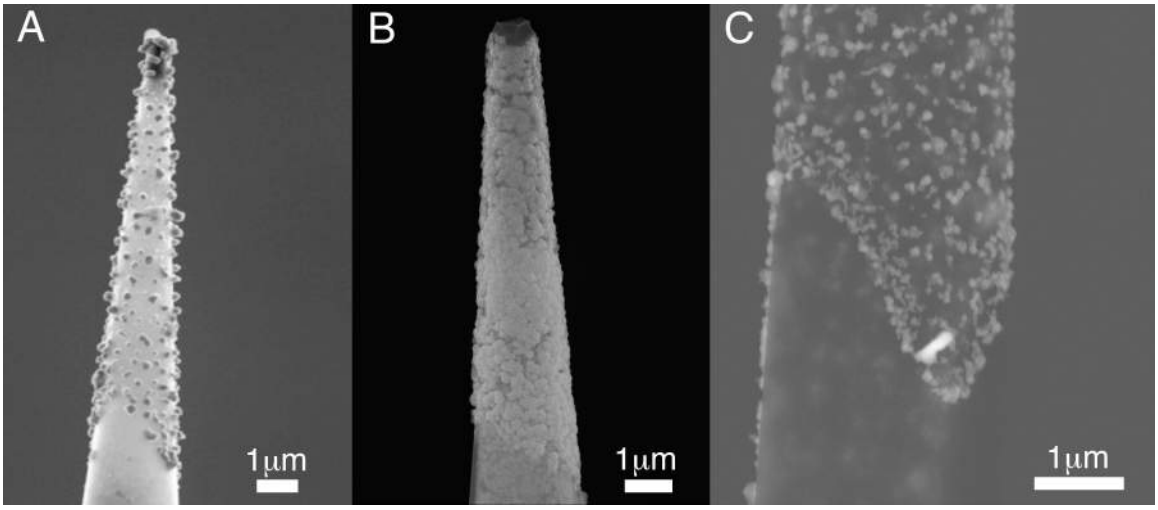

Figure 3. Silver Deposition onto Carbon Nanopipettes. (A) SEM image of Ag-electroplated CNP under standard electroplating conditions. The electroplating solution is 1.0mM AgNO3 + 0.1M KNO3. Double-pulse method is used: E1=- 400mV, t1=20 ms, E2=- 30mV, t2=2000ms. (B) SEM image of the silver layer by double pulse potentiostatic deposition method in Technic Silver Cyless II solution, E1=-900mV, t1=400ms, E2= -600mV, t2=100s. (C) SEM back scattered image of silver deposited by pulse-current deposition at 200A/dm², 10Hz, 2% duty cycle for 2s.

The potentiometric instability of CNPs can be explained by the carbon's inert nature, small electrode size, lack of redox species in solution, and sensitivity of the electrode to the local environment. This results in a large junction impedance (even relative to a high impedance headstage) and poor noise characteristics. Carbon performs much better as an ideally polarizable working electrode for amperometric studies. An alternative method for using CNPs as electrodes in the absence of redox species is to use AC techniques. A polarizable electrode in the absence of Faradaic reactions acts like a capacitor, and at high frequencies relatively large charging

currents are passed that can be measured by an amplifier even for nanoscale electrodes. This current response can be used to calculate a complex impedance of the system which is highly sensitive to the local electrode environment (Katz & Willner, 2003). This has motivated the exploration of electrochemical methods and alternative techniques for obtaining useful information from CNP electrodes, using them as either amperometric probes (working electrodes) to study cellular redox species, or with AC techniques that provide enhanced signal magnitude in the absence of redox species. The following section presents a thorough overview of basic electrochemistry and microelectrode principles in the context of single-cell studies.

1.2: Microelectrode Techniques for Single-Cell Studies

In recent years, there has been a growing interest in studying single cells to better understand cellular and sub-cellular processes that otherwise may be obscured by cells' heterogeneity. Micro- and nano-electrodes are effective tools for such studies since they are minimally invasive, causing small system perturbation, and provide fast time response, high spatial resolution, small ohmic potential drop compared to sharp/patch electrodes, and improved signal to noise ratio (Bard & Faulkner, 2000). Micro and nano electrodes can be used to detect various electrochemically-active, biologically-important species, such as catecholamines (neurotransmitters), oxygen, nitric oxide, reactive oxygen species (ROS), and reactive nitrogen species (RNS), under physiological conditions (Nebel, Grutzke, Diab, Schulte, & Schuhmann,

2013). Advancements in micro/nanoelectrode fabrication methods (W. H. Huang, D. W. Pang, H. Tong, Z. L. Wang, & J. K. Cheng, 2001; Kim et al., 2005; Lin et al., 2012; Schrlau, Falls, et al., 2008; Singhal et al., 2010), improvements in measurement techniques (Amemiya, Bard, Fan, Mirkin, & Unwin, 2008; Bergner, Vatsyayan, & Matysik, 2013; P. Chen & Gillis, 2000; Gillis, 2000; Katz & Willner, 2003), and novel surface functionalizations (Actis, Mak, & Pourmand, 2010; Katz & Willner, 2003; Randviir & Banks, 2013), are providing opportunities to study various single-cell characteristics (Fritzsch, Dusny, Frick, & Schmid, 2012; D. Wang & Bodovitz, 2010).

Until recently, most electrochemical measurements of single-cells have been carried out with sensors positioned in the extracellular solution to monitor, among other things, cellular respiration and exocytosis of neurotransmitters, carry out scanning electrochemical microscopy (SECM), and form patch-clamps to probe ionic channels (Adams, Puchades, & Ewing, 2008; Amatore et al., 2006; Cahill et al., 1996; Lindau & Neher, 1988; Mellander, Cans, & Ewing, 2010; Sun et al., 2008; Sun, Laforge, & Mirkin, 2007; Venton & Wightman, 2003; W. Wang et al., 2009; Wightman, May, & Michael, 1988; Zhao et al., 2008). Sharp-like electrodes with ohmic conductivity that can carry out electrochemical measurements inside the cell and in organelles provide new opportunities (Sun et al., 2008).

Carbon nanopipettes (CNPs) are one example of such an intracellular probe. To better understand how to best use CNPs for microelectrode

techniques, it is important to understand fundamentals of electrochemistry and microelectrodes. The majority of the following review is from the following references (Bard & Faulkner, 2000; Probstein & Brenner, 2013).

Electrochemistry is a broad and complex field, encompassing the interactions between electric fields, current, and chemical species. While electrochemical methods do not solely apply to solid/liquid interfaces, the main medium that will be considered here will be that of solid electrodes immersed in an electrolyte solution. This describes the typical CNP environment, where it is used as an electrode in a liquid environment such as a cell buffer solution. An electrolyte is any liquid solution that has free ions that allow it to be electrically conductive. The most common example is a simple salt solution. Salts will ionize when dissolved in water, splitting into charged components (Ex: $KCl \rightarrow K^+ + Cl^-$). Since the individual ions are charged and mobile they can carry current. If electrodes are immersed in an electrolyte they will be free to interact with any of the ions in solution, and there will be a characteristic potential established due to the interface of the metal/solution. This equilibrium potential is given by the Nernst Equation, Equation 1.

$$E = E^{0\prime} + \frac{RT}{nF} ln\left(\frac{{C_O}^*}{{C_R}^*}\right)$$

Equation 1.

Here, E is the potential of the electrode, Eo' is the formal potential, R is the ideal gas constant, T is the absolute temperature, n is the number of

electrons transferred in the redox reaction, F is Faraday's constant, C_O^* is the concentration of the oxidized species in the bulk, and C_R^* is the concentration of the reduced species in the bulk. The formal potential, $E^{0'}$, is a tabulated value based on the electrode material and the electrolyte solution, and it accounts for activity coefficients which are difficult to measure experimentally.

If a potential difference is imposed upon two electrodes, there will be a balance of charge, with equal and opposite charges accumulating at each electrode. If the electrodes are of two different surface areas, then they will have different charge densities. There will be a potential drop from the working electrode to the bulk solution, a potential drop across the solution due to its conductivity, and a potential drop from the solution to the counter electrode. These potential drops are dependent on electrode material, electrode/cell geometry, applied potential, and the electrolyte composition. Species concentration profiles will change as they are oxidized or reduced, or if the applied potential is changed, both due to charge redistribution and a change in redox kinetics. Thus when studying an electrochemical reaction, it is important to have a reference electrode to isolate the potential drop across the working electrode since the cell potential is not distributed evenly. Reference electrodes have potentials that are very stable over a small range of currents, and so they can be used to specify the potential distribution of each electrode relative to a standard. The general configuration of a typical

three-electrode cell is that there is a working electrode where the reaction of interest takes place. The working electrode passes current through the solution to the counter-electrode, which is a large inert electrode that balances the charge and the electrochemical reaction that occurs on the working electrode. Counter electrodes are typically selected such that they will not produce any species that will interfere with the working electrode. A platinum wire is a common counter-electrode. The reference electrode is placed in close proximity to the working electrode to minimize error due to the solution conductivity, and potential measurements are made between the reference and working electrode. This system allows for the currents to be measured through the working/counter electrodes and potentials to be measured across the working/reference electrodes such that a reaction at a single electrode surface can be studied. The most common reference electrodes are the NHE (normal hydrogen electrode, the universal standard), SCE (saturated calomel electrode), and silver chloride electrode, which are generally selected for their nonpolarizability. Ideally polarizable and nonpolarizable electrode behavior is shown in Figure 4.

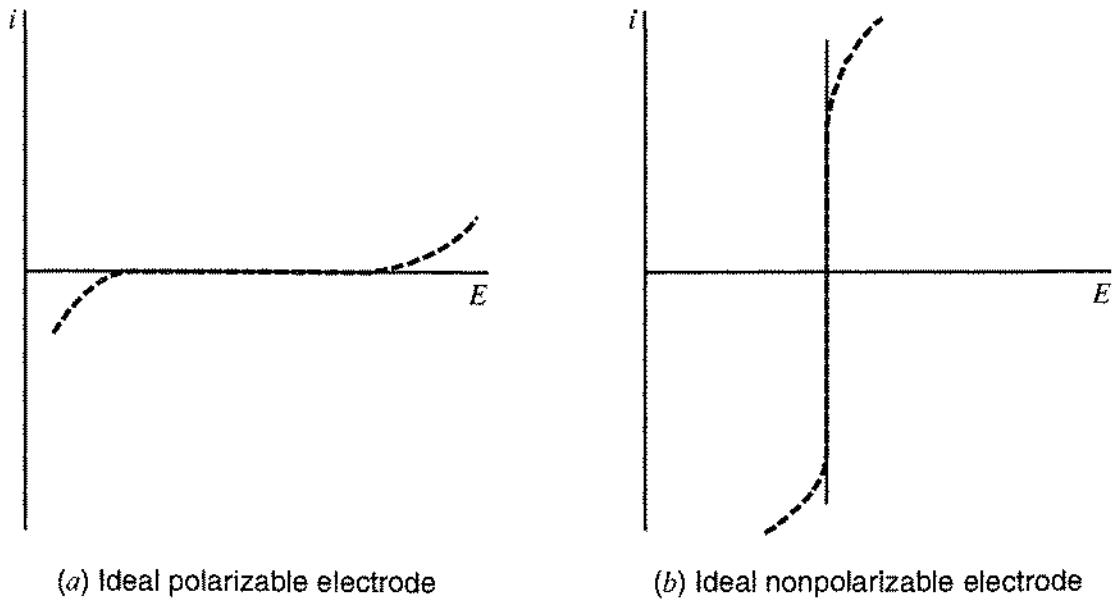

Figure 4. Current-potential curves for ideal (a) polarizable and (b) nonpolarizable electrodes. Dashed lines show behavior of actual electrodes that approach the ideal behavior over limited ranges of current or potential. Reproduced with permission, license number 360538108268 (Bard & Faulkner, 2000).

It can be seen that an ideal nonpolarizable electrode (NPE) has a constant voltage over a small range of current. Thus if the current is small, the reference electrode will always have the same potential, a desirable characteristic. At low currents, a two-electrode system can be used to make electrochemical measurements since the counter electrode can be selected to be a pseudo-reference (silver chloride wire in KCl or NaCl, for example). As long as currents are small, the error in the potential measurement will not be significant. This condition is often met when the working electrode is much smaller than the counter/reference electrode and is typically true in patch

clamping or microelectrode studies. At higher currents, a three-electrode system should be used. Ideally polarizable electrodes (IPE) are also very useful, particularly as working electrodes to study redox reactions. IPE's can accumulate charge, but very little charge crosses the electrode/solution interface. As a result, the majority of current will be a consequence of double-layer charging and redox reactions in solution. The low background currents provide a high signal:noise ratio for studying redox reactions, but produces very small current densities in the absence of a redox electrolyte.

There are generally two types of electrochemical cells of interest: electrolytic and galvanic. In a galvanic cell, reactions occur spontaneously when connected externally to a conductor, with the simplest example being a battery. An electrolytic cell is one in which reactions are influenced by the application of an external voltage, for example electrolysis or electrodeposition. The reactions required for current to flow within either of these cells are simple redox reactions, where the ions either gain or lose electrons with the following relationship, Equation 2.

$$O + ne^- \leftrightarrow R$$

Equation 2.

O is the oxidized species, R is the reduced species, n is the number of electrons involved, and e^- is an electron. The electron transfer is necessary for the flow of Faradaic current. In either case the electrode where oxidation occurs is known as the anode, while where reduction occurs it is known as the cathode. Like most chemical reactions, there are reaction kinetics associated

with the electron transfer, which govern the rate of the reaction. Generally these rates are dependent on the potential and concentrations at the electrode and the number of intermediary steps. One semi-empirical relation that describes electrode kinetics is the Butler-Volmer type Equation 3.

$$i = FAk^0 \left[C_O(0,t) e^{-\frac{\alpha F}{RT}(E-E^{0\prime})} - C_R(0,t) e^{(1-\alpha)\frac{F}{RT}(E-E^{0\prime})} \right]$$

Equation 3.

i is the Faradaic current, F is Faraday's constant, A is the electrode area, k^0 is the standard rate constant of the redox couple, $C_0(0,t)$ is the concentration of species O at the reaction plane (x=0) at time, t, $C_R(0,t)$ is the concentration of species R at the reaction plane (x=0) at time, t, R is the gas constant, T is the absolute temperature, and α is the transfer coefficient - a measure of the symmetry of the energy barrier. Equation 3 can also be put in terms of an exchange current, i_0, which is the magnitude of the current at equilibrium (when the anodic and cathodic currents are equal) as shown in Equation 4.

$$i = i_0 \left[\frac{C_O(0,t)}{C_O^*} e^{-\frac{\alpha F}{RT}\eta} - \frac{C_R(0,t)}{C_R^*} e^{(1-\alpha)\frac{F}{RT}\eta} \right]$$

Equation 4.

η is the overpotential, which is equal to $E-E_{eq}$, the deviation of the potential from equilibrium. All other variables defined previously. Equilibrium potential, E_{eq}, is defined as the potential at which zero current flows, which is easily obtained experimentally. The advantage to working with the exchange current is that the overpotential can be used rather than the formal potential, which may not always be known. The exchange current is a

measure of reaction kinetics. If reaction kinetics are very fast (i_0>>i), Equation 4 reduces to a Nernst-type relationship, Equation 5.

$$E = E^{0\prime} + \frac{RT}{F} ln\left(\frac{C_O(0,t)}{C_R(0,t)}\right)$$

Equation 5.

The consequence of fast reaction kinetics is that the electron transfer is so facile that it doesn't appear as any measurable energy barrier, but rather the electrode potential rapidly achieves equilibrium with the local concentrations, hence the Nernstian form. It should be noted that Equation 4 and Equation 5 are derived under the assumption of a one-step, one-electron reaction.

When a charged electrode is immersed in an electrolyte solution the ions will rearrange themselves to achieve equilibrium. Some ions will adsorb to the surface of the electrode to form the Stern or 'compact' layer. Counterions in solution will be attracted to the electrode surface, coions will be repelled, and a diffuse layer will form very close to the electrode where there is a nonzero net charge. These two layers, the Stern layer (also known as the 'Compact' or 'Helmholtz' layers) and diffuse layer, are known as the electrical double layer, or EDL. A schematic diagram of the EDL capacitance and potential profile can be seen in Figure 5. The Stern layer is sometimes broken into two distinct parts, the Inner and Outer Helmholtz planes, which correspond to a thin layer of adsorbed solvent molecules and other specifically adsorbed species, and the closest approach radius of a solvated ion (x_2 in Figure 5), respectively.

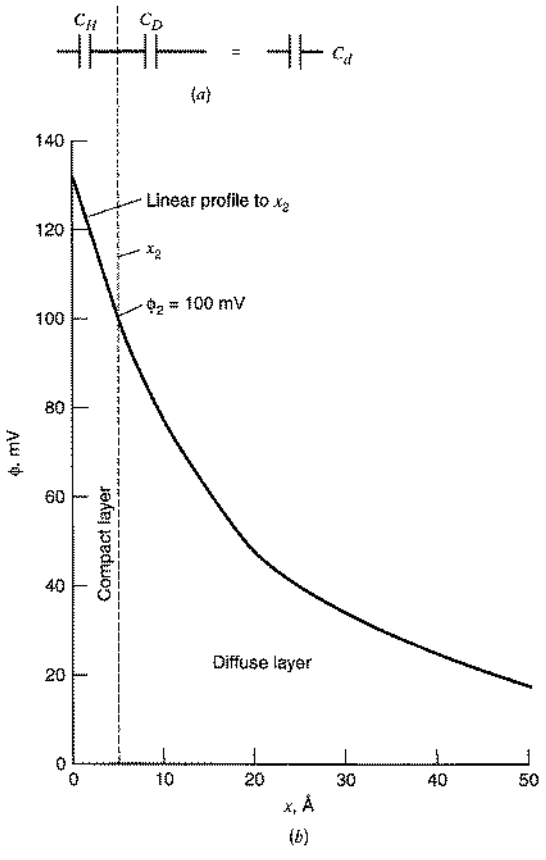

G

Figure 5. (a) A view of the differential capacitance in the Gouy-Chapman-Stern (GCS) model as a series network of Helmholtz- layer and diffuse-layer capacitances. (b) Potential profile through the solution side of the double layer according to GCS theory. Calculated for 10^{-2} M 1:1 electrolyte in water at 25°C. Reproduced with permission, license number 3605381008268 (Bard & Faulkner, 2000).

The characteristic length scale of the diffuse layer is given, for a symmetric electrolyte, by the Debye length, Equation 6.

$$\lambda_D = \sqrt{\frac{\varepsilon RT}{2F^2 z^2 c_0}}$$

Equation 6.

λ_D is the debye length, ε is the dielectric permittivity of the solution, R is the gas constant, T the absolute temperature (K), F is Faraday's constant, z is the ionic valence, and c_0 is the bulk concentration (M). It is seen that the size of the EDL is inversely related to the square root of the bulk electrolyte concentration. Temperature and dielectric variations tend to be less significant in most systems, but adjusting the salt concentration is a common method of fine-tuning the length of electrostatic interactions. The Stern layer is generally on the order of a hydrated radius of an ion (several Angstroms), and acts as a thin dielectric layer. Its thickness is usually negligible, but its contribution to the EDL's electrical response can be significant at higher concentrations. It also affects the effective potential that the solution sees, since there is a potential drop across this layer. This effect is taken into account by the "Frumkin" correction, which is important in some systems. The Stern layer and diffuse layer act as capacitances in series, due to the charging and discharging of the interface. This is shown schematically in Figure 6.

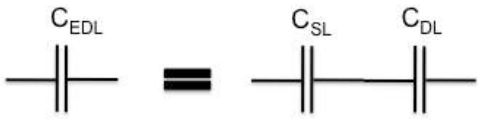

Figure 6. EDL capacitance (C_{EDL}) schematic. C_S is the Stern layer capacitance and C_{DL} is the diffuse layer capacitance.

The net capacitance of series capacitors is given by an inverse relationship, as shown in Equation 7.

$$\frac{1}{C_{EDL}} = \frac{1}{C_{SL}} + \frac{1}{C_{DL}}$$

Equation 7.

The net response is dominated by the smaller of the two values. Experimentally it is found that the Stern layer capacitance is not strongly dependent on concentration, while the diffuse capacitance increases with concentration. The diffuse layer capacitance can be calculated from Gouy-Chapman theory, as given by Equation 8.

$$C_{DL}^{"} = \sqrt{\frac{2z^2F^2\varepsilon c_0}{RT}}\cosh\left(\frac{zF\zeta}{2RT}\right)$$

Equation 8.

In the above, ζ is the potential drop across the diffuse layer, often referred to as the "zeta potential", C_{DL}" is the specific diffuse layer capacitance (capacitance per unit area), and all other parameters have been defined previously. This relationship assumes a binary, symmetric electrolyte. If the concentration is high enough, the diffuse layer capacitance will be large and the Stern layer will thus dominate. Both of these capacitances are proportional to the electrode area in contact with the solution. In fact, measuring the electrode capacitance as a function of concentration provides what is known as a Parsons-Zobel plot from which the electrode surface area and Stern layer capacitance can be calculated (Lützenkirchen, 2006). The Stern layer capacitance can typically be approximated by Equation 9 (H. N. Wang & Pilon, 2011).

$$C_{SL}^{"} = \frac{\varepsilon_S}{\lambda_S}$$

Equation 9.

C_{SL}" is the specific Stern layer capacitance, ε_s is the dielectric permittivity of the Stern layer, and λ_s is the length scale for the Stern layer, x_2 in Figure 5.

For most electrolytes, the Debye length is on the order of a few nanometers, and so except in very small systems the bulk of the solution is screened from the electric field and is considered 'electroneutral'. This fact is used to simplify many macroscale systems, but cannot be used for many micro/nano systems such as colloid suspensions or microfluidic channels, or in cases where the double layer effects are significant (microelectrodes).

There are two types of electrical currents that can flow in an electrochemical system, Faradaic and non-Faradaic. Faradaic currents are a consequence of heterogeneous oxidation or reduction reactions at the electrodes as discussed previously (Equation 2). These reactions depend on a number of factors such as electrode material, solution composition, electrode potential, geometry, and the history of the system. Kinetics of these reactions can range from slow to fast, and reversible to irreversible, with the most basic mathematical descriptions given by Equation 3 through Equation 5. Non-Faradaic reactions are associated with currents that flow as a consequence of charge rearrangement, such as charging or discharging of the double layer. These can sometimes be referred to as a 'displacement' or capacitive current. Both types of current are important to understand for analysis of

electrochemical systems. The equation system that governs concentrations, potential distributions and currents in electrochemical cells is known as the 'Poisson-Nernst-Planck' (PNP) or 'Standard' model, shown below in Equation 10.

$$a)\nabla^2\varphi = -\frac{\rho}{\varepsilon} = -\frac{F\sum z_i c_i}{\varepsilon}$$

$$b)\vec{J_\iota} = -\frac{Fz_i c_i D_i}{RT}\nabla\varphi - D_i\nabla c_i + c_i\vec{u}$$

$$c)\frac{\partial c_i}{\partial t} = -\nabla\cdot\vec{J_\iota} + R_{vi}$$

Equation 10.

Equation 10a) is the Poisson equation: φ is the potential field, ρ is the charge density, ε is the dielectric permittivity of the solution, F is Faraday's constant, z_i is the ionic valence of species i, and c_i is the concentration of species i. Equation 10b) is the Nernst-Planck equation: J_i is the molar flux of species i, D_i is the binary diffusivity of species i, R is the gas constant, T is the absolute temperature, and u is the velocity field. Equation 10c) is species conservation: t is time, R_{vi} is the volumetric generation of species i. This model consists of three parts. Poisson's equation describes the relationship between charge density, ρ, and the potential field, φ. The Nernst-Planck (NP) equation, describes the molar flux of ion subscript i, as the superposition of diffusive, migrational, and convective fluxes. In order to close the system, species conservation is enforced. The molar flux of ions is related to the electrical current density, i, by a simple relationship, Equation 11.

$$\vec{\imath} = F \sum z_i \vec{J_\imath}$$

Equation 11.

The PNP model is a set of coupled nonlinear equations, which in general makes it difficult or impossible to solve analytically, except with certain simplifying assumptions. Numerical methods are often used for more complex systems. The PNP model is further complicated by its boundary conditions. Because Faradaic reactions are associated with heterogeneous reactions, the boundary conditions tend to also be nonlinear (Equation 3 through Equation 5). If the system is such that there are no Faradaic reactions, the boundary condition can be simplified by the enforcement of zero-flux across the electrode. There can still be flux in the solution due to the ions rearranging, but at the electrode no charge directly crosses the interface, as shown in Equation 12.

$$\vec{\imath}(0,t) \cdot \vec{n} = 0$$

Equation 12.

i is the current density at the electrode (x=0) and time t, n is the unit normal to the electrode surface. There are other approximations that can be made in certain circumstances, for example if mass transfer is negligible, or large overpotentials are used, but they will not be addressed here.

The CNP system is comprised of a nanoscopic, amorphous carbon electrode. Carbon is relatively inert, and will not tend to participate in many Faradaic reactions. This means that in the absence of a Redox electrolyte it

will tend to pass non-Faradaic (charging) currents primarily with the zero-flux boundary condition given by Equation 12, while in the presence of a redox species, we will have Butler-Volmer kinetics like those given in Equation 3 or Equation 4. The electrode interface can also be modeled using equivalent circuit components, in what is known as a Randle's Circuit, Figure 7. These circuit parameters can be modeled using the equations described to predict the response of an electrode, or vice versa, the electrode response can be fit to this circuit to infer information about system.

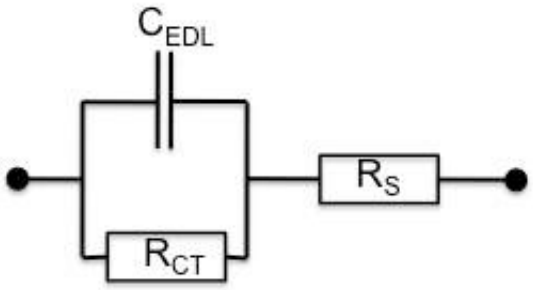

Figure 7. Randle's circuit. C_{EDL} is the double layer capacitance, R_{CT} is the charge transfer resistance and R_S is the series or solution resistance.

The electrochemical community has been using microelectrodes for decades. The general definition of a microelectrode is that the electrode is smaller than the diffusion layer that develops during experiments, and roughly corresponds to electrodes with characteristic sizes less than 25 μm. There are many advantages to such small electrodes. When the electrode area to solution volume (A/V) ratio is very small, the electrode will not greatly perturb bulk concentrations of electroactive species. Also, many applications

take advantage of the small time constants of microelectrodes for dynamic measurements, or of the low ohmic drop which is a consistent source of error with larger electrodes. The time constant of an electrode is approximately given by Equation 13.

$$\tau = R_u C_{EDL}$$

Equation 13.

τ is the time constant, R_u is the uncompensated solution resistance, and C_{EDL} is the double-layer capacitance. The solution resistance scales roughly with 1/L, with L the characteristic length scale of the electrode, while the capacitance scales with the electrode area which goes as L^2. The result is the time constant scales with L, and smaller electrodes allow for the exploration of much faster phenomena. This scaling is described in detail in section 5.9.1 of the following reference: (Bard & Faulkner, 2000). The time constant of a Faradaic reaction is independent of electrode size, and so smaller electrodes can be used to characterize faster electrochemical reactions. Larger electrodes (millimeter-scale) are typically limited to millisecond-scale perturbations, while microelectrodes can access microsecond or even nanosecond time scales in certain circumstances. This gives one the freedom to take advantage of both short-time domains or to rapidly reach steady state or quasi-steady state regimes. An additional advantage to microelectrodes is that they sample a highly localized environment, which has led to recent developments in techniques like scanning electrochemical microscopy (SECM), which uses local electrochemical measurements to map properties or

topography of a system. The downside to microelectrodes is that the small area results in a large junction impedance and can require specialized equipment to measure the small signals that are passed. In addition, the high-sensitivity of these electrodes can make interpretation of data and elimination of noise or artifacts difficult. There are additional difficulties in manipulation, durability, characterization and maintenance.

Patch electrodes have a large, stable electrode interface within the micropipette, and the electrode kinetics are very fast. The result is that the electrode behaves like a resistor, with some stray capacitance that is typically compensated using circuitry or data processing. CNPs have similar morphology, but are actual microelectrodes, with the micro/nanoscale carbon electrode interface directly in contact with the system being measured. This configuration has many advantages. The CNP does not need to be filled with electrolyte, which means it can be filled with other solutions or suspensions for cellular injection, concurrently with electrical stimulus or recording. Also the carbon tip can be completely sealed if microinjection isn't necessary which will prevent diffusion from the tip and other capillary effects. Because the carbon layer is deposited on the interior of the glass micropipette, after etching it will be significantly smaller than the analogous glass tip. Smaller tips will penetrate cells more easily and result in smaller perturbations to the cell in terms of membrane fidelity and Ca^{2+} response (Singhal et al., 2010). The fast time constant, localized measurement, smaller dimensions,

combination of injection/electrode capabilities, batch fabrication, and potential surface functionalizations make CNPs a versatile tool for single-cell studies, representing some of the smallest and cheapest manipulable electrodes.

The use of nanoelectrodes for single cell studies has attracted a considerable interest in recent years. SECM probes have been used to map cells' surface topography with submicron resolution (Amemiya et al., 2008; Bard & Faulkner, 2000; Bergner et al., 2013; Hu et al., 2013; Sun et al., 2008; Sun et al., 2007). Electrochemical impedance spectroscopy has been utilized to detect the binding of target analytes to selectively functionalized surfaces (Actis et al., 2010; Katz & Willner, 2003; Randviir & Banks, 2013). Capacitive measurements are especially useful for biodetection in the absence of redox species that can contribute to the electric current. Carbon microelectrodes have been used in neuroscience for amperometric detection of neurotransmitter exocytosis and for fast scan cyclic voltammetry (FSCV) to monitor specific neurotransmitter concentrations with high temporal and spatial resolutions (Cahill et al., 1996; W. H. Huang et al., 2001; Lin et al., 2012; Mellander et al., 2010; Venton & Wightman, 2003; W. Wang et al., 2009; Wightman et al., 1988). CNPs hold much promise for the above listed applications due to their small size, tunable dimensions, easy fabrication, and amenability to interfacing with standard electrophysiology and cell injection

equipment (Kim et al., 2005; Schrlau, Brailoiu, et al., 2008; Schrlau et al., 2009; Schrlau, Falls, et al., 2008; Singhal et al., 2010).

1.3: Microinjection for Single-cell Studies

In drug discovery, vaccine development, cellular therapeutics development, basic biology, and combinatorial biochemistry, there is a need to controllably inject reagents into a large number of cells to assure statistically significant data about cellular responses. Methods like electroporation (Gehl, 2003; Potter & Heller, 2010) and photoporation (Paterson et al., 2005; Stevenson, Gunn-Moore, Campbell, & Dholakia, 2010) are often used for bulk introduction of reagents into cells; however, these methods are difficult to optimize, lack single-cell resolution, and cannot assure that *all* the cells in the population are treated uniformly and that the intended composition of the reagents is preserved as they diffuse / migrate into the cells. This is significant since in many cases, one needs to control the composition of the mixture that is injected into a cell. For instance, the use of fluorescent tRNA to monitor translation (FtTM) requires high throughput, controlled injection. This recently developed technique (Barhoom et al., 2011) enables the identification and monitoring of active ribosome sites within live cells with submicron resolution, facilitating (i) quantitative comparison of protein synthesis among various cell types, (ii) monitoring the effects of antibiotics and stress agents on protein synthesis, and (iii) characterization of changes in spatial compartmentalization of protein synthesis upon viral

infection. Despite the immense potential of FtTM for measuring translation dynamics and synthesis patterns in real time in normal and diseased cells under various physiological, pathological, and environmental conditions, its widespread adoption has been curtailed by the difficulty in introducing predetermined quantities of fl-tRNA or mRNA into large numbers of cells in an efficient and reproducible manner.

Microinjection remains the most robust method for controllably introducing precise compositions of reagents into cells. The most prohibitive obstacles to microinjection are the relatively low throughput (several hundred cells/hour for most experienced operators), the tedious manual manipulation, and the potential damage to cells. Microinjection success rates are thus highly dependent on operator skill, and it is difficult to attain statistically significant populations of injected cells (Ansorge & Pepperkok, 1988; W. H. Wang et al., 2008). The lack of reliable, high throughput, controllable injection techniques is the bottleneck in many significant projects.

There have been many attempts to automate the cell injection process (Adamo & Jensen, 2008; Ansorge & Pepperkok, 1988; Kallio, Ritala, Lukkari, & Kuikka, 2007; Lukkari & Kallio, 2005; Matsuoka et al., 2005; Mattos, Grant, Thresher, & Kluckman, 2009; Pillarisetti, Pekarev, Brooks, & Desai, 2007; Sharei et al., 2013; Tan, Huang, & Tang, 2009; W. H. Wang, Liu, Gelinas, Ciruna, & Sun, 2007; W. H. Wang et al., 2008; Xie, Sun, Liu, Tse, & Cheng, 2010; Zappe, Fish, Scott, & Solgaard, 2006) using high through

positioning of cells at predetermined locations in an array (W. H. Wang et al., 2007), computer vision (Mattos et al., 2009; Tan et al., 2009; Zappe et al., 2006), novel microfluidic chips (Adamo & Jensen, 2008; Sharei et al., 2013), and feedback systems (Kallio et al., 2007; Lukkari & Kallio, 2005; Pillarisetti et al., 2007; Xie et al., 2010). While these systems have made significant advancements in microinjection rates and efficiency, they are still limited by lack of a robust feedback signal to indicate that the injector has, indeed, penetrated the cell membrane. Penetration-force measurement has been successfully used to detect large cell penetration (Pillarisetti et al., 2007; Xie et al., 2010), but is unlikely to provide the necessary sensitivity for the smaller mammalian cells. Instead, researchers have attempted to use electrical signals.

Electrical measurements have been used with patch electrodes (micropipettes filled with a high concentration salt solution in contact with a non-polarizable electrode, often $Ag/AgCl/Cl^-$ (Bard & Faulkner, 2000; Brown & Flaming, 1986; Geddes, 1972)) to detect cellular contact and penetration in both manual (Brown & Flaming, 1986) and automated (Kodandaramaiah, Franzesi, Chow, Boyden, & Forest, 2012) patch-clamping, and for automated single-cell electroporation (Esmaeilsabzali, Sakaki, Dechev, Burke, & Park, 2012; Sakaki, Esmaeilsabzali, Dechev, Burke, & Park, 2012). Lukkari and co-workers (Kallio et al., 2007; Lukkari & Kallio, 2005) extended this technique to microinjection by placing an electrode in the injection solution. The

solution in the micropipette was continuously subjected to a 10 Hz square wave, and the electric current was monitored. An impedance change was detected upon cell contact and penetration as well as upon pipette breaking/clogging. A similar technique used a DC ionic current measurement to detect cell penetration during electrokinetic injection of cells (Nagai, Torimoto, Miyamoto, Kawashima, & Shibata, 2013). The use of the liquid inside the micropipette as the electrical conductor imposes, however, limitations on the type (typically, high salt concentration) and volume of liquids that can be used in the injection process, adversely affects cells' viability, and limits the time resolution. Hence, it is desirable to decouple the electrical measurement indicating cell penetration from the injection liquid.

Mirkin et al. (Sun et al., 2008) detected cell penetration with solid platinum microelectrodes by introducing a redox mediator in the extracellular solution, similar to techniques used in scanning electrochemical microscopy (SECM) (Bard & Faulkner, 2000; Sun et al., 2007). The use of a redox mediator may, however, adversely impact cell viability and function (Liu, Sun, Zhai, & Dong, 2009), and the solid microelectrodes are not suitable for introducing fluids into cells. CNPs provide a unique solution for microinjection feedback, using the carbon lining as to detect penetration electrochemically, independent of the injection fluid, among other capabilities.

Chapter 2: CNPs for Cellular Probing and Microinjection

2.1: Background

As discussed in the introduction, microinjection and single-cell probing suffer from a major drawback in that they require experienced operators to manually position micropipettes and electrodes relative to delicate cells. There is a strong need for robust feedback to ensure that cells are injected and probed in the most minimally invasive manner to preserve cell viability and decrease any unwanted perturbations.

Here, we use an AC, electrical impedance measurement to detect cell and nucleus penetration with carbon nanopipettes. Using an AC signal allows us to transmit relatively large non-Faradaic (charging) currents that can be easily measured and processed with Fourier methods to yield accurate data. Much of our data is presented in terms of the equivalent capacitance, which is highly sensitive to the electrode's local environment and not dependent on Faradaic reactions (Katz & Willner, 2003). Oxygen, a natural redox species, is present in our system, but does not contribute significantly to the Faradaic current at the potentials used in our experiments (Zachek, Takmakov, Moody, Wightman, & McCarty, 2009) and does not provide significant contrast between intra/extracellular environments due to its free diffusion across the cellular membrane.

Our system has a number of advantages over previously proposed methods that utilized the injection liquid in the pipette's bore as the conductive path to detect cell penetration (Kallio et al., 2007). In the CNPs, the electrical signal is not dependent on the injection liquid, the injection liquid need not be conductive, and one can operate with small volumes of injection liquid (as there is no need to bring the injection liquid into contact with an electrode). Additionally, the small size of the CNP and the AC method provide much greater temporal resolution than is possible with ionic electrodes. We will explore the behavior and application of this technique for both microinjection (fluid within the CNP), and cellular probing (CNP is empty of fluid and pressurized to prevent capillary rise).

2.2: Experimental

2.2.1 Cell Culture and Imaging

The experiments were carried out with adherent human osteosarcoma cells (U2OS, ~40 μm diameter). U2OS cells were selected for their availability and ease of culture. The cells were cultured in Dulbecco's Modified Eagle's Medium (HyClone) with 10% Fetal Bovine Serum (HyClone) and 1% Penicillin/Streptomycin antibiotics (HyClone) in a standard (Fisher Isotemp) CO_2 incubator (37 C, 5% CO_2). The cells were then plated on Poly-L-Lysine treated glass coverslips (1 mg/mL solution) or directly grown in 35mm tissue culture dishes (Corning). The plated coverslips were transferred to petri dishes with cell culture medium for experiments.

The experiments were carried out at room temperature in standard atmosphere without any CO_2 regulation. During the experiments, the cells were outside the incubator for at most two hours. The measured data did not change significantly over this time interval, and cells remained viable, as evidenced by continued proliferation several days after the experiments.

An Olympus IX-71 inverted optical microscope with long-working-distance, phase-contrast objectives, Hamamatsu CCD camera, and HCImage Software were used to image the cells and track the carbon nanopipettes during probing. The entire system was encased in a copper-mesh Faraday cage to reduce electromagnetic interference and was located on an air-damped, vibration-isolation table (TMC MICRO-g).

2.2.2 CNP Fabrication

CNPs were fabricated with 1mm outer diameter, 0.7 mm inner diameter, filamented quartz capillaries of 7.5 cm length (Sutter Instruments). Pipettes were pulled using a Sutter P-2000 laser-based pipette puller with the parameters: HEAT 800, FIL 4, VEL 60, DEL 128, and PULL 100. Chemical vapor deposition was performed on the pipettes in a Lindberg horizontal tube furnace, with a 1" inner diameter quartz furnace tube at 875 C. The flow conditions were 200 sccm of methane and 300 sccm of argon (AirGas ultra-high purity) for a total deposition time of 40 minutes. Some pipettes were also fabricated in a Carbolite HVS 3-zone horizontal tube furnace with a 1.3" inner diameter quartz tube at 905 C, with flow conditions

of 400 sccm methane and 600 sccm argon, for a 3 hour duration which yielded equivalent carbon deposition. During deposition, the pipette tips were oriented against the flow of the gas, i.e., the tip pointed upstream. The carbon deposited selectively only inside the pipette, not on the pipette's outer surface.

The carbon-coated pipettes were etched in 5:1 buffered hydrofluoric acid (Transene Buffer HF Improved) followed by a 10-minute rinse in deionized water. The pipettes were inspected under an optical microscope and imaged with a SEM (FEI Quanta 600 ESEM). The tip outer diameter ranged from 200 to 400 nm, the inner diameter ranged from 50 to 200 nm, and the exposed carbon tip length depended on the etch time, but typically was between 4 and 20 μm for etch times between 15-60s. The tip had a conical shape with a cone angle of 1.6 degrees on average. The electrical resistance of the CNPs was on the order of tens of kΩ. When in solution, the DC junction impedance was on the order of 5GΩ, as measured by impedance spectroscopy. At 1 kHz in a typical cell medium, the interfacial impedance drops to 10-100 MΩ. The patch clamp amplifier headstage has a 0.5GΩ input impedance for the gain setting used.

2.2.3 Impedance Measurements

The CNP was connected to a HEKA EPC 10 patch clamp amplifier (HEKA Instruments Inc.) with a standard 1mm HEKA micropipette holder. A lead wire was connected at one end to the pin of the BNC connection

(standard coaxial coupling). The other end of the wire was inserted into the distal end of the CNP. Slight bends in the wire endowed the wire with sufficient springiness to press it against the carbon film and form an electrical contact with the CNP's inner carbon lining. Despite its simplicity, this electrical connection proved reliable. The pipette holder provided a hermetic seal around the CNP using a compression fitting with O-rings. Fluidic tubing with a bayonet coupler connected the hollow of the CNP to a pressure injection system (Eppendorf FemtoJet) via a simple tubing connection on the HEKA pipette holder.

The LockIn module of HEKA's PATCHMASTER software was used to monitor the current response, complex impedance, and DC conductance. Typically, the capacitance and the real part of the impedance were monitored in real-time during probing. A voltage with amplitude of 10mV, 1 kHz frequency, and -70mV offset was used with a sampling rate of 20 kHz. The impedance and capacitance data were computed once per cycle, resulting in an effective time resolution of 1ms. We elected to operate at 1 kHz since filtering proved effective, long sweep durations (~120s) could be used, and the measurement noise was near its minimum as previously demonstrated by Chen and Gillis (P. Chen & Gillis, 2000). Examining the frequency response of the electrode impedance in a simple electrolyte solution produced a traditional Nyquist plot for a Randle's circuit, and at 1 kHz the electrode was outside the Warburg regime (Bard & Faulkner, 2000).

The voltage offset was selected to be approximately equal to a typical membrane potential to avoid significant polarization of the cell during probing (Gillis, 2000). The capacitance measurement was not sensitive to the offset voltage as long as the charge transfer resistance was much greater than the solution resistance, which holds true in a typical non-Faradaic system such as ours (Gillis, 2000). No capacitance or bridge compensation was used during the measurements. Bessel low-pass filters of 2.9 kHz and 10 kHz were used in series for the current measurement, and the resulting data (capacitance, conductance, and impedance) was further filtered in real-time using the digital filter on the PATCHMASTER oscilloscope of ~5Hz. The 1mV/pA gain setting was used. A silver/silver-chloride wire was inserted in the extracellular solution and used as a pseudo-reference and counter electrode.

2.2.4 Micromanipulation and Cell Experiments

For cell probing (no microinjection), the headstage of the amplifier was mounted on a piezoelectric micromanipulator (Eppendorf Transferman NK2). The CNP tip was brought into focus when ~50 μm above the cell. The pipette was then slowly lowered, and the scope was refocused until the CNP was visible several microns above the cell of interest. The background pressure in the pipette was adjusted to 300-400 kPa to minimize capillary imbibition. The signal stabilized within a few minutes of the application of the background pressure. This time constant is associated with the time required

to eject any fluid that was uptaken by capillary rise in the hollow of the CNP. At pressures above 300 kPa, the capacitance and impedance were pressure-independent, indicating complete expulsion of liquid from the inside of the pipette.

The CNP was manually lowered into the cell using the joystick on the piezomanipulator at <5μm/s and then halted upon cell or nucleus penetration. The impedance and capacitance were measured as functions of time. Cell penetration was confirmed visually. Upon contact with the cell, a cleft in the cell membrane created a contrast difference at the tip of the CNP (enhanced by the phase-contrast filters). Microinjection experiments of fluorescent dye verified that this visual clue does, indeed, indicate cell penetration. The measured impedance change occurred simultaneously with the imaged penetration into the cell cytoplasm or the cell nucleus. Nuclei were clearly visible under the microscope. The instances of CNP penetration into and removal from the cell were recorded for each data series. Data was exported to Matlab software (Mathworks Inc.) for analysis. Because the CNPs penetrated the cell rapidly and were typically held stationary after penetration, the signals often resembled step-changes. The data during the penetration was averaged and extracellular values were subtracted. The extracellular values before and after penetration were averaged to account for any drift.

To measure the impedance as a function of cell penetration depth, the CNP was brought into position above a cell and the micromanipulator was programmed to traverse at a constant speed of 400nm/s downwards with the pipette normal to the cell membrane. The resistance and capacitance were measured as functions of time. The time axis was then translated to the CNP tip's position. The data was exported to Matlab and was offset by the extracellular value to obtain the signal change as a function of depth. The spatial resolution of this technique is limited by the accuracy of the manipulator. The manufacturer's specified step size is 40nm, and the manipulator traversed at 10 steps/s.

To study the effect of capillary rise inside the CNP, the extracellular capacitance value was measured as a function of CNP pressure.

For microinjection studies, the headstage of the amplifier was mounted similarly. The CNPs were back-filled with 5-10μL of solution using Eppendorf Microloader tips and secured to the headstage using the 1.0mm pipette holder. For continuous flow injection, the control pressure was set to 1-4 kPa. For pulsed injection the control pressure was typically set to .5-1.0 kPa. This control pressure and injection pressure were calibrated by injecting a few test cells. Pipettes were manually lowered into cells until there was a change in the impedance. The cell was either injected via the control flow, or with a burst of pressure (5-20 kPa for 0.3s) to force fluid into the cells. Cell injection was confirmed visually by cell swelling. Impedance traces and computed

capacitance traces were acquired and monitored in real time. The impedance change was measured immediately after cell and nucleus penetration.

2.3: Results and Discussion

2.3.1 A Simplified Circuit Model

The basic premise of our detection scheme is that, as the CNP tip crosses the cell membrane, there is a change in the impedance due to the electrode surface contacting the intracellular solution, which differs in its characteristics from the extracellular solution, and due to the added impedance of the cell membrane. Figure 8 depicts schematically an analog electrical circuit of the CNP-cell system (Bard & Faulkner, 2000; Gillis, 2000; Katz & Willner, 2003). The symbols R and C denote, respectively, resistance and capacitance. The significance of the various subscripts and superscripts is delineated in the figure's caption. Briefly, the electrode-liquid interface is modeled as a Stern capacitor (C^S) in series with a Debye (diffuse) layer capacitor (C^d). These capacitors are connected in parallel with a Faradaic charge transfer resistor (R^t). Since, in the absence of redox species, R^t is large, we can treat the electrode as blocking (perfectly polarizable). Likewise, the membranes can be approximated as capacitors. To the first order of approximation, we can approximate the circuit model with capacitors alone, as shown in Figure 8 B and C**.**

When the CNP resides in the extracellular solution (Figure 8B), its equivalent capacitance is:

$$C_{eq,o} = C_o^{''}\left(A_i + A_o\right) + C_j$$

Equation 14,

where C_o'' is the combined capacitance per unit area of the Stern and Debye layers at the interface between the CNP tip's carbon surface and the extracellular solution. C_j is the total capacitance of the surface inside the CNP's bore. For later use, the CNP's outer exposed surface is decomposed into area A_i and area A_o representing, respectively, the part of the CNP tip that will penetrate into the cell and the part that will remain in the extracellular solution post penetration. When the CNP is outside the cell, the entire area, $A_i + A_o$, is exposed to the extracellular solution.

When area A_i of the CNP tip is inside the cell, the equivalent capacitance of the CNP is:

$$C_{eq,i} = C_o^{''}A_o + \frac{\left(C_j + C_i^{''}A_i\right)C_m}{C_j + C_i^{''}A_i + C_m}$$

Equation 15,

where C_i'' is the capacitance per unit area of the carbon surface – intracellular solution interface. $C_m = C_m" A_m$ is the cell membrane capacitance, C_m" is the membrane capacitance per unit area, and A_m is the membrane area.

The change in capacitance upon cell penetration is thus:

$$\Delta C_{eq} = \left\{\frac{C_m}{C_j + C_i^{''}A_i + C_m} - 1\right\}C_j + \left\{\frac{C_i^{''}C_m}{C_j + C_i^{''}A_i + C_m} - C_o^{''}\right\}A_i$$

Equation 16.

The first term in Equation 16 represents the contribution of the CNP's inner bore to the capacitance change. The second term is proportional to the area of the CNP tip that is submerged inside the cell. The presence of an ionic solution in the CNP's bore greatly increases the magnitude of ΔC_{eq} compared to the case of the empty CNP.

When a liquid-filled CNP is just slightly immersed in the cell (A_i is small) and liquid is present in the CNP's bore, Equation 16 reduces to

$$\Delta C_{eq} \sim \frac{-C_j^2}{C_j + C_m}$$

Equation 17.

The capacitance change upon cell penetration is dominated by the capacitance of the internal CNP's bore and is negative.

In the absence of liquid in the *CNP*'s bore, C_j is negligible. The change in capacitance upon cell penetration is given by the second term in Equation 16:

$$\Delta C_{eq} \sim \left\{ \frac{\left(C_i'' - C_o''\right) C_m - C_o'' C_i'' A_i}{C_i'' A_i + C_m} \right\} A_i$$

Equation 18,

and the change in capacitance is proportional to the area of the CNP tip submerged inside the cell. Depending on the relative magnitudes of C_o" and C_i", the expression in Equation 18 can be either positive or negative. When the intracellular and extracellular solutions are nearly isotonic $\left(C_i'' \sim C_o''\right)$,

Equation 18 reduces to $\frac{-C_o^{"}C_i^{"}}{C_i^{"}A_i + C_m}A_i^2 < 0$. The above equation suggests that by monitoring the capacitance of an empty CNP, in addition to detecting cell penetration, we should be able to estimate the penetration depth. As we shall see shortly, the simplified capacitance-based theory can provide insights into many of our experimental observations presented below.

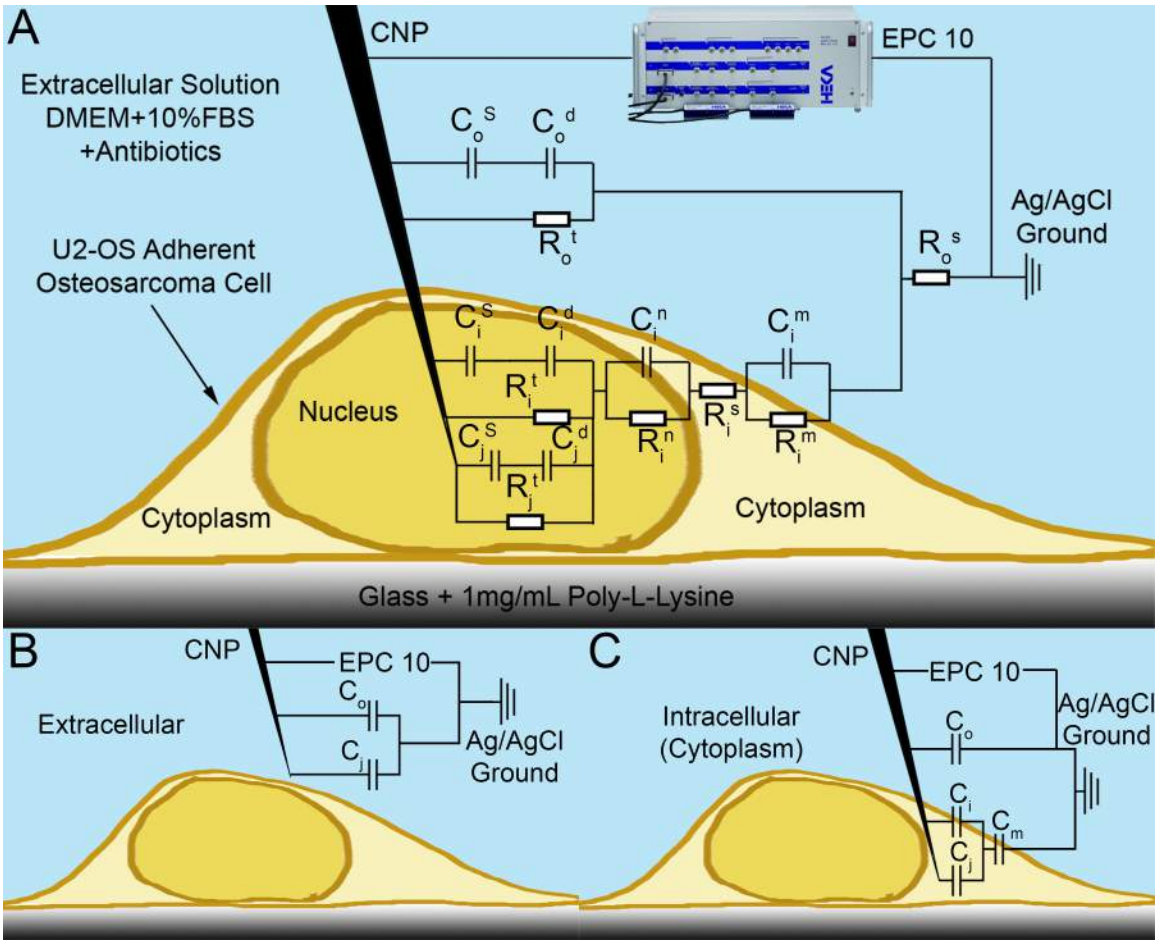

Figure 8. A schematic depiction of a CNP penetrating an adherent cell with the equivalent circuit model overlaid. HEKA EPC 10 patch clamp amplifier shown. C and R denote, respectively, capacitors and resistors. Subscripts o, i, and j designate, respectively, extracellular, intracellular, and inner-pipette circuit

components. Superscripts designate the following: S - Stern layer (capacitance), s-series (resistance), d – diffuse layer, n – nuclear membrane, m – cellular membrane, t – charge transfer. When modeling cytoplasm probing, the nuclear circuit elements (Cin and Rin) are omitted. (A) Complete circuit model. (B) Extracellular circuit approximation, only capacitors are included. (C) Intracellular (cytoplasm) circuit approximation, only capacitors are included. For cell probing without an internal fluid interface in the CNP the inner-pipette circuit components are not included.

2.3.2 Cell Penetration Detection

Figure 9 depicts typical experimental results during cell probing with a CNP pressurized to preclude capillary rise. Figure 9A and B are micrographs of cellular probing into the cytoplasm (A) and nucleus (B). Figure 9C depicts schematically the CNP tip's position in the extracellular solution (EC), cell cytoplasm (C), and nucleus (N). Figure 9D depicts the measured equivalent capacitance C_{eq} as a function of time (and, indirectly, probe position) for penetration from the extracellular solution into the cytoplasm and into the cell nucleus. Initially, the probe's tip traversed the extracellular solution and the equivalent capacitance remained nearly fixed. The low-pass filtered signal exhibited RMS (root mean square) fluctuations of about 2.0 fF. When the CNP's tip first touched the cell membrane, a dimple was observed in the membrane. At time t~5s, the CNP's tip penetrated through the cell membrane and C_{eq} dropped sharply by 23 fF. C_{eq} remained at this lower level as long as the CNP tip remained inside the cytoplasm. Once the tip was

withdrawn from the cytoplasm (t~10s), the probe nearly regained its extracellular capacitance. At time t~20s, the probe was inserted into the cell's nucleus and the measured capacitance dropped by 49 fF from its extracellular value. Upon withdrawal to the extracellular medium (t~26s), the probe regained its extracellular capacitance. Witness the large difference between the capacitance changes (a factor of ~2) upon penetration into the cytoplasm and into the nucleus. The measured changes in capacitance are consistent with the predictions of our theoretical model. In the model, we used the characteristic values of cell membrane capacitance typical to U2OS cell. A CNP with 4μm exposed length, 1.6 degree cone angle, and 250 nm tip diameter is predicted to experience 23fF drop in capacitance when penetrating 2.6μm into the cytoplasm and 46fF drop in capacitance when penetrating 1.1μm into the model's cell nucleus. We assume that the entire 1.1μm of the CNP tip is within the cell nucleus and neglect any intermediary electrode interface between the nuclear and cell membranes. The nuclear membrane is conformal with the cell membrane in an adherent cell, and so this approximation is reasonable for modeling nuclear penetration.

Figure 9E (Top panel) depicts eight sequential probing events with the same CNP into the cytoplasm (C) and the nucleus (N) of different cells over a time interval of 120s. The penetration into the nucleus consistently resulted in a greater capacitance change than did the penetration into the cytoplasm,

with average values (± one standard deviation) of ΔCeq = -43.8±17.7fF (nucleus, N=133), compared to -30.6±17.4fF (cytoplasm, N=138).

Upon nucleus penetration and withdrawal, the capacitance signal occasionally featured sharp transient troughs (Figure 9 D and E). Although the causes of these troughs is not known with certainty, the relaxation time of these troughs of 0.3±0.04s (N=6) is consistent with the documented relaxation time associated with mechanical deformations of typical cells (Wong, Tan, & Ho, 2005). We hypothesize that during cell penetration, the CNP deformed the cytoskeleton and membrane. The transient peaks are likely associated with the time that it takes the cytoskeleton to recover its original state prior to cell penetration. These peaks could also be associated with Cottrell-type currents due to a jump in potential across the cell membrane. Membrane potential can vary by tens of mV across cells and cell lines, making this hypothesis also plausible.

Figure 9F (Top panel) depicts the real part of the impedance, Re(Z), as a function of time for the same penetration events shown in Figure 9C. ΔC_{eq} was accompanied by a concurrent increase in the real part of the impedance, ΔRe(Z). The ΔRe(Z) measurements had mean values (± one standard deviation) of 85.0±46.7kΩ (cytoplasm, N=138) and 86.9±87.1kΩ (nucleus, N=133), demonstrating relatively small difference between cytoplasm and nuclear probing and a large spread in the nuclear probing data. The

difference between cytoplasmic and nuclear ΔRe(Z) was not statistically significant (P=0.59).

The lower panels of Figure 9 E and F are normalized time-derivatives of the data presented in the corresponding upper panels. The time derivatives were calculated by taking the difference between adjacent data points, using a 500 point (0.5s) moving average, and normalizing the difference with its maximum value. The spikes in the derivatives provide a convenient way to identify cell and nucleus penetration and retraction of the CNP from the nucleus and the cytoplasm. From the perspective of automation, a spike exceeding a pre-set threshold (i.e., the dashed lines in Figure 9 E and F) may be used to indicate cell or nucleus penetration and halt the manipulator's motion.

To discriminate between the signal changes due to contact with the substrate and cell penetration, we contacted the substrate lightly with the CNP tip in a region free of cells and measured the corresponding effect on the CNP's impedance (data not shown). In all cases, C_{eq} increased and Re(Z) decreased compared to their corresponding values in the extracellular solution. The reasons for these particular trends are not obvious and likely resulted from the CNP tip's bending when pushed against the substrate. The control experiments indicate, however, that the sign of the capacitance and resistance variations readily distinguishes between cell penetration and unintended contact with the substrate.

Slight drift and fluctuations both in the extracellular and intracellular measurements may have resulted from equipment vibrations, induction noise, capillary rise inside the CNP, physiological variations in the cell, and modifications in the electrode's surface due to fouling, and clogging. Indeed, the high sensitivity of the capacitance measurement to changes in the electrode interface's conditions can be used to detect CNP breakage and clogging.

Despite having an electrode surface area much smaller than traditional microelectrodes, on the order of $10\mu m^2$, compared to microelectrodes' 10^2-$10^3\mu m^2$, a signal change was detected in all of the cell probing events, demonstrating that the CNPs can robustly and reliably detect cell penetration through capacitance measurement. The empty CNPs behave like ultra-micro electrodes (UME), albeit with the benefit of much greater spatial resolution and smaller intrusion.

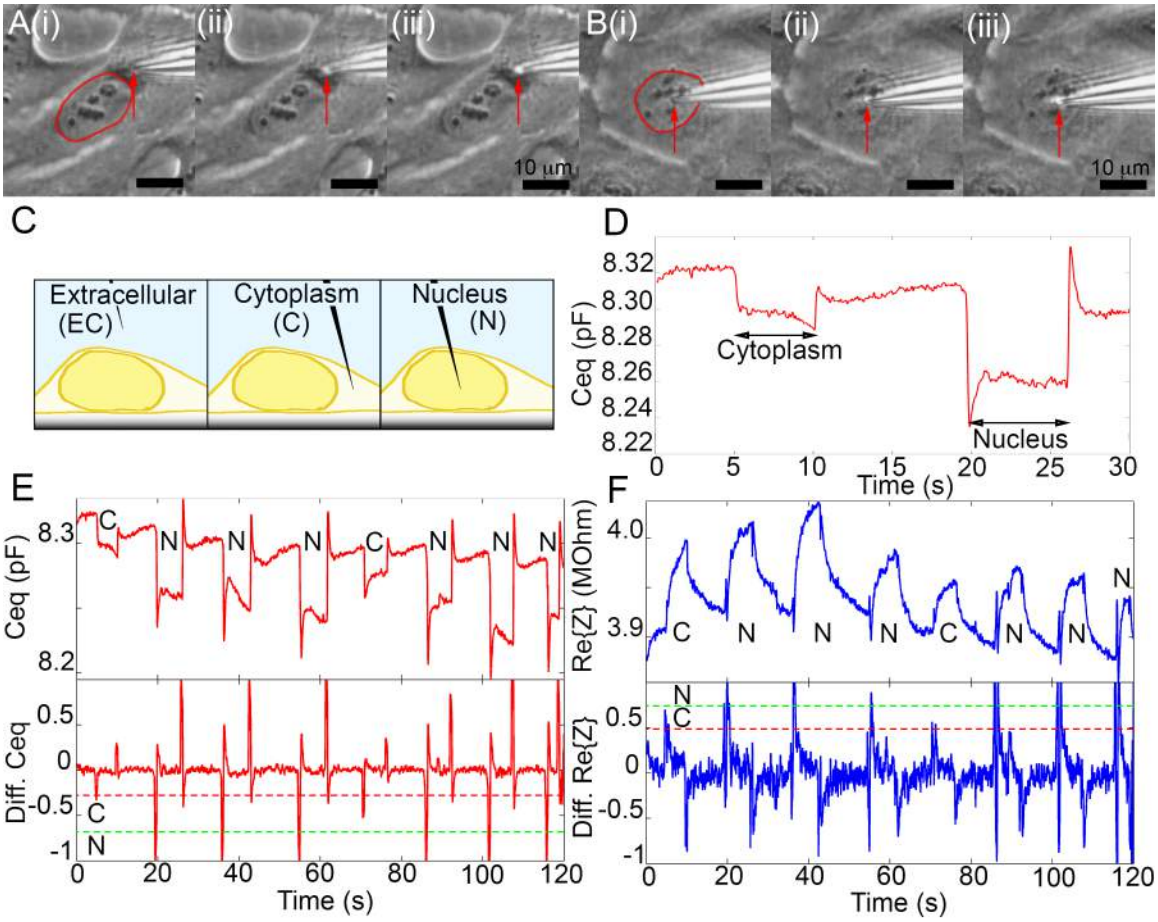

Figure 9. Cell penetration impedance detection with an empty (pressurized to 300 kPa) CNP. (A) Micrographs of probing the cell cytoplasm. (i) The CNP is outside of the cell, (the nucleus outlined with a red line). (ii) The CNP has just contacted the cell membarne. (iii) The CNP lowered into the cell. (B) Probing the cell nucleus. (i) The CNP is outside of the cell, (the nucleus outlined with a red line). (ii) The CNP has just contacted the cell. (iii) The CNP has been lowered into the nucleus. Membrane contact/penetration is indicated by the bright spot at the pipette's tip due to the phase contrast filter, enhancing the contrast at the deformed membrane cleft. The CNP tip is identified with red arrows. Scale bar 10μm. (C) Schematics showing the CNP's tip positions: in the extracellular solution (EC, left), in the cell cytoplasm (C, middle), in the cell nucleus (N, right). (D) The measured capacitance as a function of time before, during, and after penetration into the cell cytoplasm

and the nucleus. (E) The capacitance (Top) and the normalized capacitance time derivative (Bottom) as functions of time for cytoplasmic (C) and nuclear (N) probing events in different cells with the same CNP. (F) Re(Z) (Top) and its normalized time-derivative (Bottom) as functions of time for the same probing events in panel C. The dashed lines in (E) and (F) represent possible threshold values for identifying cytoplasmic and nuclear penetration.

For detection of cellular penetration during microinjection, the bore of the CNP is filled with the solution to be injected. The pipette tip is lowered through the extracellular solution until it penetrates the cell membrane, injection takes place, and then the pipette is removed. In practice, a small backpressure is applied to the pipette as it approaches the cell to induce weak flow through the pipette's tip. This flow serves both to prevent capillary uptake of extracellular/intracellular solution into the bore of the pipette and to minimize clogging.

The injection system operates in either continuous flow mode or pulse mode. In the continuous mode, the backpressure remains unaltered as the pipette penetrates the cell, and the infusion volume is controlled by the duration of the pipette's penetration. In the pulse mode, upon penetration, the backpressure is increased greatly, and the infusion volume is dictated by the magnitude and duration of the pressure pulse. Below, we examine the effects of both modes of operation on the measured impedance. In all the

experiments, we used filamented CNPs with ~300 nm diameter tips and ~16μm exposed tip length.

2.3.3 Continuous Flow Microinjection

While operating in the continuous injection mode, we lowered a liquid-filled CNP, subjected to 1-4 kPa pressure, through the extracellular solution until it penetrated into the cell. After a 1 s dwelling time, we withdrew the CNP from the cell and moved it to the next cell, repeating the process. The pressure and penetration duration were selected so as to produce a visible cell swelling, which was used to verify that infusion had, indeed, occurred. In our automated injection system, we will not rely on visual clues to determine the injected volume. Instead, we plan to use correlations that calibrate the injection volume as a function of pressure and dwelling time. The CNP's impedance was continuously monitored throughout this process.

Figure 10 depicts the changes in the equivalent capacitance ΔC_{eq} (lower curve) and the change in resistance, $\Delta Re(Z)$ (upper curve), upon penetrations into and withdrawals from different cells. The capacitance and resistance changes correlated with visible swelling of the cells due to injection. The background capacitance and resistance signals were very stable, with RMS noise of approximately 0.011pF. Upon cell penetration, there was a sharp drop in capacitance of 1-3 pF, consistent with Equation (4), and an increase in resistance of 200-300 kΩ. Upon removal of the CNP tip from the cell, the capacitance and the resistance returned to their

extracellular, baseline values. The scatter in ΔC_{eq} and $\Delta Re(Z)$ can be attributed to variations in the sizes and states of the cells, as well as the penetration location and depth of the pipette.

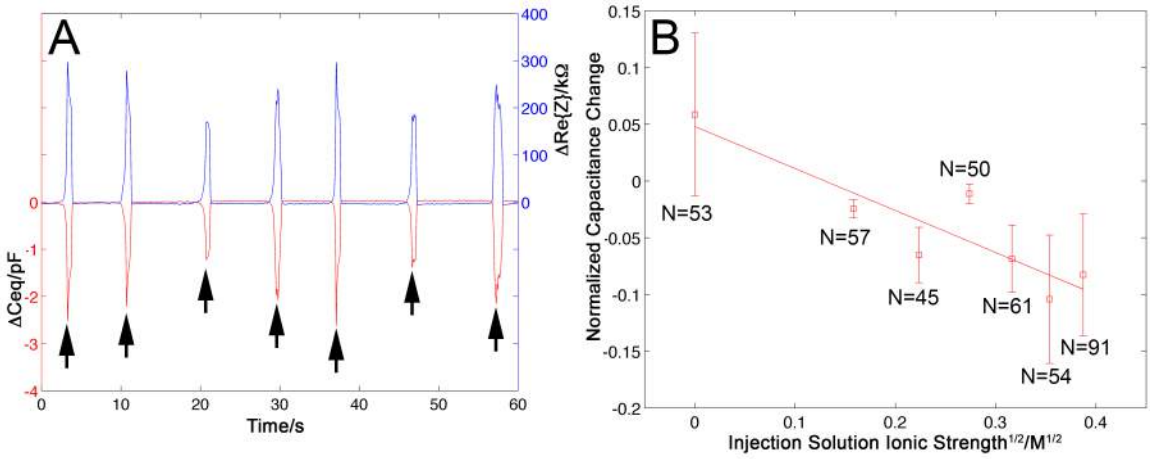

Figure 10. (A) The change in the CNP's capacitance, ΔC_{eq} (red trace, left axis), and the change in the CNP's resistance, $\Delta Re(Z)$ (blue trace, right axis), upon penetration into and withdrawal from various cells when operating in continuous-flow microinjection mode (pressure 1-4 kPa, and 100mM KCl injection solution). (B) The normalized change in capacitance $\Delta C_{eq}/C_0$ upon cell penetration as a function of the square root of the injection solution's (KCl) ionic strength. C_0 is the CNP capacitance when in the extracellular solution. The symbols represent the average of N measurements and the vertical bars represent one standard deviation. The solid line is a linear best-fit. R^2=0.80. Each data point corresponds to a distinct CNP. All the data was acquired from the same cell culture on the same day, with the exception of the data point to the far right, which was obtained with two different CNPs and two different cell petri dishes.

2.3.4 Effect of Solution's Ionic Strength on ΔCeq

Although normally it is preferred to inject the cell with a solution of similar osmotic strength to that of the cytoplasm to prevent stressing the cell, occasionally, it is necessary to use other solution concentrations. Thus, it is of interest to examine the effect of the injection solution's ionic strength on ΔC_{eq}. Equation 17 suggests that the capacitance change ΔC_{eq} is proportional to the capacitance of the CNP's carbon film – injection solution interface (C_j). C_j is composed, in part, of the electric double layer capacitance next to the inner carbon layer (ε/λ_D), where ε and λ_D are, respectively, the solution permittivity and the Debye screening length. Since the Debye screening length is inversely proportional to the square root of the ionic strength, one would expect ΔC_{eq} to decrease linearly with the square root of the injection solution's ionic strength. Figure 10B depicts $\Delta C_{eq}/C_0$ (C_0 being the extracellular baseline capacitance) as a function of the square root of the injection solution's ionic strength. Each data point represents the average of N measurements. The error bars correspond to one standard deviation. The far right data point includes results from the pulsed microinjection experiment, which was also carried out with a 150mM KCl solution. In the aggregate, the figure summarizes results of 411 events. The solid line is a linear best fit with R^2=0.8. Consistent with expectations, the experimental data decreases nearly linearly as the square root of the ionic strength increases.

When the injection solution had very low ionic strength, the capacitance increased upon cell penetration. We hypothesize that the low concentration solution effusing out of the CNP mixed with the solution enveloping the tip, reducing its concentration and the magnitude of the electric double layer capacitance C_o" in the absence of effusion. Upon cell penetration, the extracellular interface re-equilibrated with the surrounding buffer, C_o" increased, while the effusion kept C_i"< C_o". Since under these circumstance C_j is also small, the net effect is that $\Delta C_{eq}>0$, consistent with experiments.

2.3.5 Pulsed Microinjection

In pulsed microinjection, the background pressure of the microinjection pipette is kept relatively low. The majority of the injection is achieved through a controlled burst of pressure after the CNP's insertion into the cell. To test the penetration detection when operating in pulse mode and to examine the effect of the injection pulse on the measured impedance, we injected 150 mM KCl solution into U2OS cells (plated on tissue culture dishes with cell media) while concurrently recording C_{eq} and Re(Z). This particular salt concentration was selected to approximately match the ionic strength of the cytoplasm (Alberts et al., 2013). A control pressure of 10 hPa was applied continuously to the CNP prior to and during cell penetration. Subsequent to cell penetration, we applied a pressure pulse of 125 hPa for 0.3 s to inject the KCl solution into the cell. We verified the injection by visually monitoring cell

swelling. The amount of cell swelling in our experiments was consistent with that observed by others (W. H. Wang et al., 2008) during microinjection. The injected volume was small enough (<10% of the cell volume) as not to impair cell viability. Although we have not done so, the injection volume could be quantified by including fluorescent dye in the injected solution, monitoring the dye emission intensity, and using calibration table to correlate the emission intensity with the injected volume (Ilegems, Pick, & Vogel, 2002; Minaschek, Bereiterhahn, & Bertholdt, 1989; Shan, Lang, & Dimotakis, 2004).

Figure 11 illustrates pulse injections into the cytoplasm and the nucleus. In applications, the pipette would be withdrawn from the cell promptly after the injection. However, in the experiments of Figure 11, we left the CNPs' tip inside the cell for ~80s to monitor signal stability. Figure 11 A and C are, respectively, micrographs of cellular and nuclear penetration and the subsequent injection-induced swelling. The edges of the cell (Figure 11A) and nucleus (Figure 11C) are outlined with dotted lines for better visibility. As the cell swelled, various organelles were seen more clearly than prior to swelling due to the phase contrast filter on the microscope. For example, the nucleus becomes more distinct as the cell membrane is displaced by the fluid injected into the cytoplasm (Figure 11A).

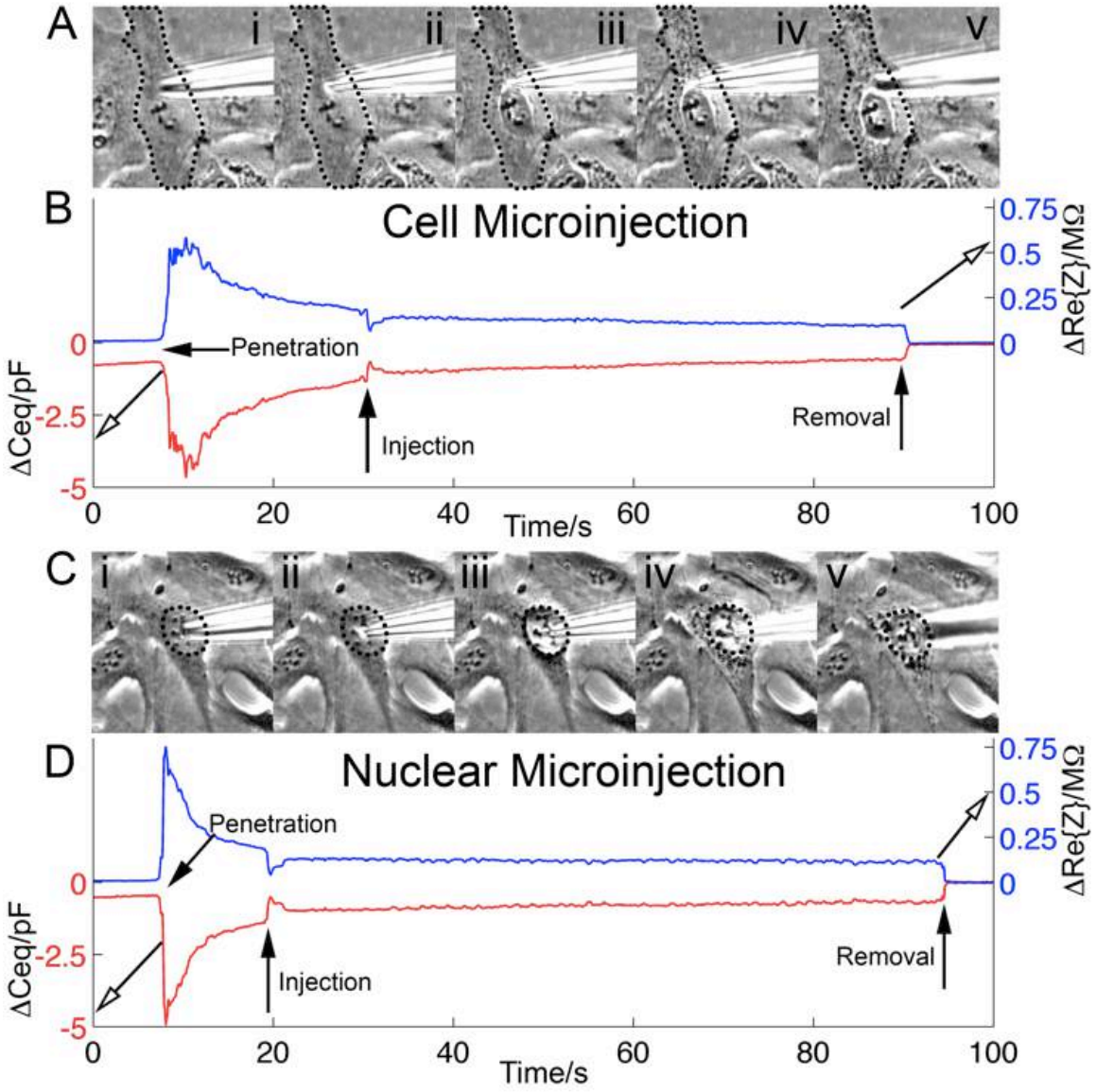

Figure 11. Concurrent penetration and microinjection detection. Control pressure: 10hPa. Injection pulse: 125hPa for 0.3s. (A) Micrographs of the cell: CNP in extracellular solution (i); CNP's tip inside the cytoplasm (ii); injection of 150mM KCl into the cytoplasm (iii-iv); CNP tip withdrawn from the cell (v). (B) ΔCeq (lower red trace) and ΔRe(Z) (upper blue trace) as functions of time during cytoplasmic penetration and microinjection events. (C) Micrographs of the CNP tip position relative to the cell nucleus: CNP outside (above) the cell (i); CNP's tip

in the nucleus (ii); nucleus is injected with 150mM KCl solution (iii-iv); CNP withdrawn from the cell (v). (D) ΔCeq (lower red trace) and ΔRe(Z) (upper blue trace) as functions of time during the nuclear penetration and injection. The cell (A) and the nucleus (C) are outlined with dotted lines for better visibility.

Figure 11 B and D depict the measured ΔC_{eq} (lower red trace and LHS ordinate) and ΔRe(Z) (upper blue trace and RHS ordinate) as functions of time during penetration, injection, and post injection into the cytoplasm (Figure 11B) and the nucleus (Figure 11D). There was a slight upward drift in the extracellular capacitance signal prior to cell penetration. No such drift was observed in Re(Z). We used the extracellular values after the CNP was withdrawn from the cell as the reference. Upon CNP penetration into the cytoplasm and the nucleus, the capacitances dropped, respectively, by -3.2pF and -4.5pF relative to the CNP's capacitance when in the extracellular solution. Concurrently, Re(Z) increased, respectively, by 540kΩ and 750kΩ upon cytoplasm and nucleus penetration relative to the extracellular values. After the cell and nucleus penetration, we observed a gradual swelling of the cell and nucleus, which was most likely caused by slow ejection of liquid from the CNP, induced by the CNP's control pressure. In our setup, during the nucleus penetration experiments, due to the close proximity of the nucleus to the cell membrane for adherent cells, it was not possible to detect the intermediary state after penetration of the cell membrane, but prior to penetration of the nuclear membrane.

The femtoinjector applied a pressure pulse to the CNP to inject solution into the cell and nucleus (two different cells) at time t~30s (Figure 11B) and time t~20s (Figure 11D), respectively. The injection caused a rapid swelling of the cell and nucleus. The injection into the cytoplasm resulted in a +0.6 pF pulse in ΔC_{eq} and a -120kΩ pulse in ΔRe(Z). The injection into the nucleus resulted in a +0.9 pF pulse in ΔC_{eq} and a -130kΩ pulse in ΔRe(Z). The pulses in ΔC_{eq} and ΔRe(Z) likely may have been caused by alterations in the CNP tip's local ionic environment, membrane swelling, and physiological changes in the cell triggered by the injection event. An interesting question, which we defer to future work, is whether the magnitude of the "injection pulse" correlates with the injection volume. ΔC_{eq} and ΔRe(Z) assumed steady values post injection. These corresponded, respectively, to ΔC_{eq} = -0.5pF and -0.7pF for cytoplasm and nucleus, relative to the extracellular values after CNP removal. The corresponding ΔRe(Z) were 98kΩ and 120kΩ. Steady state was reached faster for the nuclear injection, presumably due to the smaller volume of the nucleus. Upon removal of the CNP from the cell, both C_{eq} and Re(Z) resumed stable extracellular baseline values.

The steadiness of the impedance measurements when the CNP tips were embedded in the cytoplasm and the nucleus suggests that the CNP penetration, injection, and dwelling in the cell and nucleus did not significantly compromise the cell and nuclear membranes. This is consistent with prior work (Schrlau, 2009; Schrlau, Brailoiu, et al., 2008; Schrlau et al.,

2009; Schrlau, Falls, et al., 2008), which demonstrated that probing cells with CNPs and injecting secondary messengers into the cytoplasm did not harm cells. Furthermore, the CNPs can be used to record electrically significant events in the cell and nucleus for prolonged periods of time.

2.3.6 Cytoplasm vs. Nucleus Penetration

When measuring CNP's equivalent capacitance during cell and nucleus penetration with empty CNPs, we found a significant difference between the signal associated with cytoplasm penetration, $\Delta C_{eq,CP}$ (-30.6±17.4fF, N=138), and the signal associated with nuclear penetration, $\Delta C_{eq,N}$ (-43.8±17.7fF, N=133), P<0.0001. For the real part of the impedance, $\Delta Re(Z)_{CP}$=85.0±46.7kΩ (N=138) and $\Delta Re(Z)_{N}$=86.9±87.1kΩ (N=133) the difference was not significant. In the above, subscripts 'CP' and 'N' refer, respectively, to cytoplasm and nucleus. The ratio $\Delta C_{eq,N}$ /$\Delta C_{eq,CP}$ ~ 1.4 while $\Delta Re(Z)_{N}/\Delta Re(Z)_{CP}$ ~1. The nuclear membrane does not significantly increase the real part of the impedance at the frequency used in our experiments.

Figure 12A and B depict, respectively, the distributions of $\Delta C_{eq}^{1/2}$ associated with the penetration into the cytoplasm and into the nucleus. We selected to analyze the data in terms of $\Delta C_{eq}^{1/2}$ instead of ΔC_{eq} because the former could be better fitted with a Gaussian distribution. We fit these probability distributions with Gaussian distributions (solid lines) with R^2 values of 0.93 (Cyto.) and 0.98 (Nuc.). Figure 12C compares the probability distributions associated with cytoplasm and nucleus penetrations and shows

them to be distinct (P<0.0001). The differences in $\Delta C_{eq,CP}$ and $\Delta C_{eq,N}$ are due to the nuclear membrane's impedance. Variations in the biological state of different cells, penetration depth of the CNP, and tolerances of the CNPs make it difficult to determine whether the tip is in the cytoplasm or nucleus based on a single impedance measurement, as is evident from the overlap of the distributions in Figure 12C. When using a well-calibrated pipette and penetrating to a consistent depth, the signal magnitude can, however, be used to distinguish between cytoplasm and nuclear penetration.

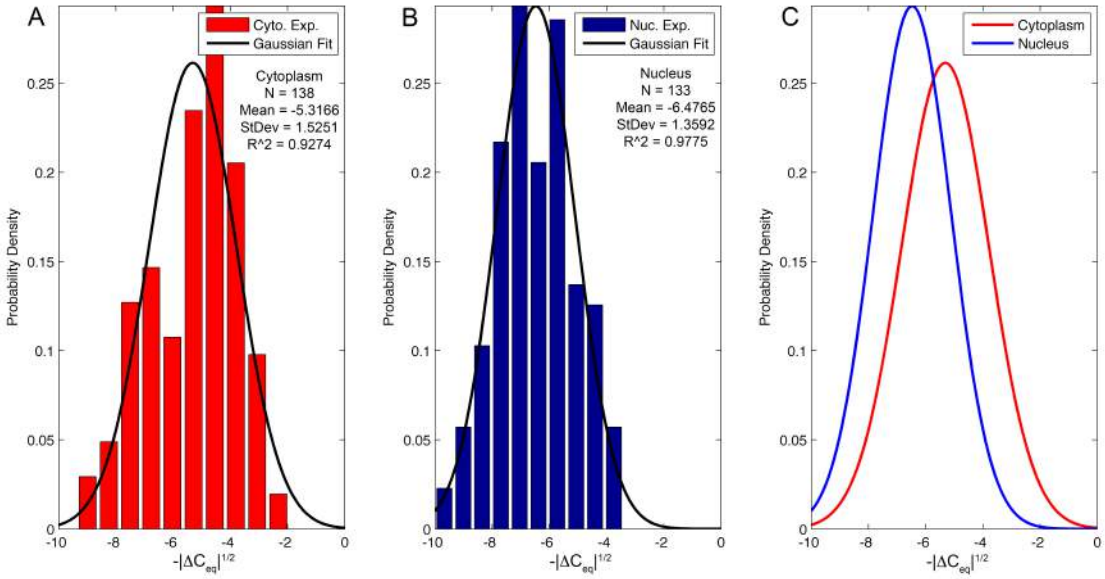

Figure 12. Distribution histograms of cellular probing data (bars) for cytoplasm (N=138) (A) and nucleus (N=133) (B) with Gaussian fits (solid lines). (C) Comparison between the Gaussian fits from (A) and (B). The y-axis data is normalized to produce a probability density function and the x-axis is the square root of the capacitance change.

We also found a significant difference between the ΔC_{eq} associated with cytoplasm and the ΔC_{eq} associated with nuclear penetration ($P<0.0001$) for microinjection studies. When the liquid-filled CNP (150mM KCl) penetrated the cell (subscript 'CP') and the nuclear membrane (subscript 'N'), $\Delta C_{eq,CP}$ (± one standard deviation) = -5.8±2.7pF (N=28) and $\Delta C_{eq,N}$ =-9.1±3.9pF (N=31). The corresponding changes in the real part of the impedance were $\Delta Re(Z)_{CP}$ = 670±387kΩ and $\Delta Re(Z)_N$ = 1020±591kΩ. The ratios $\Delta C_{eq,N}$ /$\Delta C_{eq,CP}$ ~ 1.56 and $\Delta Re(Z)_N/\Delta Re(Z)_{CP}$ ~1.52.

Similarly to cell probing with empty CNPs, the differences in $\Delta C_{eq,CP}$ and $\Delta C_{eq,N}$ during microinjection are due to the nuclear membrane's impedance. Variations in the biological state of different cells, penetration depth of the CNP, and tolerances of the CNPs make it difficult to determine whether the tip is in the cytoplasm or nucleus based on a single impedance measurement, but under controlled conditions the location can be obtained based on signal amplitude.

2.3.7 Effect of Penetration Depth

To examine the change in the equivalent capacitance as a function of the CNP tip's penetration depth into the cell, we programmed the piezoelectric micromanipulator to traverse downwards at a uniform speed (400 nm/s) until after the cell was penetrated. The CNP impedance was continuously monitored during these experiments. Knowledge of the rate of descent allowed us to infer the distance travelled.

Figure 13 depicts ΔC_{eq} (fF) of an empty CNP (hollow squares, backpressure of 400 kPa) contrasted with a CNP filled with extracellular solution (stars, ×0.1) as well as $\Delta Re(Z)$ of an empty CNP (kΩ, upright triangles, 400 kPa backpressure) as functions of the CNP penetration depth (d μm) into the cytoplasm of a cell. The symbols and solid curves represent, respectively, experimental data and theoretical predictions. The error bars correspond to one standard deviation (N=10). To accommodate the data for the liquid-filled (stars) and empty (hollow squares) CNPs in the same graph, we multiplied the values of ΔC_{eq} associated with the liquid-filled CNP by the factor 0.1. At zero depth, the CNP's tip is fully in the extracellular solution. As d increases, the fraction of the exposed tip embedded in the cell, $|\Delta C_{eq}|$, and $\Delta Re(Z)$ increase as well.

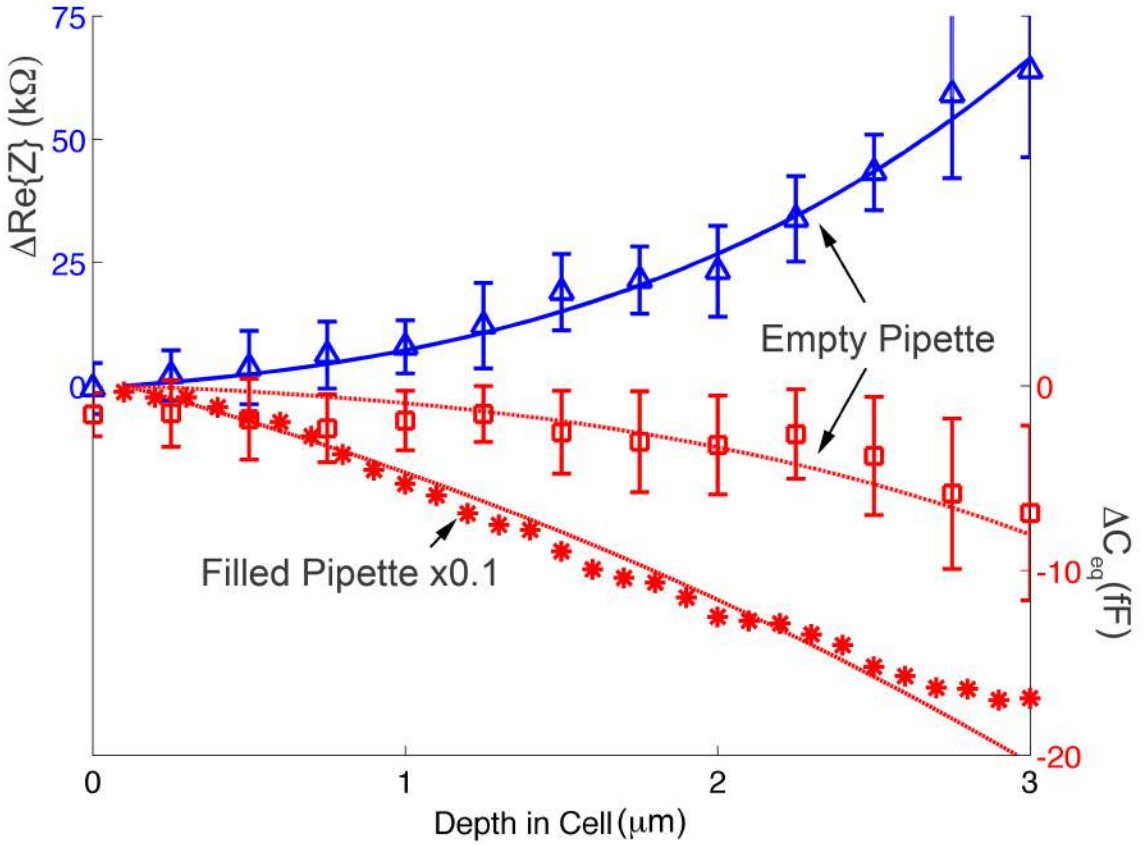

Figure 13. The real part of the change in the impedance ΔRe(Z) (blue triangles, empty CNP, n=10), ΔC_{eq} (red hollow squares, empty CNP, N=10), and ΔC_{eq} (red stars, liquid-filled CNP, N=1) are depicted as functions of the cell penetration depth (d μm) into the cytoplasm. The symbols and lines represent, respectively, experimental data and theoretical predictions.

$|\Delta C_{eq}|$ and ΔRe(Z) increased monotonically with the penetration depth (Figure 13). We used the full network-based model that includes the various resistances (Figure 8A) to predict ΔC_{eq} and ΔRe(Z) as functions of the penetration depth (solid lines). In the model, we used reported values of cell membrane capacitance (Hamill, Marty, Neher, Sakmann, & Sigworth, 1981),

and resistance (Johnson & Woodbury, 1964), and theoretical values for the diffuse layer capacitance based on Gouy-Chapmann-Stern (GCS) theory (Bard & Faulkner, 2000). We modeled the CNP geometry as a simple truncated cone. The model for the empty CNP required just one fitting parameter: the CNP's Stern layer capacitance, which we estimated as 30μF/cm^2. This estimate is on the same order of magnitude as the documented (H. N. Wang & Pilon, 2011) Stern layer capacitance of 40μF/cm^2 for a spherical microelectrode submerged in a KCl solution, and roughly half that predicted by GCS theory (~65 μF/cm^2). In the case of the liquid-filled CNP, a second fitting parameter was needed to approximate the effective inner surface of the CNP in contact with the liquid. The theoretical predictions agree well with the experimental data (symbols). Consistent with our previous observations, the liquid-filled CNPs exhibited much greater $|\Delta C_{eq}|$ than the empty ones. The ability to estimate the CNP tip's penetration depth may be useful to minimize cell damage as well as to control the position of the electrode tip for intracellular sensing.

The simplified model for the capacitance variations (Equation 18) approximates well the predictions of the full circuit model for Im(Z). Although the increase in Re(Z) with penetration depth is consistent with intuition, we were not been able to come up with a simple model to predict Re(Z) as a function of d. Instead, we have to rely on the predictions of our full circuit model (Figure 8A).

The spatial resolution of this technique depends on electrode geometry, amplifier characteristics, and the micromanipulator's resolution. Our micromanipulator step size limits our maximum resolution to 40nm and our amplifier noise level was measured to be 2.0fF. Once the probe is in the cytoplasm, we anticipate being able to detect penetration depth within 130nm. This estimate does not account for membrane indentation and possible cell remodeling during penetration. It is also important to appreciate the inherent variability of biological samples. Careful optimization and calibration would be necessary to use this technique in a quantitative (measuring penetration depth) rather than qualitative (detecting and minimizing penetration depth) manner.

2.3.8 Effect of Pressure on CNP Capillary Uptake

Since the carbon film inside the CNP is typically uninsulated from the liquid inside the CNP, the presence of liquid inside the CNP increases the electrode's effective area and affects the characteristics of the electrode. The hollow of the CNP may be completely or partially filled with solution. When an unpressurized, empty CNP is introduced into a solution, liquid will fill the hollow of the CNP by capillary imbibition. The electrode's increased interfacial area due to the presence of liquid in the CNP's hollow increases the EDL capacitance. Thus, when a liquid-filled CNP penetrates a cell, a much larger change in the equivalent capacitance is detected than when an

empty CNP is used. The extent of the liquid imbibition into the CNP can be modified by adjusting the control pressure.

When control pressure is applied, this pressure counteracts the Laplace pressure at the fluid/air interface (Berg, 2010)

$$\Delta P = \frac{2\gamma}{r_b}$$

Equation 19.

where ΔP is the pressure difference across the interface (meniscus), γ is the surface tension, and r_b is the radius of the CNP's bore at the location of the interface. Since the capacitance change is proportional to the wetted area and the CNP's tip is conical, we expect $C_{eq} \sim 1/P^2$, where P is the control pressure. Below, we assume that only a part of the conical section of the CNP's bore is filled with solution. Figure 14 depicts the measured C_{eq} as a function of $1/P^2$ for a characteristic CNP submerged in PBS buffer 1X (Hyclone). As expected, C_{eq} varies nearly linearly with $1/P^2$. Linear behavior with $1/P^2$ was consistent among all CNPs tested (N=5), with an average R^2 value of 0.96. When we extrapolate the data of Fig. 6 to $P \rightarrow \infty$, we find less than a 2% difference, on average (5 CNPs), between the extrapolated value of C_{eq} at $P \rightarrow \infty$, and the value at the working pressure. We consider the pressure sufficiently high to render capillary effects insignificant. This characterization could be useful in applications that require uptake of liquids by capillary action, for example in electrochemical nanosamplers (Yu et al., 2014), or to characterize the internal geometry near the CNP's tip.

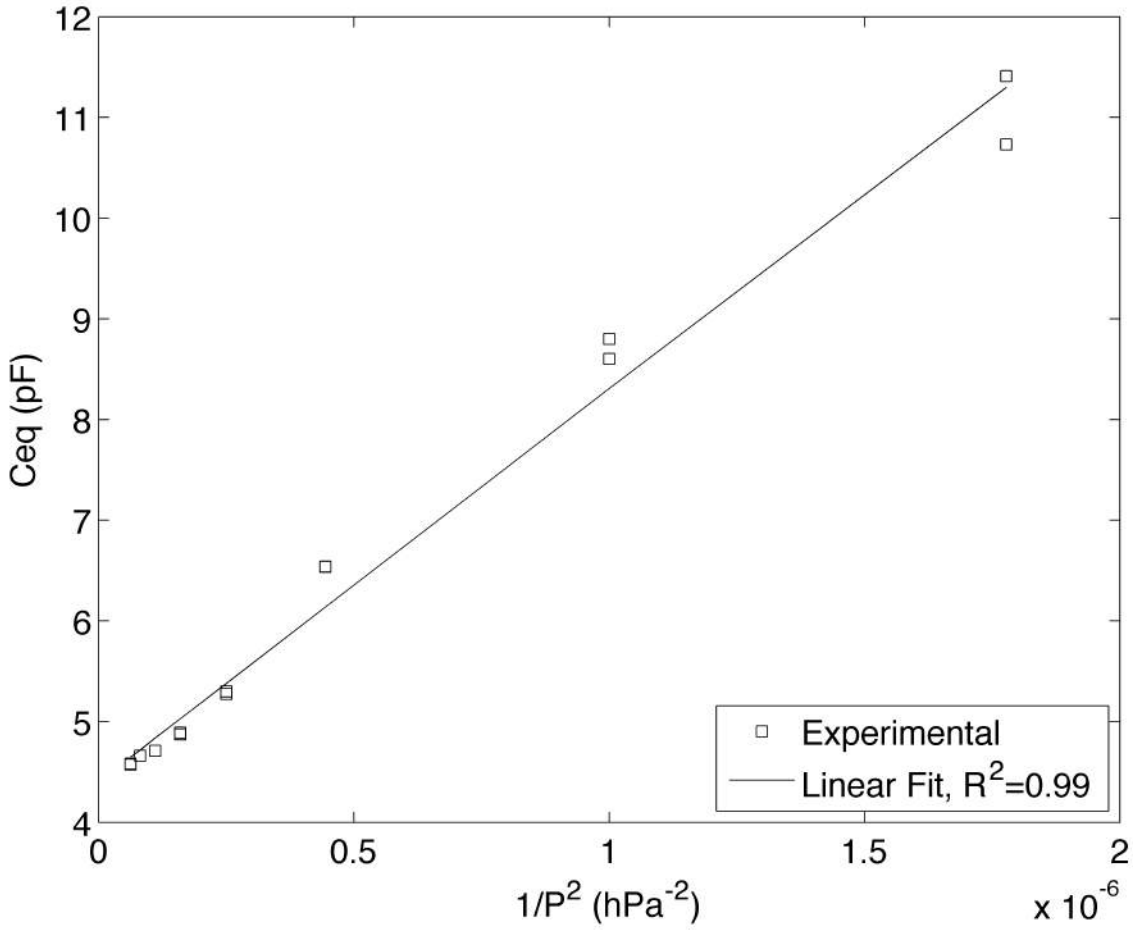

Figure 14. The equivalent CNP's capacitance Ceq as a function of P^{-2}, where P is the control pressure. The symbols and the line represent, respectively, experimental data and the best linear fit.

2.4: Conclusions

Reliable, controllable, high throughput methods for cell injection are critical for, and are the bottleneck in, many important projects in biomedical research. To enable high throughput automated injection, it is desirable to detect cell penetration to trigger the injector. The electrical monitoring of CNP impedance provides a relatively simple means to detect cell penetration. Since CNPs have independent paths for electrical signal monitoring through

their carbon lining and for injection through their hollow bore, they are uniquely suitable for automated injection. Unlike other proposed electrical detection methods for cell penetration, the CNPs do not rely on the injection liquid itself to provide the conductive path. Additionally, the CNPs provide smaller dimensions, improved biocompatibility, and better optical contrast for visual feedback during micromanipulation than traditional pulled glass pipettes and much greater controllability than cell transfusion techniques based on cell membrane poration and vectors. There is also a pressing need for methods to place nanoelectrodes into cells with high precision and minimal invasiveness for intracellular measurements.

We have demonstrated that CNPs can robustly detect cellular and nuclear penetration through an impedance measurement. By applying a kHz-frequency potential difference between the CNP and a counter electrode submerged in the extracellular solution, we attain stable, low-noise impedance measurements with time resolution <1 ms, without a need to rely on a redox mediator in the extracellular solution or high concentration ionic electrolyte in the injection pipette. Trends in the experimental observations are predicted well with a simple, equivalent circuit model. Although a redox mediator is not necessary for our measurements, one could be employed as an alternative means for penetration detection if desired.

Data collected from many microinjection events demonstrates that there is a statistically significant difference between capacitance signal

magnitudes when probing the cytoplasm of a cell versus the nucleus, with an average difference of 3.3pF for 150mM KCl solution-filled CNPs and 13.2fF for empty CNPs. We also found that the signal from CNP nanoelectrodes correlates monotonically with penetration depth, and follows expected trends for capillary nanosampling, which could provide improved capabilities for single-cell electrochemical nanosamplers. The proposed measurement technique is reliable and stable, can be used with any composition or volume of injection solution, and can be applied for most, if not all, mammalian cell types. We anticipate such technology to significantly advance microinjection reliability and throughput, as well as nanoelectrode placement for noninvasive intracellular recording. This work has been disseminated in two publications in *Nanotechnology* (S. E. Anderson & Bau, 2014; Sean E. Anderson & Bau, 2015).

Chapter 3: CNP Electrodes (CNPEs) for Neurotransmitter Detection in *Drosophila Melanogaster*

3.1 Attribution

The work in this chapter was performed in collaboration with Professor B. Jill Venton's lab at the University of Virginia, Department of Chemistry. Hillary R. Rees (MS, UVA Dept. of Chemistry) and Eve Privman (MD/PhD Candidate, UVA Dept. of Chemistry and Neuroscience Graduate Program) performed CNPE electrochemical characterization for sensitivity, stability, and waveform optimization for neurotransmitter detection. Eve Privman performed all *in vivo Drosophila* studies. I performed initial feasibility studies for dopamine detection, and fabricated, tested, and characterized CNPEs used in experiments using optical microscopy, electron microscopy, and capacitance measurement. I directly contributed Figure 15, Figure 16, and Figure 21B; the Venton lab contributed all other figures in this chapter. This work was published in *Analytical Chemistry* (Rees, Anderson, Privman, Bau, & Venton, 2015), and all authors contributed to writing and editing the resulting manuscript.

3.2: Background

Carbon-fiber microelectrodes (CFMEs) are traditionally used with fast-scan cyclic voltammetry (FSCV) to study rapid neurotransmitter changes *in vivo* (Robinson, Hermans, Seipel, & Wightman, 2008). They allow real-time detection of catecholamines with high sensitivity and selectivity. Traditional CFMEs are 7 μm in diameter (Chadchankar & Yavich, 2012); however, smaller electrodes would be useful for neurochemical studies in small organisms such as *Drosophila melanogaster* (the fruit fly). The larval fly central nervous system is extremely small, only about 100 μm wide and the brain is about 8 nL in volume (Vickrey, Condron, & Venton, 2009). Individual neuropil, or brain regions, of the adult fly are only a few microns in diameter (Kahsai & Winther, 2011; Mao & Davis, 2009). *Drosophila* is a convenient model organism because it has homologous neurotransmitters with mammals and is easy and fast for genetic manipulation. CFMEs have been used to make electrochemical measurements of exogenously applied dopamine in the adult fly mushroom body (Makos, Kim, Han, Heien, & Ewing, 2009). In addition, endogenous, stimulated dopamine changes have been measured in a single fruit fly larva (Vickrey et al., 2009). *Drosophila* have glial sheaths surrounding their neuropil that can be tough to penetrate. In larvae, a cut surface is made to insert the electrode (Vickrey et al., 2009; Vickrey & Venton, 2011; N. Xiao, Privman, & Venton, 2014; N. Xiao & Venton, 2012),

and in adults, collagenase has been applied to chemically digest the tissue (Makos, Han, Heien, & Ewing, 2009; Makos, Kim, et al., 2009). Therefore, studying the release of endogenous neurotransmitters with better spatial resolution requires a small, dagger-like electrode that can penetrate through the tough glial sheath barrier with minimal tissue damage. Although CNPs have not been previously tested with intact brain tissue, they have been used to penetrate individual mammalian cells while retaining cell viability (Schrlau, Falls, et al., 2008; C. Wang, Chen, Wang, & Hu, 2005). Hence, it is reasonable to expect that the CNPs can penetrate the brain tissue without causing significant damage.

Over the past few decades, nanoelectrodes have been developed for electrochemical applications. Carbon electrodes are preferred for neurotransmitter applications because of their low cost, wide potential window, and good adsorption properties (McCreery, 2008). To make smaller electrodes, carbon fibers can be either flame etched or electrochemically etched to sub-micron tips (W.-H. Huang, D.-W. Pang, H. Tong, Z.-L. Wang, & J.-K. Cheng, 2001; Kawagoe, Jankowski, & Wightman, 1991; Strand & Venton, 2008; Strein & Ewing, 1992). Carbon nanomaterials, such as nanotubes, can also be used as smaller electrodes. Carbon nanofiber microelectrodes have been developed for neurotransmitter detection, but they are on a larger chip and not easily implantable (Koehne et al., 2011). Small carbon paste electrodes have been made for scanning electrochemical

microscopy studies, but are not easy to batch fabricate (Satpati & Bard, 2012). Tiny, nanometer-sized electrodes have been made using a single-walled carbon nanotube either sticking out (Campbell, Sun, & Crooks, 1999) or on a silicon wafer (Heller et al., 2005). Alternatively, some methods completely insulate an etched carbon fiber except for the very tip leaving an effective diameter of a few nanometers (S. Chen & Kucernak, 2002; C. Wang et al., 2005). However, insulation is difficult and a single carbon nanotube or nanometer-sized fiber is not robust enough to be implanted into tissue.

For *in vivo* measurements in *Drosophila*, we desire a sharp, carbon nanoelectrode with high sensitivity to detect nanomolar concentrations that can be easily batch fabricated. Carbon nanopipette electrodes (CNPEs) are nanometer sized electrodes, which have been previously used for electrophysiological measurements and delivering fluids into cells (Schrlau et al., 2009; Schrlau, Falls, et al., 2008; Vitol et al., 2009). CNPEs are fabricated by selectively depositing a carbon layer on the inside of a pulled-quartz capillary. The capillary is then chemically etched to expose the carbon tip. CNPEs are batch-fabricated in a furnace and are rigid because of the quartz insulation. While many of our past designs consisted of hollow pipettes, allowing for drug delivery to cells, extending the carbon deposition time can lead to a sealed, solid tip with a 50-400 nm diameter. Recently, CNPEs with recessed tips have been evaluated as nanosamplers and scanning

electrochemical microscopy tips (Yu et al., 2014). Here, solid-tipped, cylindrical CNPEs and FSCV are coupled for the first time.

The objective of this study was to characterize the electrochemical properties of CNPEs using FSCV for the detection of dopamine and test their suitability for measurements in Drosophila. We use three parameters to define the truncated cone geometry of the CNPE tip: the tip diameter, exposed length along the pipette axis, and cone angle. Tip diameter affects invasiveness, cone angle affects sharpness and rigidity, and the exposed length controls the electrode interfacial surface area. The CNPEs used here were approximately 250 nm in diameter at the tip with exposed carbon length ranging from 5 μm to 175 μm. Dopamine current was stably detected with CNPEs with an optimized triangular waveform of -0.4 V to 1.3 V at a scan rate of 400 V/s and a frequency of 10 Hz. The current was linear with dopamine concentration up to 10 μM. CNPEs are sharp and robust enough to successfully penetrate into a *Drosophila* larva central nervous system without breaking and endogenous, stimulated dopamine release could be measured. CNPEs coupled with FSCV will facilitate fast, real-time measurements of dopamine in specific brain regions of the *Drosophila*.

3.3: Experimental

3.3.1 Solutions and Chemicals

All reagents were purchased from Fisher Scientific (Fair Lawn, NJ) unless otherwise specified. Dopamine hydrochloride, serotonin hydrochloride,

and octopamine hydrochloride was purchased from Sigma-Aldrich (St. Louis, MO). Each neurotransmitter was dissolved in 0.1M $HClO_4$ for a 10mM stock solution and diluted daily in phosphate buffered saline (PBS) for testing. The PBS was 131.25 mM NaCl, 3.0 mM KCl, 10.0 mM NaH_2PO_4 monohydrate, 1.2 mM $MgCl_2$ hexahydrate, 2.0 mM Na_2SO_4 anhydrous, and 1.2 mM $CaCl_2$ dihydrate with the pH adjusted to 7.4. Sodium chloride was purchased from VWR International LLC (West Chester, PA), sodium phosphate from Ricca Chemical Company (Arlington, TX) and calcium chloride from Sigma-Aldrich. All aqueous solutions were made with deionized water (Milli-Q Biocel, Millipore, Billerica, MA).

3.3.2 Carbon Nanopipette Electrode Fabrication

CNPEs were fabricated with 1 mm outer diameter, 0.7 mm inner diameter, filamented quartz capillaries of 10 cm length (Sutter Instrument Co., Novato, CA) or 1mm outer diameter, 0.8mm inner diameter non-filamented quartz capillaries (VitroCom, Mountain Lakes, NJ). Pipettes were pulled using a Sutter P-2000 laser-based pipette puller with the parameters: HEAT 800, FIL 4, VEL 60, DEL 128, and PULL 100 (1x0.7mm filamented) or HEAT 750, FIL 4, VEL 50, DEL 150, PULL 55 (1x0.8mm non-filamented). Chemical vapor deposition (CVD) was performed on the pipettes in a 3-zone horizontal tube furnace (Carbolite HVS, Hope Valley, UK) with a 1.3" inner diameter quartz tube at 900 °C, with flow conditions of 400 sccm methane and 600 sccm argon, for a 3 hour duration. During deposition, the pipette tips

were oriented against the flow of the gas, i.e., the tip pointed upstream. Pipettes were cooled under argon flow to prevent the oxidation of the carbon at elevated temperatures The carbon deposited selectively inside the pipette, not on the outer surface due to the gas confinement effect described by Singhal et al (Singhal et al., 2010). No catalyst was used.

The carbon-coated pipettes were etched in 5:1 buffered hydrofluoric acid (Transene Co. Inc., Danvers, MA) for 10 to 15 minutes followed by a 10-minute rinse in deionized water. A friction grip was used to hold pipettes, and a manual manipulator was used to lower the tips into beakers of either HF or water. Short CNPEs for use in the Drosophila larval ventral nerve cord were prepared by lowering the etch time to 60 seconds. The pipettes were inspected under an optical microscope (Olympus Corp. BX-51) and imaged with a SEM (FEI Quanta 600 ESEM, Hillsboro, OR). The tip outer diameter ranged from 50 to 400 nm and the exposed carbon tip length depended on the etch time and tolerances of the pipette puller, but typically was 125-175 μm for etch times of 10 minutes and 5-10 μm for 1 minute. For additional details on CNP fabrication we refer readers to the following references (Kim et al., 2005; Schrlau, Falls, et al., 2008; Singhal et al., 2010).

To ensure the pipettes were properly sealed, CNPEs were connected to the headstage of a HEKA EPC 10 patch-clamp amplifier using a standard 1.0mm HEKA pipette holder. The pipettes were also connected to a pressure-injection pump (Eppendorf Femtojet, Happauge, NY). The CNPE tip was

submerged in phosphate buffered saline (HyClone, PBS1X) and a silver chloride wire was used as a counter/reference electrode in solution in a 2-electrode configuration. The digital lock-in module of the PATCHMASTER software was used to measure the equivalent capacitance of the CNPE interface with a 10mV, 1kHz sinusoidal potential, as the pressure within the pipette was adjusted between 0 and 300 kPa. The tip was first checked for bubbles, which would indicate a completely broken tip, and then the capacitance was monitored with changing pressure. The capacitance is proportional to the electrode interfacial area, and if it is stable with varying pressure it indicates that there is minimal capillary rise and that the tip is well-sealed. CNPEs that were not well sealed were discarded.

3.3.3 Scanning Electron Microscopy

Scanning electron microscopy was performed in a FEI Quanta 600 ESEM (FEI, Hillsboro, Oregon) in secondary electron mode. CNPEs were adhered to a standard sample mount with carbon tape such that the CNPE axis was orthogonal to the electron beam. A short working distance (5mm) and low accelerating voltage (2 keV) were used in high-vacuum mode to attain enhanced surface detail and to minimize charging effects.(Joy & Joy, 1996) The Environmental SEM provides a large sample chamber that allows CNPEs to be mounted without breaking or modification.

3.3.4 Instrumentation and Electrochemistry

Preliminary studies were performed using CNPEs mounted on a HEKA EPC 10-2 headstage via a standard 1.0mm coupling. Fast-scan cyclic voltammograms were attained at 400V/s, 10Hz, with a waveform from -400 to +1000 mV vs. Ag/AgCl/Cl^- using HEKA PATCHMASTER software, which was then exported to Matlab for post-processing. Phosphate Buffered Saline (PBS, HyClone) and PBS spiked with dopamine were loaded into a Scientific Instruments ALA-VM4 perfusion system. The CNPE was placed in a flow cell and perfused with PBS while recording. After equilibration the flow was switched to the PBS/dopamine mixture, and then switched back to PBS for rinsing. Background subtraction and plotting were performed in post-processing.

CNPEs were transferred to UVA for further characterization and studies. Here, fast-scan cyclic voltammograms were collected using a Chem-Clamp potentiostat (Dagan, Minneapolis, MN). TarHeel CV software (gift of Mark Wightman, University of North Carolina) was used for data collection and analysis. The hardware and data acquisition were the same as previously described.(Heien, Phillips, Stuber, Seipel, & Wightman, 2003) A triangular waveform was applied to the electrode. The electrode was scanned at a scan rate of 400 V/s from -0.4 V to 1.3 V and back at a frequency of 10 Hz unless otherwise noted. A Ag/AgCl wire was used as a reference electrode. The flow injection apparatus with a six-port, stainless steel HPLC loop injector used is

the same as previously described (Huffman & Venton, 2008). Electrodes were tested with a 5 s injection time. Because carbon is deposited on the entire length of the CNPEs, a direct electrical connection was made with a silver wire in the Universal Pipette Holder (HB180, Dagan Corp., Minneapolis, MN). No backfill solution was used. The holder was connected to a 1 MΩ headstage (Dagan Corp., Minneapolis, MN).

3.3.5 Endogenous Dopamine Evoked by CsChrimson Channelrhodopsin Stimulation

Virgin females with UAS-CsChrimson inserted in attp18 (Klapoetke et al., 2014) (a gift of Vivek Jayaraman) were crossed with th-GAL4 flies (a gift of Jay Hirsh). Resulting heterozygous larvae were shielded from light and raised on standard cornmeal food mixed 250:1 with 100 mM all-trans-retinal. A small amount of moistened Red Star yeast (Red Star, Wilwaukii, WI) was placed on top of the food to promote egg laying. The central nervous system of a third instar wandering larva was dissected in the buffer. Isolated ventral nerve cords were prepared and recorded from as previously described (Borue, Cooper, Hirsh, Condron, & Venton, 2009). The electrode was allowed to equilibrate in the tissue for 15 minutes prior to data collection. A baseline recording was taken for 10 seconds prior to stimulation. Red-orange light from a 617 nm fiber-coupled high-power LED with a 200 μm core optical cable (ThorLabs, Newton, NJ) was used to stimulate the CsChrimson ion channel. The light was modulated with Transistor-Transistor Logic (TTL) inputs to a

T-cube LED controller (ThorLabs, Newton, NJ), which was connected to the breakout box. TTL input was driven by electrical pulses controlled by the TarHeel CV software.

3.3.6 Statistics

Statistics were performed using GraphPad Prism 6.0 (GraphPad Software, San Diego, CA). Data are reported as the mean ± standard error of the mean (SEM) for n number of different electrodes. Significance was determined by unpaired *t*-tests and defined as $p \leq 0.05$.

3.4: Results and Discussion

Preliminary feasibility studies were carried out to determine if CNPEs could be used for FSCV of dopamine. A custom flow cell and a patch-clamp amplifier were used to acquire fast-scan data from a CNPE as the flow solution was changed between buffer and buffer/dopamine. The data was exported to Matlab where background-subtraction and pseudo-color plots of the current were generated, as shown in Figure 15. The preliminary data demonstrated clear detection of dopamine, minimal background and noise, clear redox peaks, and sensitivity at the sub-micromolar level. This led to collaboration with the Venton lab at UVA who specialize in Fast Scan Cyclic Voltammetry, for characterization and *in vivo* studies with CNPEs.

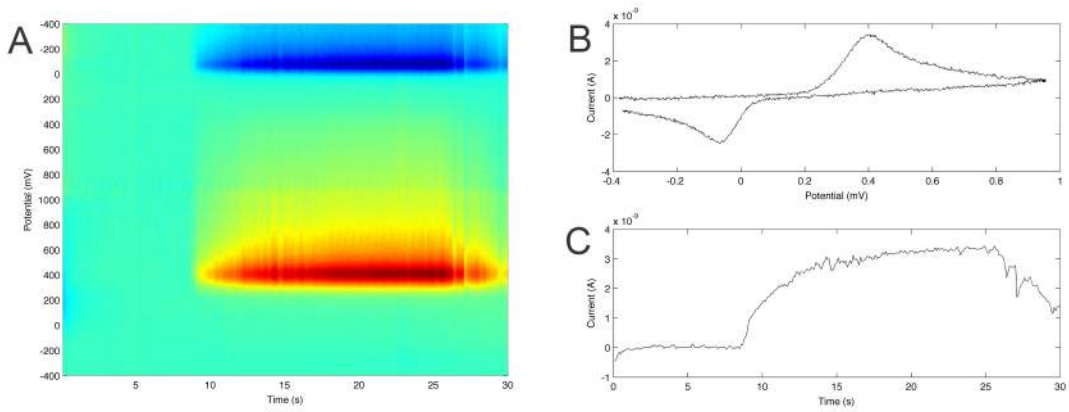

Figure 15.Preliminary CNP FSCV data, 5µM dopamine in PBS1X. Dopamine introduced at t=10s, and stopped at t=25s. (A) Color plot of dopamine detection, red is the oxidation current, blue is the reduction current. (B) Sample cyclic voltammogram demonstrating peaks near +400mV and -75mV vs. Ag/AgCl/Cl-. (C) Oxidative peak current over time, which is proportional to dopamine concentration.

The first goal of this study was to electrochemically characterize CNPEs using FSCV. FSCV allows measurements of rapid changes in neurotransmitter concentrations. CNPEs have traditionally been manufactured with open tips (Schrlau, Falls, et al., 2008), but that is not suitable for rapid electrochemistry as sample would wick up into the pipette. Here, the fabrication was modified slightly to grow enough carbon to make an electrode with a solid tip ~250 nm in diameter. The second goal was to test the suitability of CNPEs for dopamine measurements in *Drosophila* larvae, which have a very small central nervous system. This nanoscale electrode would allow for high spatial resolution measurements.

3.4.1 Fabrication of Carbon Nanopipette Electrodes

The carbon nanopipette electrode (CNPE) consists of a pulled-glass/quartz pipette coated with a layer of pyrolytic carbon along its entire inner surface to a thickness sufficient to seal the pipette's narrow opening (Figure 16). Figure 16A shows the fabrication process. First, a quartz capillary was pulled into a fine-tipped nanopipette (Figure 16A(i)). Next, carbon was deposited by CVD until the tip was sealed with carbon (Figure 16A(ii)). Further up, the carbon-coated pipette was still hollow, which facilitates electrical connection via contact with a metal wire. Subsequent to the carbon deposition, the quartz/glass at the tip of the CNPEs was etched in buffered hydrofluoric acid to expose a desired length of a tapered carbon cylinder (Figure 16A (iii)). The exposed length was controlled by the etching time. For the pipette geometry used here, this corresponds to an exposed length of 12.5-17.5 μm/minute as measured with an optical microscope and confirmed with SEM. Figure 16B shows an example CNPE tip with ~170 μm exposed carbon. The interface between the exposed carbon and the quartz insulation is clearly visible. Figure 16C is an enlarged image of the quartz/carbon interface. The tip diameter of the individual CNPEs used in this work was measured with SEM and the range of tip sizes was 50-400nm (Figure 16D), with an average of 250 nm. Since the glass/quartz template controls the outer dimensions of the deposited carbon, it is likely that the primary source of tip variability stems from the pipette puller parameters.

Even with the above variability, this fabrication method consistently yields sub-micron sized tips, an order of magnitude smaller than traditional CFMEs. All electrodes were tested for tip closure prior to use.

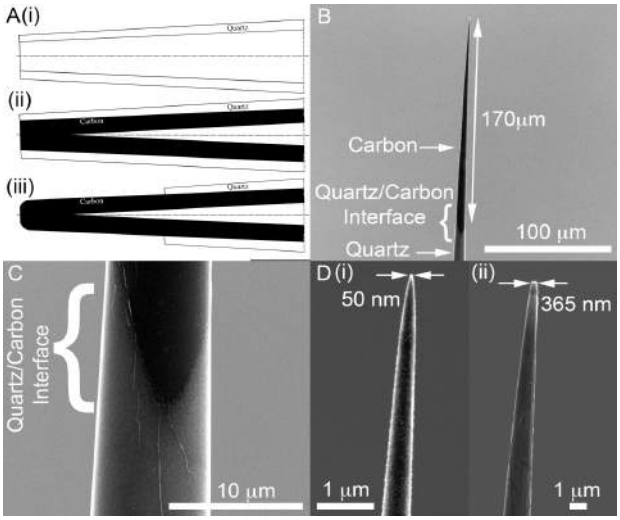

Figure 16. Carbon Nanopipette Electrodes (CNPE). (A) A schematic of the CNPE fabrication process. (i) Quartz/glass pipette is pulled to form a template. (ii) The pulled pipette is placed in a furnace in the presence of precursor hydrocarbons and carbon is deposited selectively along the pipette's interior surface for a sufficient amount of time until the tip is sealed with carbon. No catalyst was used. (iii) The glass/quartz at the tip is wet-etched to expose a desired length of the underlying carbon. (B) SEM image of the CNPE tip profile. (C) Enhanced SEM view of the quartz/carbon interface. (D) Enhanced SEM view of the CNPE tips. (i) Tip diameter 50 nm. (ii) Tip diameter 365 nm (same CNPE as in (B) and (C)). The tip and edges appear brighter due to SEM charging effects.

3.4.2 Comparison of CNPEs and CFMEs

Dopamine was chosen to analyze with CNPEs because it is an important neurotransmitter, easily oxidized, and adsorbs to carbon surfaces

(Bath et al., 2000). Dopamine plays an important role in reward, addiction, and motor behaviors (Arbuthnott & Wickens, 2007). Figure 17 shows examples of background-subtracted cyclic voltammograms (A and B) as well as normalized current vs time plots (C and D) for dopamine at two different waveforms for a CNPE (dashed line) and a CFME (solid line). The first waveform (referred to as the 1.0 V waveform) scanned from -0.4 to 1.0 V vs. Ag/AgCl/Cl^- at a scan rate of 400 V/s and a frequency of 10 Hz (A and C). The second waveform (referred to as the 1.3 V waveform) was the same as the 1.0 V waveform except the switching potential was 1.3 V (B and D). Figure 17B and D show larger currents for both CNPEs and CFMEs with the 1.3 V potential limit than the ones with the 1.0 V potential limit, as expected due to oxidation of carbon (Pavel Takmakov et al., 2010). The CFME had more current for dopamine than the CNPE for both waveforms. However, the peak oxidation voltage was lower for CNPEs (Figure 17A and B). CNPEs and CFMEs have a similar time response at the 1.3 V waveform, although CNPEs were slightly slower with the 1.0 V waveform (Figure 17C and D).

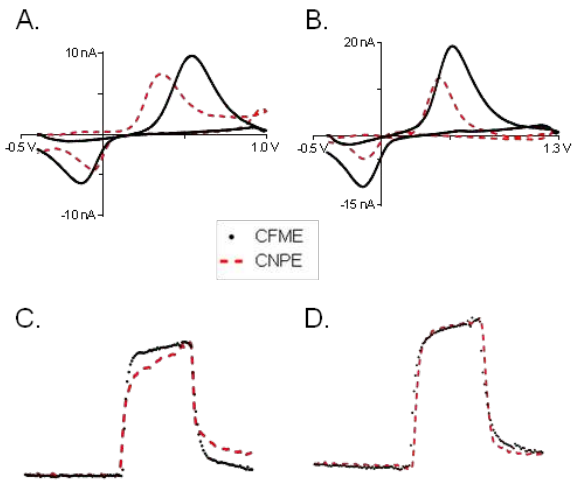

Figure 17. Example data for a 150 µm long CNPE (red dashed line) and a 50 µm long CFME (black line) with the 1.0 V and 1.3 V waveforms. Background-subtracted cyclic voltammograms for 1 µM dopamine are shown for (A) the 1.0 V waveform and (B) the 1.3 V waveform. Normalized current versus time plots at peak oxidation voltage for (C) the 1.0 V and (D) 1.3 V waveforms.

Table 1 shows average peak oxidative currents ($i_{p,a}$), background currents, and the difference between the oxidative and reductive peak potentials (ΔE_P) for CNPEs (150 µm in length, ~250 nm diameter) and CFMEs (50-75 µm in length, 7 µm diameter) at the 1.0V and 1.3V waveforms. The average peak oxidative current ($i_{p,a}$) for 1 µM dopamine is about 30% lower for CNPEs than CFMEs at both waveforms; however, the difference was not significant (unpaired t-test, 1.0 V waveform, p=0.1273; 1.3 V waveform, p=0.2353). The background currents were obtained in the absence of dopamine and compared using the maximum values during the forward scans. Background currents for CNPEs were higher than CFMEs, although

not significantly (unpaired t-test, 1.0 V waveform, p=0.2484; 1.3 V waveform, p=0.3730). Background current is proportional to electrode surface area. The 7 μm diameter, 62 μm long CFME has a surface area of 1410 μm^2, while the 150 μm long CNPE with a cone angle of 1.6° and a tip diameter of 250 nm has a surface area of 1970 μm^2. Thus, the CNPEs are about 1.4 times larger than CFMEs, which is consistent with background current ratios of 1.5 and 1.4 documented in Table 1 for the 1.0V and 1.3V waveforms, respectively. For *in vivo* measurements, the exposed carbon length was successfully reduced below 10 μm (8.2 ± 1.4 μm) by decreasing the quartz etch duration time. This size was appropriate for producing sufficient current magnitude from a highly localized region.

Table 1. Average electrochemical parameters for 1 μM dopamine detection for CNPEs and CFMEs at 1.0 V and 1.3 V waveforms.

	$i_{p,a}$ (nA)	Background current (nA)	ΔE_P (V)
CFME 1.0V[a]	11 ± 2	330 ± 70	0.69 ± 0.02
CNPE 1.0V[b]	7.4 ± 2	490 ± 110	0.50 ± 0.02[d]
CFME 1.3V[a]	19 ± 2	410 ± 80	0.66 ± 0.01
CNPE 1.3V[c]	14 ± 3	570 ± 160	0.52 ± 0.01[d]

$i_{p,a}$ is oxidative peak current; ΔE_P is the difference between the oxidative and reductive potentials. [a]n=6. [b]n=8. [c]n=11. [d] Data for CNPEs are significantly different than for CFMEs at the same waveform (p<0.0001).

A lower oxidation current correlated with lower background charging current was expected; however, this was not true for the CNPEs of the sizes

used in our experiments. The ratio of background current to peak oxidative current is significantly higher for CNPEs than CFMEs at both waveforms signifying CNPEs are less sensitive per unit area than CFMEs. At the 1.0 V waveform, CNPEs have a background current to peak oxidative current of 75 ± 10; whereas, the CFME ratio is 29 ± 4 (unpaired t-test, $p<0.005$, CNPE $n=8$, CFME $n=6$). For the 1.3 V waveform, CNPEs have a background current to peak oxidative current of 42 ± 5, and the CFME ratio is 21 ± 4 (unpaired t-test, $p<0.005$, CNPE $n=11$, CFME $n=6$). These differences in sensitivity per unit area may due to different types of carbon in CFMEs vs CNPEs or capacitative coupling with the thin quartz near the CNPE tip.

ΔE_p is the difference between the oxidative and reductive peak potentials. The average ΔE_p for CNPEs is significantly lower than CFMEs for the two waveforms (Table 1, unpaired t-test $p<0.0001$). As in the case of the CFMEs, there is no significant difference in ΔE_p for CNPEs for the 1.0 V and 1.3 V waveforms ($p=0.4010$). The decrease in ΔE_p for CNPEs compared to CFMEs implies reduced overpotential for dopamine. However, one would expect to observe higher sensitivity with lower overpotential, and the CNPEs had less sensitivity per unit area. Alternatively, the IR drop may be different for the different materials. The lower ΔE_p might also be due to differences in diffusion and adsorptive behavior due to different carbon types and geometries between the CNPEs and CFMEs. The CNPE carbon is amorphous with graphitic islands, and has surface functional groups that depend on

deposition conditions (Vitol et al., 2009). In contrast, the CFMEs are predominantly graphitic. The lower ΔE_p could be due to different functional groups or the amount of edge plane graphite sites on CNPEs, which play a role in electron transfer and adsorption reactivity (McCreery, 2008).

CNPEs were also used to detect serotonin and octopamine, which are other electroactive signaling molecules in the *Drosophila* central nervous system. Figure 18 shows examples of background-subtracted cyclic voltammograms with inserts of peak oxidation current over time for octopamine (A and B) and serotonin (C and D). The standard waveform (-0.4 to 1.3 V at 400 V/s) was applied at 10 Hz to CNPEs for octopamine detection (Figure 18A) and serotonin detection (Figure 18C). In addition, specialized waveforms previously developed for these neurotransmitters were applied, a positive waveform for octopamine detection (Cooper & Venton, 2009) (0.1 to 1.0 V and back at 600 V/s, Figure 18B) and the serotonin waveform for serotonin detection (Jackson, Dietz, & Wightman, 1995) (0.1 to 1.0 to -0.1 to 0.1 at 1000 V/s, Figure 18D). Both analytes exhibited less electrode fouling when using their respective specialized waveforms, which is indicated by a faster return of the current to baseline after removal of the analyte from the flow cell. For octopamine, a strong secondary peak is observed using the positive waveform at CNPEs (Figure 18B), whereas less secondary peak was observed when using the positive waveform with CFMEs (Cooper & Venton,

2009). This could indicate adsorption of the secondary oxidation product of octopamine to the surface of CNPE despite the positive holding potential.

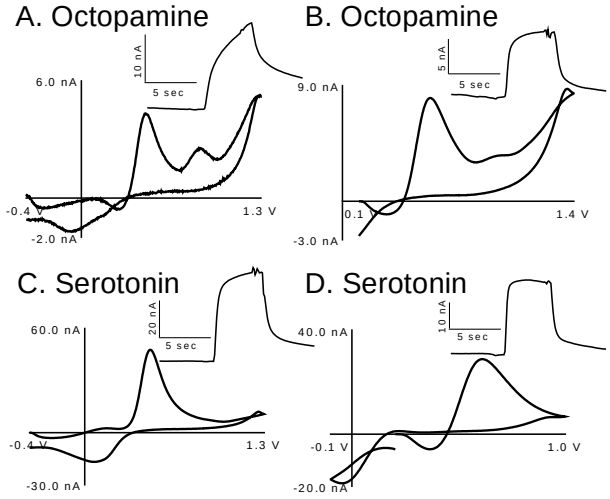

Figure 18. Example data of octopamine and serotonin detection using a 150 µm long CNPE. Background-subtracted cyclic voltammograms for 1mM octopamine are shown for (A) the 1.3 V (Dopamine) waveform and (B) the positive waveform, 0.1 to 1.4 V and back at 600 V/s. Background-subtracted cyclic voltammograms for 1 µM serotonin are shown for (C) the 1.3 V (dopamine) waveform and (D) the serotonin waveform, 0.1 to 1.0 to -0.1 to 0.1 V at 1000 V/s. The insets show current versus time plots of the main peak oxidation currents for each waveform.

The average peak oxidation current of 1 µM serotonin was 43 ± 11 nA (n=4) for CFMEs and 33 ± 2 nA (n=4) for CNPEs. The average peak oxidation current of 1 µM octopamine was 10 ± 3 nA (n=4) for CFMEs and 2.8 ± 0.2 nA (n=4) for CNPEs. The ratio of background charging current to peak oxidative current for serotonin is significantly lower for CNPEs (2.5 ± 0.4, n=4) than CFMEs (11 ± 2, n=4) (unpaired t-test, p=0.0117). However, the ratio of

background charging current to peak oxidative current for octopamine is not significantly different between CNPEs (52 ± 15, n=4) and CFMEs (31 ± 6, n=4) (unpaired t-test, p=0.2489). Therefore, CNPEs have higher sensitivity for serotonin than CFMEs, while having the same sensitivity for octopamine.

3.4.3 CNPE Stability Over Time

Electrode stability is important for *in vivo* experiments, which can last hours (Nguyen et al., 2014). To test stability, the 1.0 V waveform was applied continuously to the CNPE in buffer and the response to a five-second injection of 1 μM dopamine was measured every hour. Current was normalized for each electrode to the first response to dopamine to take into account differences in individual electrodes. Figure 19 shows that at the 1.0 V waveform, the CNPE sensitivity dropped to 32% of the original current after 3 hours. CFMEs are stable over the same time (Zestos, Nguyen, Poe, Jacobs, & Venton, 2013). The left inset shows example cyclic voltammograms taken at the first injection of dopamine and after three hours for the 1.0 V waveform. The oxidative and reductive peak voltages shifted outward, signifying slower electron transfer kinetics accompanied the decrease in sensitivity. We hypothesize the surface of the electrode is fouled which would reduce the sensitivity and slow the transfer kinetics; however, dopamine diffuses to the electrode and some current is still measured from electron tunneling.

This problem of electrode surface fouling is overcome by electrochemically renewing the surface. Scanning to 1.3 V allows for the regeneration of a fresh carbon surface and maintains electrode sensitivity (P. Takmakov et al., 2010). For the stability experiments using the 1.3 V waveform, the CNPEs were allowed to stabilize with the waveform applied for 30 minutes before taking the initial measurement due to the oxidation of the electrode surface. If not allowed to stabilize, the signal actually increases during this time due to increased surface area from carbon-carbon bonds breaking and increased adsorption due to carbon functional groups (Heien et al., 2003). The peak oxidative current was constant over three hours (Figure 19) with the 1.3 V waveform, indicating that CNPEs are stable at this waveform and suitable for longer *in vivo* studies. This is confirmed by the right inset CVs which show the sensitivity and the electron transfer kinetics remained the same after three hours. Three hours is longer than a typical *Drosophila* experiment, and some electrodes were used for much longer or in multiple larvae and showed no degradation in signal. From this stability experiment, we determined that the 1.3 V waveform was most appropriate and we used this waveform for the remaining studies.

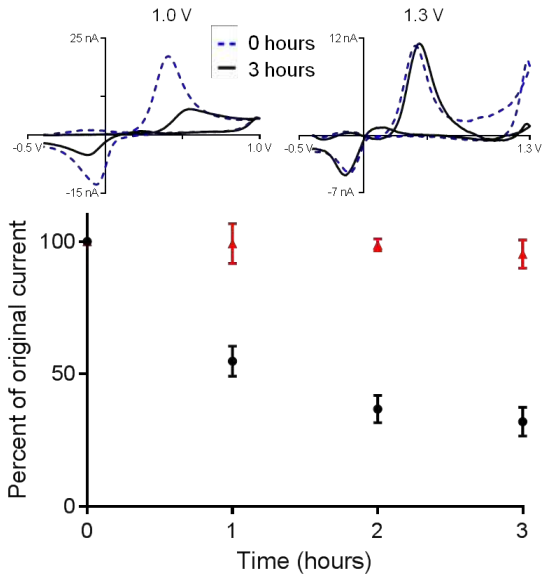

Figure 19. Stability of CNPEs over three hours at the 1.0 V waveform (black circles) and 1.3 V waveform (red triangles) (n=4 electrodes). Insets show example cyclic voltammograms for both waveforms at initial measurements and after three hours.

3.4.4 CNPE Characterization

Figure 20 shows that the CNPE peak oxidation current for 1 μM dopamine is proportional to the scan rate (R^2=0.984, n=4). The frequency was varied to keep equal time between scans. Current is normalized to the maximum value per electrode to minimize effects due to varying surface areas of different electrodes. For a diffusion-controlled process we anticipate a $v^{1/2}$ proportionality with peak current, arising from the diffusive time scale in the transport equation. For an adsorption-controlled process we expect a proportionality with scan rate, which arises upon the inclusion of adsorption kinetics via a Langmuir or linearized Langmuir isotherm (Bard & Faulkner, 2000). This plot indicates that the kinetics are more adsorption-controlled

than diffusion-controlled (plot of i vs $v^{1/2}$ yields an R^2=0.956, n=4), similar to carbon-fiber microelectrodes (Bath et al., 2000). Figure 20B shows peak currents for various dopamine concentrations (100 nM to 10 μM). Current is linear with concentration up to 10 μM. The average LOD, calculated from the 100 nM data, was 25 ± 5 nM (n=3).

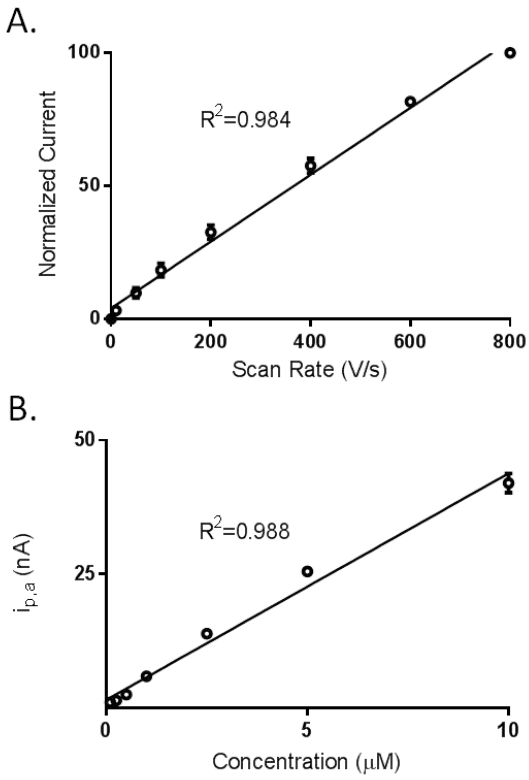

Figure 20. Electrochemcial characterization of CNPE. (A) Normalized peak oxidative current for 1 μM dopamine vs scan rate. The plot is linear for CNPEs (n=4) showing the kinetics are adsorption-controlled. (B) Peak oxidative current vs concentration (n=3). CNPEs show a linear response in current up to 10 μM. Solid lines are best fits of the data.

3.4.5 Measurements of Endogenous Dopamine in Drosophila Evoked by CsChrimson Stimulation

To test the use of CNPEs to detect endogenous dopamine in *Drosophila*, dopamine release was stimulated with the red light sensitive cation channel CsChrimson and detected using a CNPE. CsChrimson is a channel that is more red-shifted than the traditional Channelrhodopsin-2 which has been used in optogenetics (Klapoetke et al., 2014). Upon red light stimulation, the CsChrimson channels open and cations enter the cell, depolarizing the neuron and causing an action potential. A th-GAL4 driver was used to express UAS-CsChrimson in only the dopaminergic cells of the heterozygous crossed flies (Klapoetke et al., 2014). The CNPE does not penetrate cells but measures extracellular changes in dopamine that occur due to volume transmission.

CNPEs with lengths of 125-175 um would be suitable for measurements in mammalian tissues. However, because the *Drosophila* larval VNC is so small (only 200 μm in length), smaller CNPEs were needed. CNPEs with short exposed tips 8.2 ± 1.4 μm in length, were characterized and the average current for 1 μM DA at these electrodes is 0.39 ± 0.08 nA. However, the noise is also small and the S/N values are still good (37 ± 4). Figure 21 shows the cyclic voltammogram for dopamine (Figure 21A) when a short, 7 μm long CNPE (Figure 21B) was used to detect stimulated release. The cyclic voltammogram has the characteristic oxidation and reduction

peaks for dopamine. A false color plot of the data (Figure 21C) shows the dopamine release during a 5 second long red light stimulation. Consecutive voltammograms are plotted over time on the x-axis, the y-axis is applied voltage, and current is shown in false color. Green/purple is dopamine oxidation and blue/yellow is dopamine reduction. The concentration versus time plot is made using an *in vitro* calibration to convert maximum peak oxidation current to dopamine concentration. Dopamine is cleared from the extracellular space by dopamine transporters (Vickrey & Venton, 2011) and the concentration begins to decrease after the stimulation is finished. Using this short CNPE, endogenous dopamine was successfully detected, verifying that CNPEs are suitable for dopamine measurements in *Drosophila* tissue.

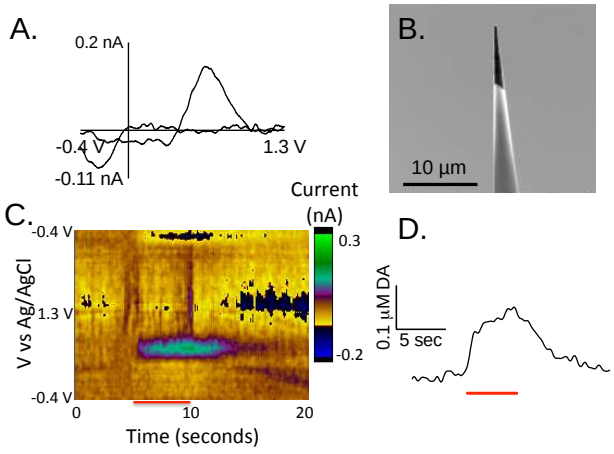

Figure 21. Example CNPE measurement of endogenous dopamine evoked by a 5 second continuous red light stimulation. (A) Background-subtracted cyclic voltammagram of evoked dopamine. (B) SEM of a short CNP like the one used *in vivo*. (C) Color plot showing stimulated dopamine in a *Drosophila* larval ventral nerve cord. Red light was applied from 5 to 10 seconds. (D) Extracellular concentration of dopamine over time as red light stimulates release (red line).

The batch fabrication of robust, nanosized electrodes suitable for *in vivo* studies is difficult and most methods to fabricate smaller electrodes have involved etching a single electrode by hand. The CNPEs developed here are batch fabricated and have the robustness to be implanted in tissue. The sensitivity per unit area for CNPEs with FSCV is slightly less than traditional CFMEs, but CNPEs are able to measure endogenous dopamine in *Drosophila* larvae. Reducing the length to 5 to 10 μm makes these CNPEs useful for high spatial resolution measurements in *Drosophila*. The Mirkin group has recently made disk electrodes from CNPEs with recessed tips for use as scanning electrochemical microscopy tips (Yu et al., 2014). Direct fabrication or mechanical polishing of CNPEs to disk electrodes that are flat and not recessed would allow future measurements from discrete regions and at single neuronal cells. The ability to measure endogenous dopamine release in *Drosophila* will allow for studies on how genetics or behavior affects neurotransmission regulation. CNPEs could also be applied to study other neurotransmitters such as serotonin and octopamine in the future.

3.5: Conclusions

We fabricated solid-tipped CNPEs that allow high spatial resolution measurements of dopamine. CNPEs are batch fabricated and the electrode geometry can be easily modified via puller parameters, deposition conditions, and etch duration, to produce electrodes of desired tip size, taper, and

exposed surface area. The nanoscopic tip provides for highly localized measurements, and its sharp conical shape makes it ideal for implantation into small regions such as the dopaminergic centers of the *Drosophila* brain. CNPEs were characterized for the first time with FSCV and their electrochemical signals for dopamine were suitable for *in vivo* measurements in *Drosophila*. CNPEs have fast electron transfer kinetics, stability, and good sensitivity. For dopamine, they are less sensitive per unit area compared to CFMEs, but still have sufficient signal for in vivo measurements. Interestingly, CNPEs showed improved sensitivity for serotonin compared to CFMEs. Coupled with FSCV, CNPEs could be used to measure real-time dopamine changes in specific regions of the adult fly, where the neuropil are only a few microns in diameter. Future studies in specific brain regions will give a better understanding of neurotransmission underlying discrete physiological processes. This work has been published in *Analytical Chemistry* (Rees et al., 2015).

Chapter 4: Carbon Nanopipette-Based Automated Injection System

4.1: Attribution

The work presented in this chapter was performed with Chengzhi Qi (MS candidate, University of Pennsylvania Dept. of Mechanical Engineering and Applied Mechanics) who worked under my direct mentoring. Chenzhi Qi coded, debugged, and tested the Matlab-based GUI that is presented in this chapter and contributed Figure 22. I served an advisory role by setting and guiding the project goals, training, troubleshooting, and performing live-cell experiments.

4.2: Background

Adherent cellular microinjection is a useful method for introducing precise volumes of liquids and controlled compositions of reagents into cells with single-cell resolution. There are few limitations on the types of solutions and suspensions that can be injected, so long as they can be loaded into a micropipette, do not clog the tip, and are not too viscous. Very few adjustments are needed between different cell lines or types so there is minimal time lost to parameter optimization, which is a common problem in electroporation, lipofection, and other bulk methods. It can take weeks or months of trial and error to yield parameters for good transfection efficiency via these bulk methods. Many bulk techniques are also wasteful in terms of

the amount of reagents used, as most of the reagents do not end in cells. These techniques also lack single-cell resolution and good compositional control, and they have poor cell viability with large percentages of cells dying in the process.

The unfortunate reality of microinjection however, is that it requires tedious manual manipulation of micropipettes by experienced operators and the throughput is inherently limited. It is also difficult to achieve good injection consistency among different experimentalists who may have subtle differences in technique and are susceptible to human error. An experienced operator can inject a few hundred cells per hour with a success rates that are wildly inconsistent, and are often as low as 35%. Improvements in microscopy and micromanipulation technology have greatly aided this field, but it is still limited by lack of robust automation. A number of groups have worked towards automated and semi-automated injection techniques (Adamo & Jensen, 2008; Ansorge & Pepperkok, 1988; Becattini, Mattos, & Caldwell, 2014; Esmaeilsabzali et al., 2012; Kallio et al., 2007; Pillarisetti et al., 2007; W. H. Wang et al., 2007; W. H. Wang et al., 2008; Zappe et al., 2006), but to my knowledge none have been successful in incorporating microinjection feedback with commercial microinjection and amplifier technology in a robust package for adherent mammalian cell injection.

In our previous work, we demonstrated the use of carbon nanopipettes (CNPs) for robust impedimetric feedback of microinjection. Briefly, a software

Lock-In amplifier is used to monitor the CNP's impedance and equivalent capacitance. There is a discrete change in measured capacitance upon cellular penetration and microinjection that can be used to provide electrical feedback. Carbon nanopipettes consist of a quartz micropipette with a thin layer of electrically-conductive pyrolytic carbon deposited along its interior *via* chemical vapor deposition (CVD) (Kim et al., 2005; Schrlau, Falls, et al., 2008; Singhal et al., 2010; Vitol et al., 2009). The quartz at the tip of the CNP can be etched in Hydrofluoric Acid to controllably expose the carbon tip, producing a batch-fabricated nanoelectrode of controllable geometry that can be hollow to permit fluid flow, or sealed for use as a pure nanoelectrode (Hu et al., 2013; Yu et al., 2014). CNPs are inexpensively batch fabricated, have tunable nanoscale geometry, and are compatible with common micropipette couplings and amplifiers, making them a versatile tool for cellular injection, biosensing, and electrochemical methods. To date, CNPs have been used for electrical feedback of cell probing and microinjection, fast scan cyclic voltammetry for neurotransmitter detection in *Drosophila*, scanning electrochemical microscopy (Hu et al., 2013), electrochemical nanosampling (Yu et al., 2014) injection of *C. Elegans* (Brennan et al., 2013), characterization of Calcium channels in breast cancer cells (Schrlau, Brailoiu, et al., 2008), and electrophysiological measurements (Schrlau et al., 2009).

Here we describe a Matlab-based graphical user interface (GUI) that interfaces an Eppendorf microinjection system, microscope CCD (charge-

coupled device) camera, and HEKA patch-clamp amplifier with our CNPs for semi-automated microinjection with electrical feedback. Matlab is a technical computing language that is commonly used in STEM fields, and is capable of interfacing with a wide range of systems. Eppendorf microinjection systems and HEKA patch-clamp amplifiers are commercially available and widely used in labs specializing in microinjection or patch-clamp electrophysiology. We anticipate that the availability and versatility of our code will allow other labs to implement their own semi-automated injection systems and facilitate novel microinjection studies by reducing difficulty and variability, while improving throughput and injection success rates.

The micromanipulation and amplifier control schemes could be adapted to alternative applications, such as semi-automated patch clamping, single-cell probing or electroporation, scanning electrochemical techniques, or other unforeseen technologies that would benefit from robust coupling between micromanipulator, microscope, and amplifier control in an adaptable scheme. For example, interfacing of the GUI with the pump controls leads the way for automation of single-cell dose-response studies, since pump parameters (pressures, injection times) can be incrementally adjusted in a controlled manner via the software to inject different groups of cells on the same dish with different volumes.

4.3: Experimental

4.3.1 Microinjection System and Computer Interface

A computer running Matlab version 2014b (MATHWORKS Inc.) was connected to the RS232 serial connection of an Eppendorf Femtojet microinjection pump and Eppendorf Transferman NK2 piezoelectric micromanipulator using USB-to-serial adaptors. The computer was also connected to a Hammamatsu ORCA ER CCD camera on an Olympus IX-71 inverted microscope via Firewire connection. A second computer was used to control the HEKA EPC 10-2 patch clamp amplifier via PATCHMASTER software (HEKA Elektronik Inc.). This secondary computer contained the data acquisition card for the amplifier, on a newer system it would be possible to integrate all functionality on a single computer. The computers were connected via a local area network. Raw data from the PATCHMASTER software was written to a network share folder where it could be read in real time with low latency (<1ms ping) by the Matlab computer.

Commands were sent to Eppendorf products via the serial connection following the syntax and settings in the user-manuals for the micromanipulator and pump (Eppendorf, Inc.). Camera control was achieved using the Matlab image acquisition toolbox and associated functions and controls. PATCHMASTER raw data files were read using 32-bit float format. The default settings for PATCHMASTER save data in a bundled file, which includes amplifier settings and associated meta-data. It is important to

disable this bundling in order to produce a single ".dat" raw file format that can be read by Matlab. The system overview is depicted in Figure 22.

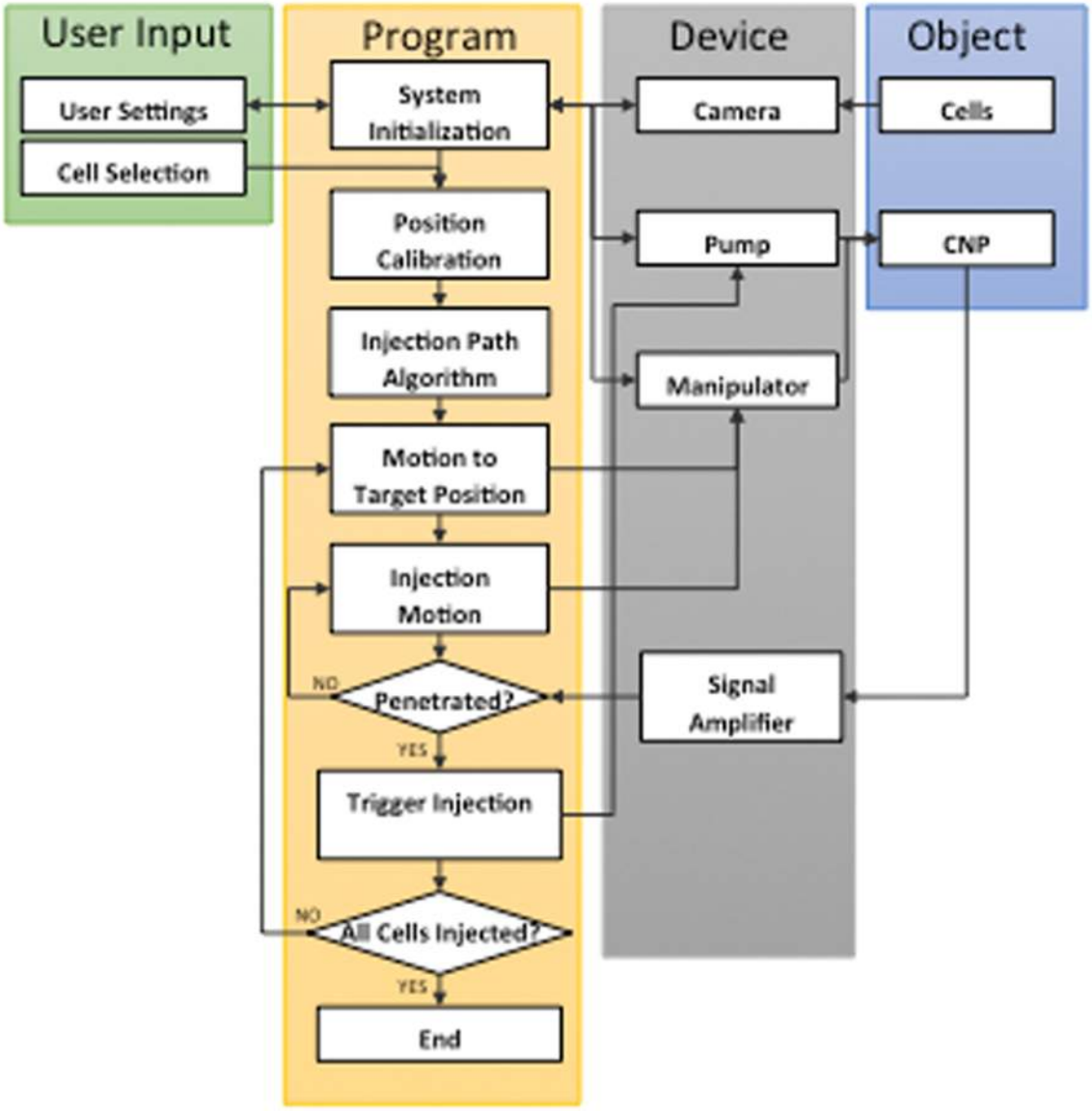

Figure 22. Semi-automated CNP injection system overview, depicting the interaction between the GUI, amplifier, microinjection equipment, and microscope imaging.

4.3.2 CNP Fabrication

Quartz micropipettes were fabricated as described in sections 2.2.2 and 3.3.2 from 1.0mm x 0.7mm filamented quartz capillaries of 10cm length (Sutter Inc.) using the following puller parameters: HEAT 750 FIL 4 VEL 50 DEL 150 PULL 85. Carbon deposition was performed for 1 hour at 900^{o} C, and CNPs were subsequently etched for 45-60s in 5:1 Buffer HF Improved (Transene Co.) to expose approximately 5-8 μm of the tip, measured along the cone axis. Pipette tip integrity was checked via optical microscopy prior to experiments. CNPs were loaded with 1mg/ml 4kDa FITC-Dextran (Sigma Aldrich) in 100mM KCl (Fisher Scientific) and imaged with fluorescence microscopy under moderate control pressure (1-5 kPa) to ensure that tips were open and dye was flowing well prior to microinjection. Clogged and broken CNPs were discarded.

4.3.3 Matlab Code

Our Matlab code is freely available online (Qi & Anderson, 2015). The main GUI structure is found in nk2gui2.m. Running this script will launch the GUI. It is important that all the other .m files (which contain algorithms for various processes such as path calculation, injection motion, and capacitance measurement) should be in the working directory. The computer used should contain drivers for the CCD camera and serial adaptors. The CCD camera should be selected such that it is compatible with Matlab's image acquisition toolbox, details of which can be found at their web page

("Image Aquisition Toolbox," 2015). Some settings may need to be adjusted based on hardware, such as COM ports for the serial adaptors. The code has been commented and broken into various functions for ease of editing, testing, and debugging. Currently the electrical detection scheme requires manual activation of the amplifier's LockIn software, after which point the user can select the active data file during injection.

4.3.4 Cell Culture

Adherent Mouse Embryonic Fibroblasts (MEF) were cultured in a 1:1 mixture of DMEM (HyClone Inc.) and F10 Nutrient Mix (Gibco Inc.), which was supplemented with 10% Fetal Bovine Serum (HyClone Inc.) and 1% Pennicillin/Streptomycin antibiotics (HyClone Inc.). Cells were cultured in a Fisher Isotemp CO2 incubator at 37^{o} C with 5% CO2 and were grown in 75mL cell culture flasks (Thermo Fisher), or 35mm glass bottom microwell dishes, Poly-d-lysine coated (MatTek Corp.). Experiments were performed at 70-90% confluency.

4.3.5 Microinjection Studies

35 mm culture dishes with 70-90% confluent MEF cells were placed on inverted scope and imaged with a 40x phase contrast objective on an Olympus IX71 inverted microscope. A CNP loaded with 5 μl of 4kDa FITC-Dextran (Sigma Aldrich) at a concentration of 1mg/ml in 100mM KCl (Fisher Scientific), was secured to the HEKA EPC 10-2 headstage using the HEKA 1.0mm pipette holder. The fluidic connection to the holder was connected to

the Eppendorf Femtojet microinjection pump. Several cells were manually injected to calibrate the pump parameters, which were typically a control pressure of 0.5-5 kPa, injection pressure of 5-15 kPa and injection time of 0.1-0.3 s. For electrical feedback, the capacitance signal was also verified during test injections to ensure that CNPs were responding as described in Chapter 2 and to adjust the threshold value.

A 2-point calibration routine was performed to ensure that the GUI camera window and the micromanipulator were properly coordinated. A z-reference plane was defined during test injections. For injection without feedback, the pipette will directly inject to that z-datum at the (x,y) coordinates specified, similarly to previously described methods (W. H. Wang et al., 2008).

After calibration, the user selects points on the live camera feed of adherent cells to serve as injection sites, and then hits enter. A traveling salesman algorithm then calculates an optimized pipette path that minimizes the total travel distance needed to move the pipette to inject cells at each selected (x,y) coordinate. The injection motion brings the pipette tip to the desired coordinates at a set speed and angle that can be adjusted within the GUI. For typical pipette orientation, this angle is between 30^{o} and 60^{o}. The pipette then dwells inside the cell while the pump is triggered, after which it is retracted, reversing the injection motion. This code has all been developed and optimized, however there is a significant drawback to this method of

injection due to the need to define a z-datum. Cells vary in thickness and substrates are rarely perfectly planar relative to the manipulator. Experimentally, we find that a substrate can vary by over a micron in the z-coordinate within a field of view (~20 cells). Lack of frequent z-calibration can result in substrate contact or completely missing the target cell. Because of this, we anticipate that incorporation of electrical feedback would significantly improve injection throughput and success rate, which at the moment is dependent on careful and frequent calibration. This injection mode was tested for proof-of-concept.

For electrical feedback, the PATCHMASTER software's LockIn module is run continuously with the equivalent capacitance component (CM) output exported to a raw data file. This data is then read into Matlab. The extracellular capacitance value is stored for reference, and a threshold is defined based on our previous characterization. This threshold is a percentage drop in the capacitance (relative to the extracellular value) that indicates cellular penetration. The threshold can be easily adjusted based on variations in experimental conditions such as buffer, cell line, or injection fluid. It would also be possible to output impedance, and define an impedance threshold based on the Real or Imaginary components, or simply the impedance magnitude. For 100mM KCl solution, we attain a capacitance signal change of ~10% on average during injection, consistent with our

previous experience, and so a threshold of 1-5% should be sufficient for penetration detection.

Injection is performed in the same manner as previously described, except that the pipette is triggered to stop and initiate injection when the capacitance or impedance threshold is reached. If a z-reference is defined we can use the same injection motion previously defined, if not we can prescribe a purely downward motion of the pipette to ensure that the target (x,y) coordinates are injected. Unfortunately, the "Stop" command for the Eppendorf manipulator does not function, and so currently the routine is programmed to traverse downwards with a prescribed step size, and the capacitance is measured at each step before the next step is triggered. This slows detection and throughput considerably. We anticipate that incorporation of a functional stop command would allow us to use faster injection speeds and detect penetration earlier, which should improve accuracy and throughput. After injection the pipette is retracted. Large deviations in the extracellular capacitance after retraction indicate clogging or CNP breakage, at which point CNPs can be replaced or cleaned. This process is depicted in Figure 23. This process has similarly been tested for proof of concept.

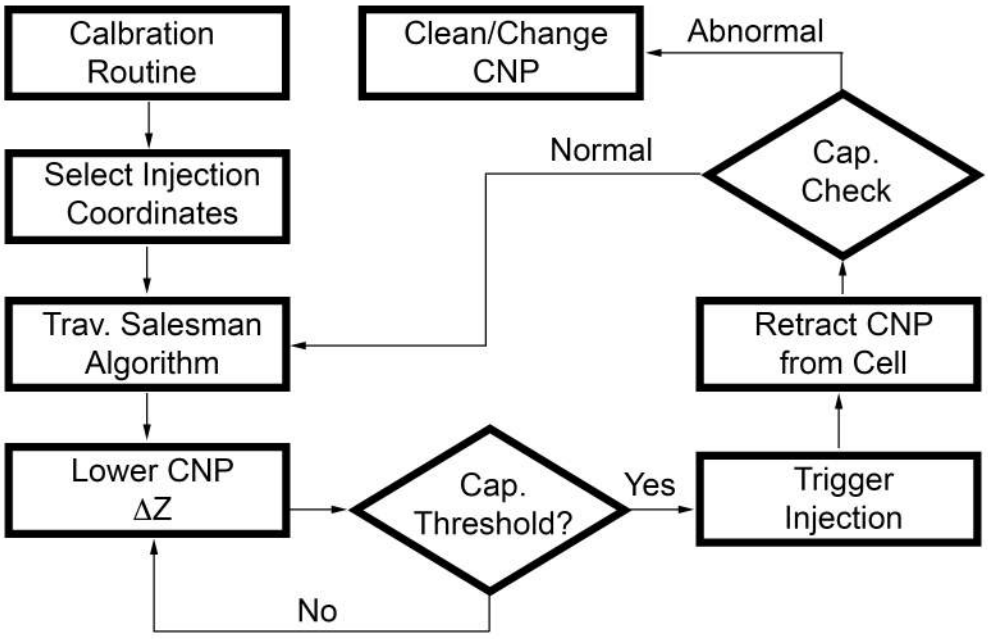

Figure 23. Microinjection logic flow chart. "Cap." is an abbreviation for capacitance, and "Trav." is an abbreviation for traveling. Abnormal and Normal refer to the capacitance relative to the reference extracellular state. A large deviation from this reference state is indicative of pipette breakage or clogging.

4.3: Results and Discussion

4.4.1 Matlab Graphical User Interface

The Matlab-based GUI is depicted in Figure 24. The various controllers are denoted in the figure with colored outlines. The camera controls are located on the top of the GUI (Figure 24A), allowing the user to start and stop live image acquisition, adjust gain, contrast, and exposure, and save photos or videos. The live camera feed is shown in Figure 24B. The feed depicts a typical cell injection field of view with 40X phase contrast objective. Adherent MEF cells are shown and the shadow of our CNP is visible and

entering the field of view from the right hand side about 1/3 of the way up from the lower edge of the frame. Figure 24C shows the injection settings. Here, the user sets a Z-datum, and can adjust injection parameters such as speed, angle, and pull-back delay, which should be coordinated with the injection time. Figure 24D is where pump parameters can be easily adjusted, including the compensation pressure, injection time, and injection pressure. There is also an option to run the clean function on the pipette, which applies a maximum burst of pressure for a user-defined amount of time. This is helpful for dislodging clogs from the pipette. An automatic clean routine is also built into the code. This routine triggers the clean function after a user-defined number of cell injections to reduce clogging propensity. Lastly, Figure 24E has an information display board which returns feedback from the pump and manipulator queries, and a button for adjustment of additional settings. These settings include COM ports for the manipulator and pump, and remote/manual toggle for the manipulator control.

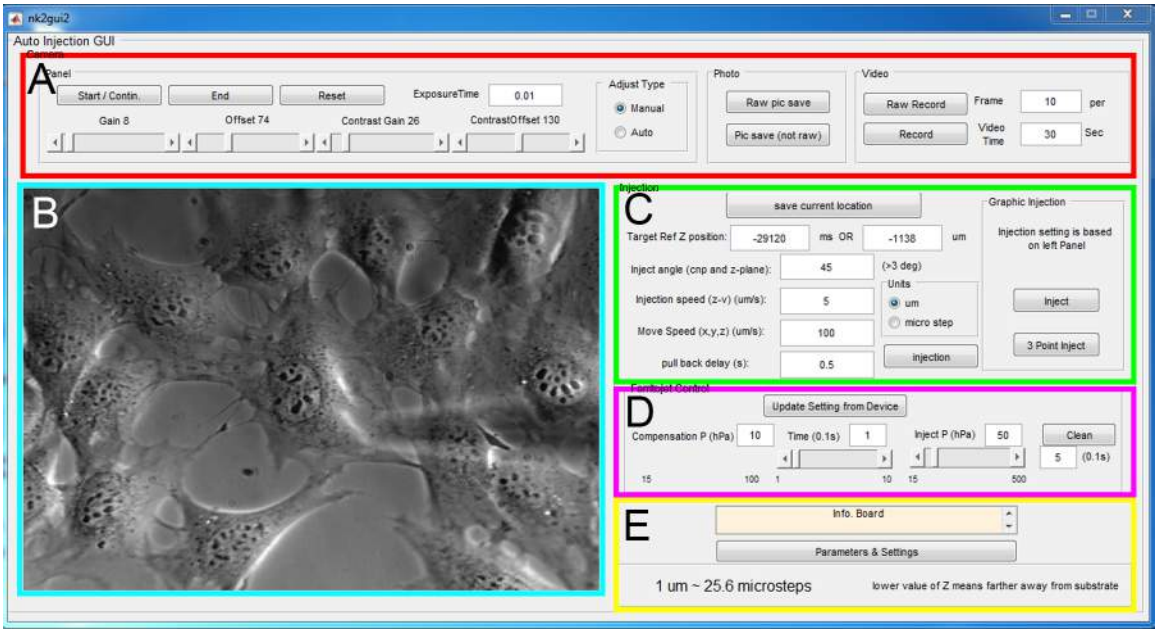

Figure 24. Matlab-based semi-automated GUI. Various sections are outlined in color for emphasis. (A) Camera controls for gain, contrast, and image/video acquisition. (B) Live camera window with cells and CNP visible. (C) Injection parameters (substrate datum, speed, angle, pull-back delay). (D) Pump parameters for control pressure, injection pressure, injection time, and clean function. (E) Information display board and additional connection parameters (COM ports etc…).

When a user is interested in performing microinjection, the "inject" button in the Graphic Injection subsection of Figure 24C is selected to launch a sub-GUI for graphic injection which is depicted in Figure 25A.

4.4.2. Calibration

It is important to perform a simple calibration to ensure that the micromanipulator and GUI camera feed are properly synchronized. We utilize a simple two-point X/Y calibration which is depicted in Figure 25B and

C. Briefly, the microscope is focused onto the CNP's tip a few microns above the cells of interest (Figure 25B). The user is instructed to move the pipette tip to the top right region of the window (Figure 25B), at which point a crosshair is used to select the tip coordinates. Next the user is prompted to move the pipette to the lower left region of the window and again selects the pipette tip (Figure 25C). This provides two (x,y) coordinates for both the GUI window and the manipulator. The two coordinates provide us with a vector in each reference frame, directed from one point towards the other. The length of the vectors (distance between coordinates) provides a scale factor between the two reference frames. Using a simple equation system, we can also find the components of a 2-dimensional rotation matrix to solve for any angular difference between the manipulator and GUI reference frames. This allows us to compensate for any angular misalignment. Lastly we define one of the calibration points as a fixed origin point between the two frames. Any point the user selects in the GUI will define a point relative to the origin, from which a vector can be drawn. This vector can then be scaled and rotated into the manipulator reference frame, and the resulting coordinates can be rounded to the nearest step or micron and sent to the manipulator. To test the calibration scheme we measured the distance between the pipette tip and target coordinates using the known pixel size of our CCD camera. We found the tolerances in the (x,y) coordinates to be within 1 micron for a well-

calibrated pipette, which is sufficient resolution for nuclear or cytoplasmic targeting of mammalian cells.

If CNPs are not being utilized for electrical feedback, then the user can choose a traditional z-datum injection. In this mode, the z-reference plane is stored using the "save current location" button in Figure 24C, typically by performing a manual test injection. The pipette is directed into position at the user-selected injection coordinates on the GUI, which we will denote as (x_i,y_i). The pipette is then driven to inject the target cell at (x_i,y_i,z_{ref}) with z_{ref} the reference z datum. With the exact injection coordinates known, an optimized injection motion can be utilized, similar to that used by newer Eppendorf microinjection systems (Eppendorf InjectMan) and programmed by other groups (Becattini et al., 2014). Briefly, the pipette is driven to the target coordinates at a specified angle, typically selected to align with the pipette axis such that the motion penetrates the cell normal to the cellular membrane. The pipette is retracted at this same angle. This motion ensures that the cell is penetrated using the sharpest possible entry angle, which minimizes damage to the cellular membrane and helps reduce the interaction of the pipette with the cell and its membrane, which can clog or foul pipettes with biomaterial.

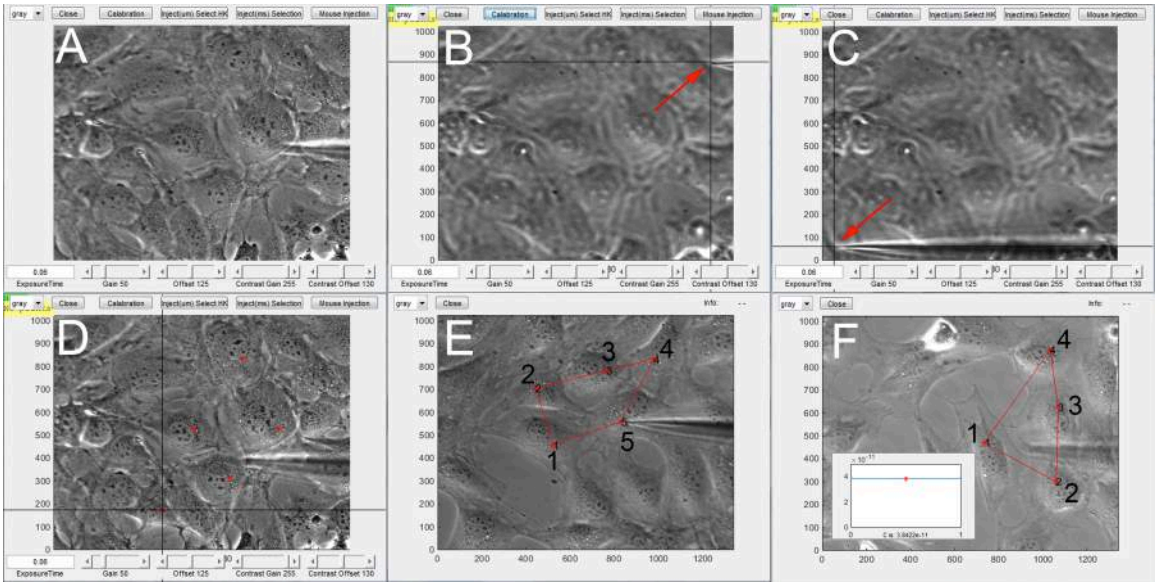

Figure 25. GUI calibration and injection routine. (A) Sub-GUI for Injection. (B) X/Y calibration step 1: the pipette is moved to the upper right of the field of view and the user identifies the location of the pipette tip. (C) X/Y calibration step 2, the pipette is moved to the lower left of the field of view and the user selects the tip via crosshair. Red arrows in (B) and (C) indicate crosshair and tip location. (D) After calibration the user selects the injection points via mouse crosshair. Injection points are tagged with a red star. (E) Z-datum injection with optimized injection path shown. Numbers have been reproduced and enlarged for visibility. (F) Microinjection with electrical feedback. Cell numbers have been reproduced and enlarged for visibility. Inset displays the capacitance measurement (red star) as well as the extracellular capacitance threshold (blue line). When the capacitance drops below a percentage threshold below the blue line, injection will be triggered.

It is also possible to perform a 3-point calibration routine using the "3 point inject" button on Figure 24C. In this calibration, the pipette is used to lightly contact the substrate at three points. These three points can be used

to mathematically define the plane of the substrate relative to the manipulator and subsequent injection will target the plane at the specified (x_i,y_i) coordinates. This is more accurate than the z-datum calibration, but requires multiple points of substrate contact and must still be recalibrated with some frequency. This means there is a tradeoff between accuracy and time, with additional risk of pipette damage.

4.4.3. Semi-Automated Cellular Microinjection with Electrical Feedback

The semi-automated injection process is shown in the sub-GUI for Figure 25D through F. Figure 25D shows the cell selection process. The user can select an arbitrary number of points on the live camera feed, selecting desired cells for microinjection, as well as targeting the cytoplasm, nucleus, or specific sub-cellular regions. The selection process is performed using the mouse to move the crosshair to the desired location and then left-clicking. A red star indicates the selected location as a visual cue to help the user keep track of which cells are being injected. When the user has selected all the cells of interest, he/she can press 'enter' or right-click to start the path optimization and injection procedure. The path optimization uses a traveling-salesman algorithm, similarly to Wang et al. (W. H. Wang et al., 2008), to find the shortest path between the selected points. This path is then plotted over the GUI and the injection procedure is started, following the injection path between points. The selection of injection points can be automated with the use of imaging software.

Figure 25E shows traditional z-datum injection, with the injection path depicted in red, the injection points indicated by the red stars, and the order of injection denoted by the small number next to each star. In the figure, the CNP penetrates the last cell, #5. At the conclusion of the injection process, the pipette will return to its initial position, and the software will notify the user that the injection has been completed with a small popup window. There is also a "mouse injection" mode in which left clicking the live camera feed moves the pipette to that location, and right clicking triggers injection at that location. This injection mode allows a user to inject cells one-by-one in rapid succession with real-time control, which we anticipate to be a highly desirable feature. Traditional z-datum injection is fast and efficient, but requires frequent recalibration and has poor success rates. This is because within the field-of-view of our microscope the substrate z-datum can vary by 1-2 microns relative to our manipulator. This is significant since adherent cells are only 3-5 microns at their thickest point (W. H. Wang et al., 2008), and are thinner farther from the nucleus. This means that a 1-2 micron shift in cellular z-location can result in cells not being penetrated by the micropipette, or being penetrated too deeply. The latter can result in substrate contact, increased propensity for pipette breakage and clogging, and likely cell death. In either case injection will be unsuccessful. This results in poor success rates for z-datum injection, and a need for frequent recalibration whenever injecting cells far from the calibration point.

Figure 25F depicts microinjection with our CNP electrical feedback. In this mode, the user defines a capacitance threshold that can be adjusted based on the injection solution of interest as described in Chapter 2. The point selection and path optimization is identical to the previous injection mode, except now we have electrical feedback. The user has the option of not performing z-calibration and the pipette will traverse straight downwards at the target (x_i,y_i) location. Alternatively, the user can use a z-calibration with the optimized injection motion and the benefits of electrical feedback. With this feedback, the under- or over-estimation of the target z-coordinate for injection can be avoided, since the pipette will translate towards the cell until penetration is detected and injection is triggered, or until the z-limit is reached. The z-reference can be used to define this z-limit, as well as a start point for the injection motion. By beginning the injection at a point close to the cells, the time resolution can be improved be decreasing the average distance the pipette needs to travel to contact the cell. The extracellular capacitance is measured prior to the injection motion as an average over 10ms (10 data points) and set as the baseline value. When the signal drops below the threshold as the pipette is lowered, the motion is halted and injection is triggered. After injection, the pipette is retracted and moves to the next cell. The capacitance is plotted in real time as shown in the inset in Figure 25F. The blue line is the baseline value, and the red dot is the most recent capacitance measurement. In this panel, the pipette is in the

extracellular solution and so the measurement and baseline are aligned. When the threshold is reached, the capacitance display panel will flag with a red cross as a signal to the user.

A successful proof-of-concept injection with electrical feedback is depicted in Figure 26. Figure 26A shows three cells selected for injection. Figure 26B shows the optimized injection path overlaid on the cells, and the capacitance display window in the lower right of the panel. Figure 26C(i) depicts the capacitance trace during the successful microinjection of the three cells pictured. In each case, the cell injection was triggered by the capacitance signal, which dropped on the order of 3-5 pF when the tip penetrated the cell. The three points of cell penetration are denoted by arrows with numbers corresponding to the cells in Figure 26A and B. The inset in Figure 26C(ii) is a fluorescence micrograph of the three cells post-injection. It was clear that each cell was injected based on visible swelling, but in cases where the injection volume is small, fluorescence is a useful tool for confirmation of successful injection. There is some periodic (1s interval) noise below the capacitance curve, which is an artifact of the sweep settings in the PATCHMASTER software. When the data file is written by PATCHMASTER there is an appended data segment at the end of the file that we found to be proportional to the sweep length, and longer sweeps result in file read delays as could be expected. Thus it is advantageous to run multiple shorter sweeps rather than one long continuous sweep, in the interest of time resolution.

Optimization of the sweep parameters and some filtering algorithms can be implemented to mitigate this noise in the future.

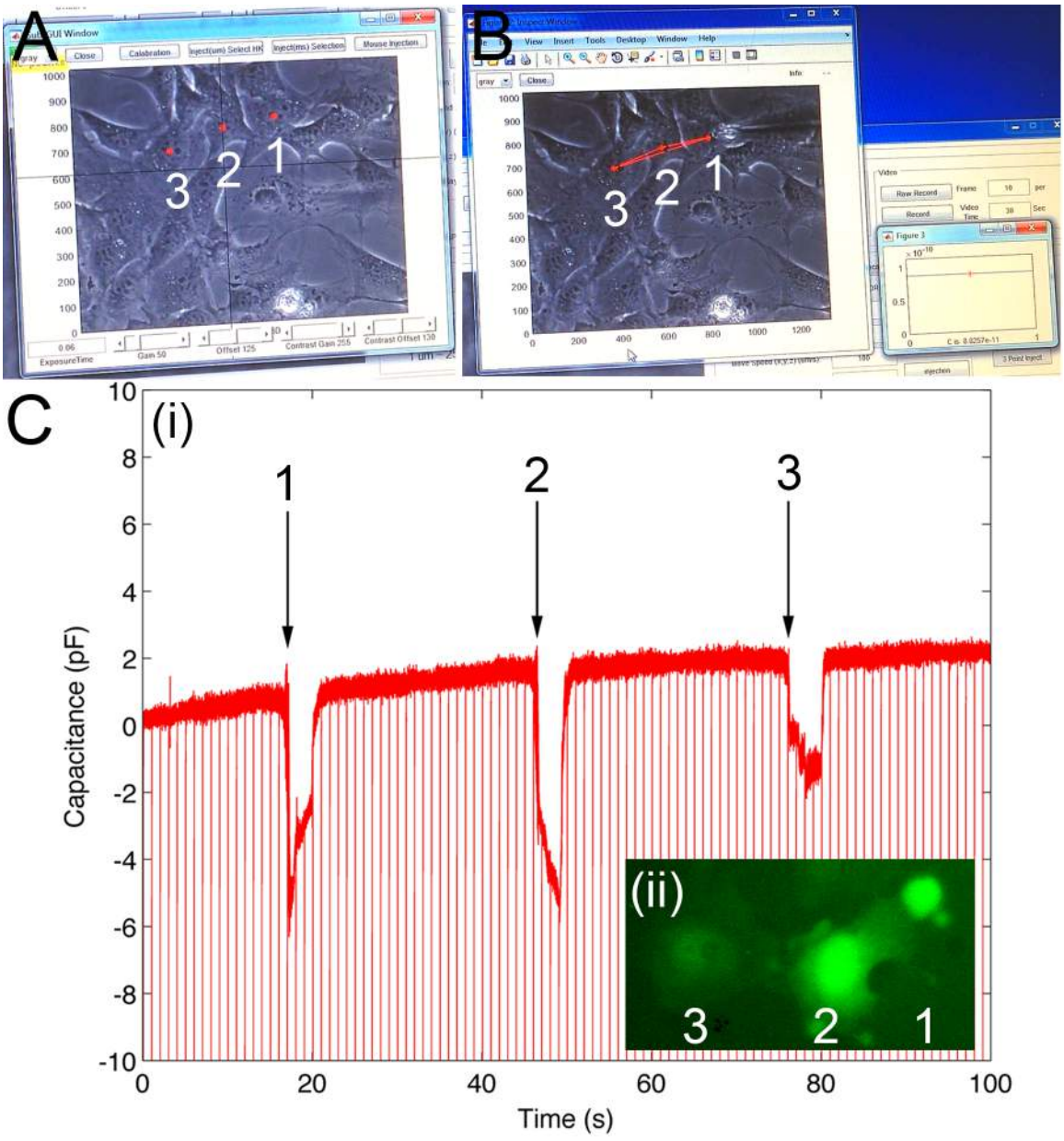

Figure 26. Semi-automated cell injection with electrical feedback. (A) Injection coordinates selected for the three numbered cells. (B) The injection path during the automated microinjection is shown with a red line. The capacitance is monitored in the display window in the lower right of the panel. (C)(i) Capacitance trace as a function of time during automated microinjection. A clear capacitance

drop is seen for each of the three cells. Arrows indicate the point of penetration for each of the three cells (numbered). (ii) Inset shows three cells fluorescing after successful injection with FITC-dextran.

This injection was performed using the axial injection motion in conjunction with the capacitance feedback mode. This requires the additional step of defining a z-limit to prevent substrate collision and to bound the process since the system needs an estimate for the z-coordinate to define the angled trajectory. This has advantages in terms of invasiveness or minimization of clogging/fouling as described previously due to the pipette penetrating the cell at a sharper angle. This is the most robust injection mode because it allows the use of the axial injection-motion with electrical feedback, and can also serve as a worst-case safeguard against substrate contact with the pipette.

4.4: Conclusions

We have successfully developed a semi-automated adherent cell microinjection system using carbon nanopipettes for impedimetric feedback. We used commercial equipment and a custom GUI designed in Matlab. The GUI source code is easily editable and can take advantage of the myriad functionalities available in the Matlab software for more advanced control capabilities. While it is unlikely that manipulator-based microinjection will ever be truly *high*-throughput, advancements such as these can help researchers attain statistically significant cell numbers with single-cell

precision, and improved consistency among different operators and laboratories. This opens the door for novel studies that are not feasible with alternative transfection methodologies. The use of commercial equipment will allow for this system to be readily adopted by labs with similar equipment, or labs interested in entering the microinjection field, and can be adapted to new applications due to the versatility of Matlab.

Our software has been tested for proof of concept. We have been successful in performing semi-automated microinjection without electrical feedback, and have overcome obstacles to incorporate electrical feedback through the development of a scheme to read the raw binary data files written by our patch-clamp amplifier in real time. We have tested this code, verifying that we are indeed monitoring the capacitance signal in real time, and we have implemented this detection methodology for microinjection with our CNPs, leading to successful proof-of-concept semi-automated injection of adherent cells with electrical feedback (Figure 26). What remains for further development of the code is optimization of the impedimetric detection scheme, streamlining the user interface, and quantifying the performance of the GUI using some clearly defined metrics, for example injection success rate (number of cells injected versus number attempted) and throughput in terms of cells injected per hour. Additional functionality may be built into the code to improve robustness, such as using the time derivative of the capacitance data to help avoid drift issues, and incorporating automated

pipette quality-control measures to monitor the status of the pipette in the extracellular solution. Large deviations in the extracellular impedance or capacitance can be indicative of clogging or fouling and can be used for further feedback on the state of the pipette.

Below are several recommendations for improved implementation of this system with electrical feedback:

1. Moving amplifier control and data acquisition to the same computer. The current data acquisition computer is limited in terms of memory, processing speed, and storage. In addition, PATCHMASTER is capable of being controlled by external software, meaning Matlab could be programmed to control amplifier acquisition. Data management would also be easier, obviating the network share folder and improved memory and processing speed could help with time resolution.
2. Implementation of a manipulator "Stop" function. The current process loop involves moving the manipulator one step and then checking the capacitance. Ideally, the manipulator would simply traverse downwards at a constant speed and halt motion when the capacitance threshold is reached.
3. Using a new manipulator and pump. The new line of Eppendorf equipment has a smaller step size that will improve precision, likely

has improved noise characteristics, and will have more reliable computer control schemes and better technical support.

4. Extensive testing and iteration to optimize code and experimental parameters.

Chapter 5: Microinjection of fl-tRNA for Studies of tRNA Subcellular Dynamics

5.1: Background

tRNA is a fundamental adaptor molecule in cells, providing the necessary link between mRNA codon sequence and amino acids during protein synthesis at a ribosome (Alberts et al., 2013). It serves a major role in cellular translational machinery. Defects and dysregulation of tRNA are linked to a number of diseases and disorders (Pavon-Eternod et al., 2009; Tuller, 2012).

Researchers are discovering that tRNA has a greater role in cell biology than previously recognized. There are on the order of 500 genes encoding tRNA, which is a surprising diversity, considering that there are only 22 standard amino acids, even when isoacceptors are accounted for. The tRNA is encoded in both the cell nucleus and mitochondria, and there are cellular mechanisms that cause some nuclear-encoded tRNA to be imported into the mitochondria for protein synthesis (Rubio & Hopper, 2011). tRNA has also been found to bind with Cytochrome C (CytC) (Hou & Yang, 2013; Mei, Stonestrom, Hou, & Yang, 2010; Mei, Yong, Liu, et al., 2010; Mei, Yong, Stonestrom, & Yang, 2010) which could have implications for the Warburg effect (Michelakis, Webster, & Mackey, 2008; Zhao, Butler, & Tan, 2013). Cancer cells are known to have elevated levels of tRNA (Pavon-Eternod et al.,

2009), and tRNA-inhibition of CytC in the mitochondria could be related to cancer cells shifting to anaerobic respiration pathways. Elevated tRNA levels have already been linked to apoptotic resistance (Hou & Yang, 2013; Mei, Stonestrom, et al., 2010; Mei, Yong, Liu, et al., 2010; Mei, Yong, Stonestrom, et al., 2010), and the metabolic pathway has been shown to be a viable therapeutic target for cancer cells (Michelakis et al., 2008; Zhao et al., 2013). tRNA nuclear/cytoplasmic trafficking is also an interesting phenomenon. tRNA is made in the nucleus and then exported to the cytoplasm, where the translational machinery of the cell is located. It has been shown however, that tRNA can also travel retrograde, from cytoplasm into the nucleus, and there are certain modifications to the tRNA that occur only after it has been reimported into the nucleus (Hopper, 2013; Hopper & Shaheen, 2008; Kramer & Hopper, 2013; Murthi et al., 2010). tRNA retrograde nuclear transport has been shown to be a critical step in HIV infection, facilitating the transport of the HIV reverse transcription complex into the nucleus where it incorporates the viral genome into the host cell. The HIV-linked tRNA accumulates in the nucleus on its own, and has a defective 3' end, which makes it incapable of supporting translation. This suggests that cells may have regulatory machinery to return damaged tRNA to the nucleus for repair or degradation (Zaitseva, Myers, & Fassati, 2006), and that tRNA nuclear import is robust enough for viruses to have evolved to exploit it. Understanding the tRNA nuclear/cytoplasmic trafficking mechanisms and the factors involved can

provide insights into how cells regulate tRNA subcellular distribution, what factors affect trafficking, how tRNA trafficking differs between healthy and diseased/cancerous cells, and how viruses like HIV are able to take advantage of tRNA trafficking mechanisms to enter the nucleus of cells. It is also of interest to see how tRNA modifications, different tRNA isoacceptors, or tRNA damage affect trafficking.

One of the difficulties in tRNA trafficking studies is that they typically use fluorescence in-situ hybridization (FISH), which is a fixation technique that is cumbersome to perform and only provides snapshots of the tRNA dynamics (Hopper, 2013). The Cooperman Lab at Penn has developed chemistry for fluorescently labeling tRNA (fl-tRNA) with various fluorophores (Betteridge et al., 2007). The fluorescently tagged tRNA behaves similarly to native tRNA in terms of protein synthesis, and allows for real time dynamic monitoring of tRNA subcellular dynamics, including monitoring of protein synthesis in real time (Barhoom et al., 2011) and monitoring viral protein upregulation after infection (Barhoom et al., 2013). Fl-tRNA can also be used to study subcellular nuclear trafficking dynamics in real time. Typically lipofection is used to introduce fl-tRNA into cells, but lipofection requires an incubation period that may result in a loss of information on early-time dynamics. Microinjection provides an elegant alternative, due to its single cell resolution, ability to inject selectively into either the cytoplasm or nucleus, and capabilities for simple dose control via

injection parameters. Most importantly, microinjection provides a known start time for observations of dynamics and extraction of transport kinetics.

5.2: Experimental

5.2.1 Injection Method

Filamented quartz micropipettes (Sutter Instruments) were back-loaded with fl-tRNA suspended in molecular grade water, connected to an Eppendorf Femtojet microinjection system, and mounted on an Eppendorf Transferman NK2 piezoelectric micromanipulator on an Olympus IX71 inverted microscope. Fl-tRNA was provided by the Cooperman lab and was prepared as previously described (Betteridge et al., 2007). Mouse Embryonic Fibroblast (MEF) cells were cultured in 44.5% DMEM (HyClone), 44.5% F10 nutrient mix, 10% fetal bovine serum (HyClone), and 1% Pennicilin/Streptomycin antibiotics on glass-bottom cell culture dishes treated with Poly-L-Lysine (MatTek Corp.) and kept in a Fisher Isotemp incubator at 37C and 5% CO2. Some experiments were carried out with HeLa or U2OS cells as well, under identical conditions, except no F10 was used (89%DMEM). Two hours prior to experiments, the cell media was replenished. Cells were microinjected with tRNA (typically 10-100μM for a final cellular concentration of 1-10μM) via continuous flow injection and observed either with epifluorescence or spinning disc confocal microscopy. For nutrient deprivation, cell media was changed to low glucose DMEM w/o amino acids immediately after microinjection unless otherwise specified. On

the spinning-disc confocal microscope, cell cultures were maintained in a stage incubator (LCI Chamlide) that controlled temperature (37C) and CO2 levels (5%). The spinning disc confocal experimental setup is depicted in Figure 27. For standard epifluorescence, cells were maintained in ambient conditions, at room temperature and standard atmosphere.

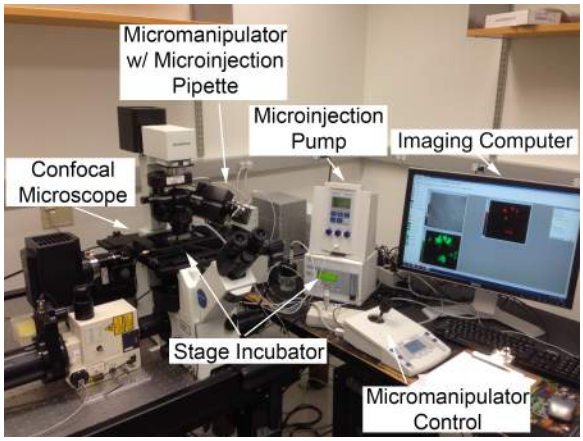

Figure 27. Spinning disc confocal microscopy with stage incubation and microinjection capabilities.

5.3: Results and Discussion

5.3.1 Simple Kinetic Model for Membrane Transport

Here we describe a simple kinetic model for nuclear/cytoplasmic trafficking kinetics.

Assumptions:

1) The kinetics of membrane transport are concentration dependent and of the form:

$$J = kC$$

Equation 20.

In the above, J is the mass flux across the membrane, k is the rate constant, and C is the concentration.

2) Diffusion throughout the cytoplasm and nucleus occur at a time scale significantly faster than the transport across the membrane. Concentrations can change over time, but are uniform in the cytoplasm and nucleus. Please see section 5.3.3 for further discussion on the validity of this assumption.

3) Injection is only into the cytoplasm so the nuclear concentration is zero initially.

Governing equations:

1) Mass transport

$$\frac{dC_N}{dt} + k_{out}C_N = k_{in}C_C$$

Equation 21

2) Mass conservation

$$C_N V_N + C_C V_C = C_0(V_N + V_C)$$

Equation 22

Variable definitions:

C_N = Nuclear concentration of tRNA

V_N = Volume of the nucleus

C_C = Cytoplasmic concentration of tRNA

V_C = Volume of cytoplasm (total cell volume – nuclear volume)

C_0 = Mean concentration of tRNA or the concentration of the tRNA when it is evenly distributed within the entire cell

k_{out} = rate constant of tRNA nuclear export

k_{in} = rate constant of tRNA nuclear import

t = time

Eliminating C_N from Equation 21, using Equation 22:

$$C_C = \frac{C_0(V_N + V_C) - C_N V_N}{V_C}$$

Equation 23

We define a volume fraction:

$$\varphi = \frac{V_N}{V_C}$$

Equation 24

Equation 23 assumes the form:

$$C_C = C_0(\varphi + 1) - C_N\varphi$$

Equation 25

Substituting Equation 25 into Equation 21:

$$\frac{dC_N}{dt} + (k_{out} + k_{in}\varphi)C_N = k_{in}C_0(\varphi + 1)$$

Equation 26

Equation 26 has the solution

$$C_N(t) = \frac{k_{in}C_0(\varphi + 1)}{(k_{out} + k_{in}\varphi)} + Ae^{-(k_{out}+k_{in}\varphi)t}$$

Equation 27

Using the initial condition $C_N(0) = 0$:

$$\frac{C_N(t)}{C_0(\varphi + 1)} = \frac{k_{in}}{(k_{out} + k_{in}\varphi)}\left(1 - e^{-(k_{out}+k_{in}\varphi)t}\right)$$

Equation 28

Using Equation 25 to solve for $C_C(t)$

$$\frac{C_C(t)}{C_0(\varphi+1)} = 1 - \frac{k_{in}\varphi}{(k_{out}+k_{in}\varphi)}\left(1 - e^{-(k_{out}+k_{in}\varphi)t}\right)$$

Equation 29

Taking the ratio of the nuclear and cytoplasm concentrations:

$$\frac{C_N(t)}{C_C(t)} = \frac{\left(1 - e^{-(k_{out}+k_{in}\varphi)t}\right)}{\left({}^{k_{out}}/_{k_{in}} + \varphi e^{-(k_{out}+k_{in}\varphi)t}\right)}$$

Equation 30

Long time behavior (t→infinity):

$$\frac{C_N(t)}{C_C(t)} = {}^{k_{in}}/_{k_{out}}$$

Equation 31

Equation 31 is self-consistent with Equation 21 when $dC_N/dt=0$.

Fluorescence intensity is proportional to concentration for dilute fluorophores. Typical cellular microinjection is on the order of 10% of the cellular volume, leading to intracellular concentrations on the order of a few micromolar, well within this dilute linear regime. The ratio of nuclear to cytoplasmic mean intensity should follow Equation 30. This data can be extracted from our experiments with image processing, and fit to our model using Mathematica to extract kinetic parameters.

5.3.2 tRNA Dye Effects

One major concern of using fluorescently tagged tRNA is that the fluorescent label will alter the normal tRNA trafficking behavior, or that free dye in the solution can obscure the true tRNA dynamics. For example,

different fluorophores will interact differently with lipid membranes (Hughes, Rawle, & Boxer, 2014). This issue arose when I attempted to study two arginine isoacceptor tRNA within the same cell. One isoacceptor was labeled with Cy3, and the other with Rhodamine 110. The two tRNA had different cellular distributions, and a control test with bulk tRNA showed that this was primarily a dye effect. Additional tests with Alexa 488 and Alexa 555 - labeled phenylalanine isoacceptor tRNA showed that these dyes also had differences in their distribution. There are also differences relative to control cells injected with dye only. These results are depicted in Figure 28.

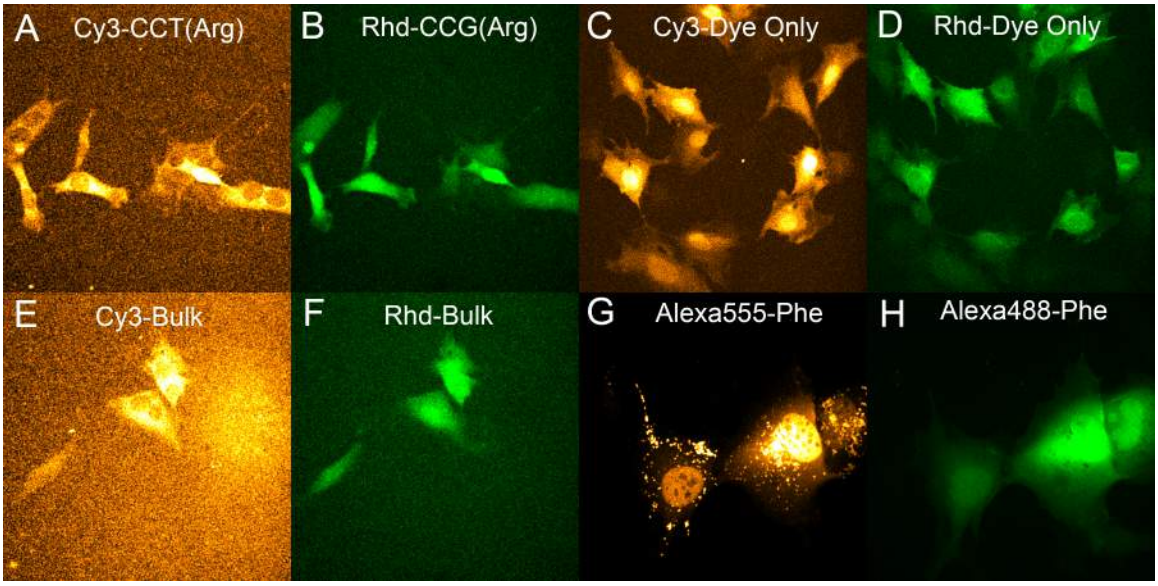

Figure 28. tRNA dye effects. (A) MEF cells coinjected with 25μM CCT Cy3 tRNA and (B) 25μM CCG Rhodamine tRNA. Both CCT and CCG are Arginine isoacceptors. (C) MEF cells coinjected with 25μM Cy3 dye (no tRNA) and (D) 25μM Rhodamine 110 dye (no tRNA). (E) MEF cells coinjected with 12.5 μM Cy3 bulk tRNA and (F) 12.5 μM Rhodamine bulk tRNA. (G) MEF cells coinjected with 25μM Phenylalanine Alexa 555 tRNA and (H) 25μM Phenylalanine Alexa 488 tRNA.

In all cases in Figure 28, the tRNA with green dye (Rhodamine or Alexa 488) distributes fairly evenly throughout the cells. The Cy3-tRNA distributes preferentially throughout the cytoplasm with a decreased concentration in the nucleus, and the Alexa 555-tRNA can be seen in the nucleus and forming discrete bright spots in the cytoplasm that have interesting transport behavior on the timescale of the experiment. It is possible that these are polyribosome complexes or tRNA aggregates and that there is some controlled transport behavior on cytoskeletal transport networks such as microtubules. When dye alone (no tRNA) was injected (Figure 28C and D), we saw the Cy3 distribute throughout the cell with some concentration in the nucleus, and the Rhodamine distributed throughout the cell but somewhat less in the nucleus. Imaging cells with dye alone was not stable, and the dye disappeared from the cells rapidly (3 minutes for rhodamine, 10 minutes for Cy3). We can rule out photobleaching because two cells remained fluorescent significantly longer than the rest (22 minutes for the Cy3 channel), in addition to successful long term (>2 hour) imaging with fl-tRNA using the same labels. Both Cy3 (Babcock, Chen, & Zhuang, 2004) and Rhodamine (Fernandez-Suarez & Ting, 2008) are membrane permeable and may have rapidly diffused out of the cells. The dye alone may also be toxic to the cells when not stabilized on a tRNA molecule. Many cells injected with dye alone showed cell-death indicators such as shriveling, blebbing, and

rounding of the nucleus. The permeabilization of the cell membrane during cell death may further explain the rapid decrease in intracellular concentration as the dye diffused out. We have observed differences in dye distribution in different isoacceptors Figure 28A and B, dye alone, Figure 28C and D, bulk tRNA, Figure 28E and F, and the same isoacceptor, Figure 28G and H.

Possible explanations for these discrepancies in dye behavior include differences in interaction with the lipid bilayer (Hughes et al., 2014), free dye in solution, or a perturbation in the energy barrier for nuclear-cytoplasmic trafficking. The green dyes, Rhodamine and Alexa 488, will tend to have more free (unbound) dye in solution and may necessitate an additional chromatographic step prior to microinjection studies. This unfortunately decreases the fl-tRNA yield, but should improve purity. There could also be differences in non-specific dye adhesion to tRNA molecules.

In the case of unbound or non-specific adhesion of dye, we would expect the unbound dye to leave the cell as seen in control tests, which we believe to be primarily a consequence of the dyes' membrane permeability. If the free dye is indeed toxic to cells as we speculated in our control test (Figure 28C and D) this toxicity could be mitigated by the lower concentration of free dye relative to the dye bound to the fl-tRNA. In addition, elevated tRNA levels are known to confer apoptotic resistance to cells and the injection of additional tRNA may impede the normal cell death pathway (Hou & Yang,

2013; Mei, Stonestrom, et al., 2010; Mei, Yong, Liu, et al., 2010; Mei, Yong, Stonestrom, et al., 2010).

5.3.3 tRNA Localization During Nutrient Deprivation

Consistent with FISH studies (Hopper, 2013; Kramer & Hopper, 2013; Murthi et al., 2010), we found that nutrient deprivation of cells resulted in nuclear accumulation of tRNA on a rapid and observable timescale, on the order of 5 minutes. This is time resolution that is not attainable via FISH methods, and emphasizes the utility of our technique for accessing previously unobservable dynamics. Figure 29 shows the spinning disc confocal images of a cell immediately after injection (A) and after 30 minutes of nutrient deprivation (B). Image C is a higher resolution micrograph, which shows more subcellular detail. It can be seen that the tRNA accumulates in the nuclear periphery, granular regions in the nucleus, and in fibrous regions in the cytoplasm, believed to be either the endoplasmic reticulum or microtubules (or both). Microtubules are implicated in the transport of a wide array of molecular species within a cell (Vihinen-Ranta, Yuan, & Parrish, 2000), and may direct and facilitate tRNA intracellular trafficking behavior.

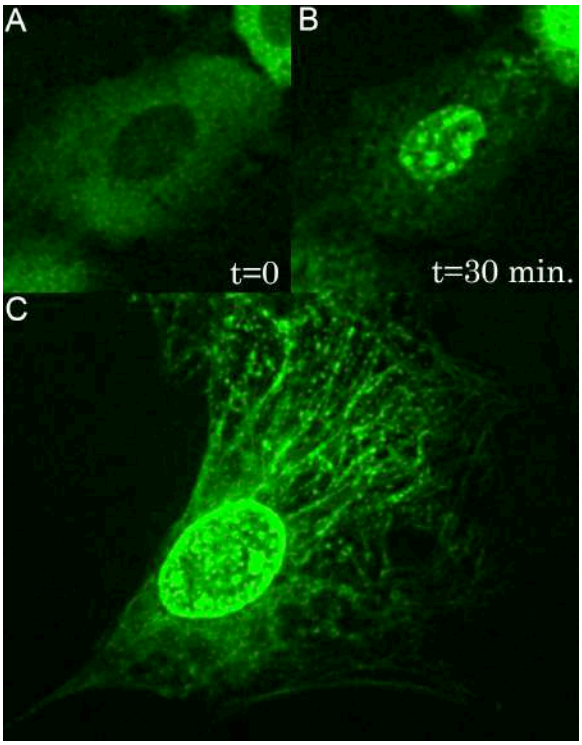

Figure 29. Rhodamine-labeled bulk tRNA localization during nutrient deprivation of MEF cells. (A) Immediately after microinjection with tRNA. (B) 30 minutes after microinjection w/ tRNA. (C) Higher resolution image after localization. This is a different cell than the one pictured in (A) and (B), but it is from the same experiment. tRNA accumulates in nuclear periphery, granular regions in the nucleus, and in fibrous regions in the cytoplasm believed to be endoplasmic reticulum or microtubules. We can observe localization and trafficking dynamics.

It should be noted that dye effects were *not* observed during nuclear accumulation resulting from nutrient deprivation. Both Cy3 and Rhodamine labeled tRNA behaved similarly, localizing to the same regions in the cell on the same time scale. This suggests that the nuclear accumulation effect is fairly strong relative to other factors that affect fl-tRNA distribution. The

benefit to this is that we can apply our previous analytical model to attain dynamics and kinetic information for tRNA nuclear accumulation.

We analyzed the ratio between the mean intensity in the nucleus and cytoplasm using Mathematica to fit kinetic parameters from our model to the experimental data. A sample curve fit to our kinetic model is shown in Figure 30A. In each curve fit, we assume a volume ratio, φ, of 0.1, based on the average cell volume occupied by the nucleus (Alberts et al., 2007), and fit three parameters: k_{in}, k_{out}, and a time offset to account for any time lost between the instant of injection and imaging. There is typically 1-5 minute delay between injection and imaging. It is possible to image concurrently with injection but is logistically more difficult and limits imaging to a single cell at a time. This is because the pipette must be oriented above the injection location of interest, the scope must be carefully focused on the cell of interest, and confocal imaging must be performed as the injector is slowly lowered into the cell. If any parameters are incorrect this can result in pipette breakage, cell death, or lack of injection. Our automated injection system would mitigate many of these concerns and allow for a user to target multiple cells for injection while imaging.

We were unable to use a nuclear stain due to microscope limitations, however a live-cell nuclear stain would open up the possibility of automated image processing, which would improve throughput and accuracy. Data is well fit by our model and typically resembles a simple exponential. We

explored the distribution of the k_{in} and k_{out} values in Figure 30B. We found the distribution to be approximately lognormal. The kinetics of some microtubule transport processes are known to be lognormal distributed (Zaliapin, Semenova, Kashina, & Rodionov, 2005) which may suggest a possible transport mechanism, with microtubules guiding the active transport of tRNA to the nucleus. For a lognormal distribution, the geometric mean is a more appropriate for characterization, rather than the arithmetic mean which is skewed by the outliers on the right end of log scale (Navidi, 2008). The geometric means of the rate constants provide the first known measurement of tRNA nuclear/cytoplasmic transport kinetics and are presented in Table 2. The spread of the data can be represented by the standard deviation of the natural log of the data set for a lognormal distribution, which is also shown in Table 2.

Table 2. tRNA nuclear accumulation in MEF cells during nutrient deprivation: kinetic parameters, N=34.

tRNA Label	Rate Constant	Geometric Mean	StDev(ln(k))
Rhodamine	k_{in}	5.8e-3 s^{-1}	7.5e-1
	k_{out}	3.8e-3 s^{-1}	7.5e-1
Cy3	k_{in}	6.2e-3 s^{-1}	9.2e-1
	k_{out}	4.0e-3 s^{-1}	9.5e-1

A comparison of the Rhodamine and Cy3 data shows that they are not statistically significantly different (P=0.37 for k_{in} and P=0.41 for k_{out}) using a large sample (N>30) test for difference between two means using the normally distributed natural logarithm of the data (Navidi, 2008).

Taking the ratio of the mean data for k_{in}/k_{out} yields values of 1.53 and 1.55 for Rhodamine and Cy3, respectively. This is self-consistent with the mean of the ratio data for individual cells (Figure 30C), which was found to be 1.57 and 1.56 for Rhodamine and Cy3, respectively. This means that on average, under nutrient stress, the cell will reach a steady-state concentration of tRNA that is 1.5-1.6X greater in the nucleus compared to the cytoplasm for the experimental conditions used here.

With a measurement of the trafficking kinetics, we can now check our previous assumption that concentrations are uniform within the cytoplasm and nucleus. This assumption is true if the diffusive time scale is much faster than the time scale for nuclear/cytoplasmic trafficking. We can test this using a Damköhler number, defined in Equation 32.

$$Da = \frac{ka^2}{D}$$

Equation 32.

Here, Da is the Damköhler number, k is the rate constant for nuclear/cytoplasmic trafficking, a is the length scale for diffusion, and D is the diffusion coefficient of the species of interest. The Damköhler number defined here represents the ratio of the diffusive time scale to the trafficking time scale. Using the largest measured rate constant for k_{in}, 6.2e-3 s^{-1}, a MEF cell radius of 20μm (typical MEF cell size) for the diffusive length scale, and a diffusivity of 7.0e-7 cm^2/s for tRNA (Potts, Ford, & Fournier, 1981), we calculate a Damköhler number of 3.5e-2. The smallness of this number (<<1)

suggests that the diffusive time scale is much faster than the trafficking kinetic time scale. This confirms that our assumption was accurate and we can indeed consider the concentrations as uniform in our analytical model.

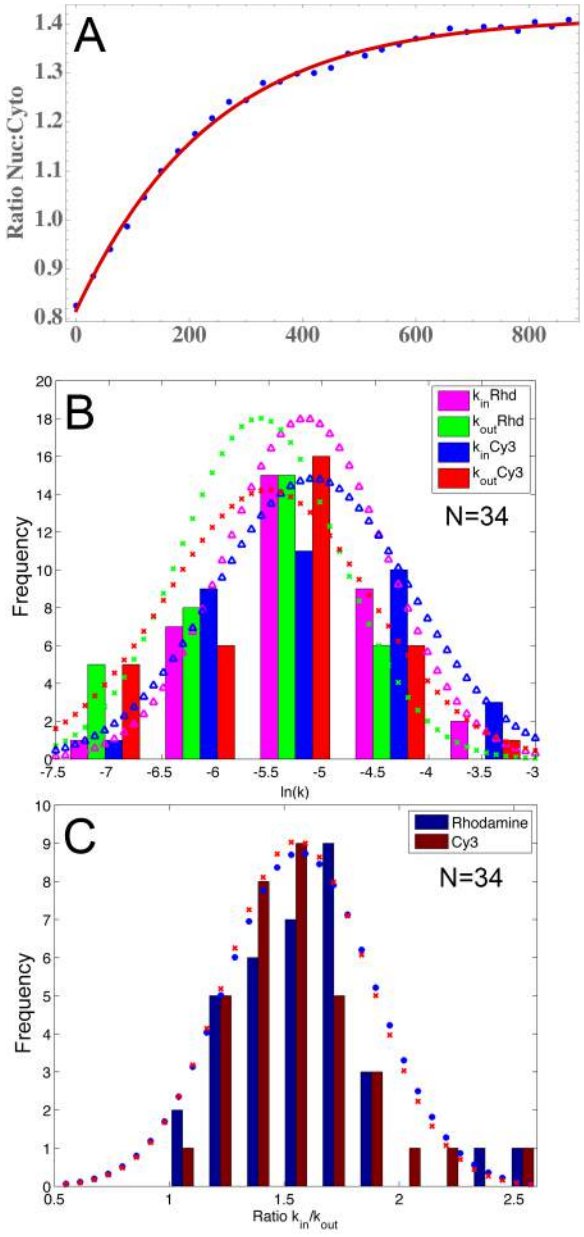

Figure 30. tRNA Nutrient Deprivation Kinetics. (A) Sample curve fit of the ratio between nuclear and cytoplasmic mean intensity during nutrient deprivation and tRNA nuclear accumulation. Symbols represent experimental data and the red line

is the Mathematica curve fit to our model. (B) Natural logarithm of the kinetic parameters extracted from nutrient deprivation. Histogram represents experimental data for k_{in} and k_{out} for both Rhodamine (magenta and green, respectively), and Cy3 (blue and red, respectively). The curves are the best Gaussian fit to a lognormal distribution. The triangles correspond to k_{in}, and the crosses to k_{out} for the two dyes, N=34. The k_{in} distribution is shifted to the right relative to the k_{out} distribution indicating nuclear accumulation. (C) Histogram of the ratio of k_{in}/k_{out} for individual cells during the same nutrient deprivation experiment in (B) for Rhodamine (red) and Cy3 (blue). k_{in}/k_{out} values >1 indicate nuclear accumulation. Curves represent best Gaussian fit for Rhodamine (blue asterisks), and Cy3 (red crosses).

It was also of interest to see if the nuclear accumulation was reversible. Figure 31 shows results from an experiment in which cells were microinjected with bulk tRNA and left to incubate for an hour while they were imaged (Figure 31A(i) and B(i)). After incubation, the media was depleted and cells were imaged for 50 minutes (Figure 31A(ii) and B(ii)). After 50 minutes of nutrient deprivation, the media was replenished (Figure 31A(iii) and B(iii)). MEF cells are quite active, and upon nutrient deprivation they stopped migrating, and there was some nuclear accumulation of the tRNA seen in both Rhodamine and Cy3 channels. After the nutrient replenishment the cells resumed their normal migration activity and within 10 minutes the nuclear accumulated tRNA was seen to be redistributing and was less concentrated in the nucleus. The ratio of nuclear to cytoplasmic

mean intensity for the cell indicated in Figure 31A and B is plotted in Figure 31C. For both dyes, the ratio increased upon nutrient deprivation (nuclear accumulation), and then decreased upon nutrient replenishment. The effect was most clearly seen in Rhodamine (nuclear to cytoplasmic intensity ratios of 1.39→1.92→1.13), but was also seen in Cy3 (nuclear to cytoplasmic intensity ratios of 1.03→1.12→1.04). This result was interesting and suggests that tRNA nuclear accumulation is indeed reversible and likely serves a regulatory mechanism in cells as others have suggested (Hopper, 2013; Huang & Hopper, 2014; Kramer & Hopper, 2013; Murthi et al., 2010; Whitney, Hurto, Shaheen, & Hopper, 2007). This experiment does raise some questions however, as there was not as much nuclear accumulation as was seen in the experiments of Figure 29 and Figure 30 and it wasn't as ubiquitous or fast. Also after nutrient replenishment, the fluorescence began to fade rapidly for unknown reasons. I speculate that there may have been residual media with nutrients that may have interfered with the rapid response that was seen previously. Due to lack of a robust perfusion system, the media was changed carefully via syringe such that the petri dish was not moved and the imaging field of view could be preserved. The media was rinsed twice with the nutrient-free mix, but it is plausible that the rinse was not thorough enough to sufficiently dilute remaining nutrients. It is also possible that these cells are at a different stage of the cell cycle compared to previous experiments with confluency closer to 70%, which is on the low end

of the range used for experiments. The previous response was reproducible and three separate experiments comprise the data in Figure 30, so we have some confidence in those results. Nevertheless, this experiment is a good example of the type of factors that can be investigated with this novel technique.

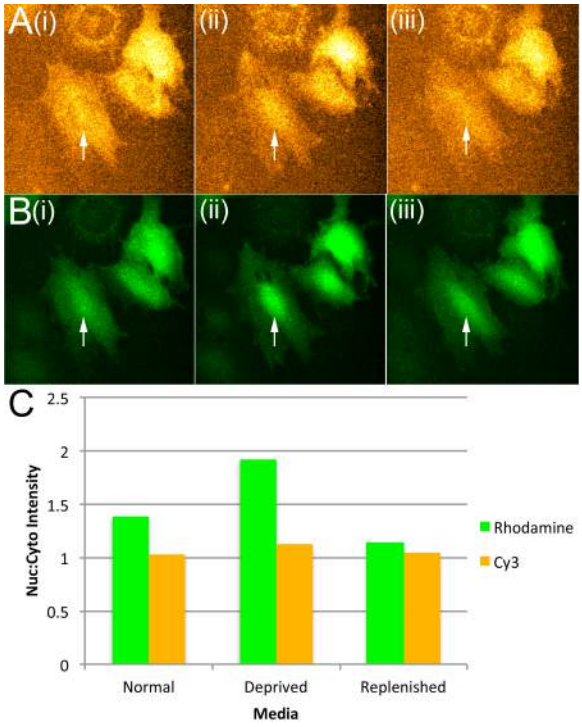

Figure 31. Reversibility of tRNA localization during nutrient deprivation. (A) MEF cells coinjected with 25µM Cy3 bulk tRNA and (B) 25µM Rhodamine 110 bulk tRNA. Cell of interest is indicated with a white arrow pointing towards its nucleus. (i) Cells one hour after injection in normal media. (ii) After one hour in normal media, the cells are switched to nutrient-deprived (amino-acid free DMEM) media for 50 minutes. Some nuclear localization is seen. (iii) Media replenished and within 10 minutes the tRNA is seen redistributing. (C) Ratio of nuclear to cytoplasmic mean intensity for the cell indicated with the white arrow in (A) and (B) for Rhodamine (green) and Cy3 (orange). The ratio was taken after 60 minutes in normal media

("Normal"), after 50 minutes in amino-acid deprived media ("Deprived"), and 6 minutes after media replenishment ("Replenished").

5.3.4 tRNA Localization During Cell Death

Early injection studies with fl-tRNA showed that cells undergoing cell death (necrosis or apoptosis) demonstrated a rapid accumulation of tRNA in the nucleus, as shown in Figure 32. The rapid nuclear accumulation was typically associated with visible signs of cell death (i.e., membrane blebbing, shriveling of the cell, rounded nuclear profile, and eventual substrate detachment). This may be a more extreme cellular response to stresses as seen in the nutrient deprivation study, or may be the result of a different mechanism. For example, CytC is released from the mitochondria and triggers the apoptotic pathway of a cell. tRNA has been shown to bind and inhibit the action of CytC (Hou & Yang, 2013; Mei, Stonestrom, et al., 2010; Mei, Yong, Liu, et al., 2010; Mei, Yong, Stonestrom, et al., 2010), so this localization to the nucleus may prevent normal cellular tRNA from interfering and inhibiting the normal cell death pathway.

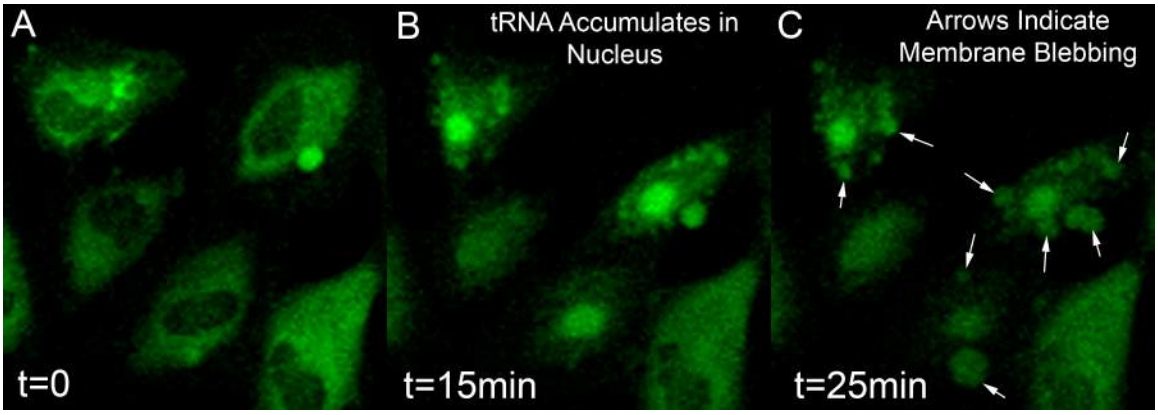

Figure 32. tRNA accumulates in the cell nucleus during cell death. (A) HeLa cells, injected with Cy5-tRNA at time 0. (B) Within 15 minutes, tRNA has clearly accumulated in the nucleus. (C) Within 25 minutes, signs of cell death are present, including shriveling, shrinking and rounding of the nuclear profile, and membrane blebbing.

5.4: Conclusions

We have recently optimized live-cell imaging and injection parameters for tRNA trafficking studies, and our technique appears highly promising from these preliminary results. We have begun to see phenomena that have not been previously reported, such as the nuclear accumulation of tRNA during cell death. We also quantified nuclear/cytoplasmic trafficking kinetics with a time resolution not feasible via FISH techniques, providing the first known measurements of nuclear/cytoplasmic trafficking kinetics of tRNA using a simple model that fits our data well. We anticipate that fl-tRNA microinjection could lead to a better understanding tRNA dynamics, the mechanisms and purpose of tRNA transport, and the cellular processes that regulate them. We hope that in the long term, such studies will provide

researchers with a better understanding of the links between tRNA dysregulation and disease.

The major hurdle to current studies is the discrepancies in tRNA distribution with different fluorescent labels. While we have shown that microinjection is a reliable technique for measuring nuclear/cytoplasmic trafficking kinetics, it is important to understand dye effects in order to attain kinetics for control cells. Without this data it will not be possible to quantitatively compare rate constants relative to normal cellular behavior, and dye effects will be a concern in any experiment moving forward. Furthermore, limitations in dye selection may limit the capabilities of future experiments.

Chapter 6: Conclusions

6.1 Summary of Research

Carbon nanopipettes are a powerful tool for microinjection and cell probing. We have demonstrated that using the carbon lining as an electrode surface in an AC impedimetric scheme allows us to detect cell penetration with sub-micron spatial and millisecond temporal resolution without the need for redox mediator or presence of solution in the pipette, and without disrupting normal cell viability or function. We find a statistically significant difference between penetrating or injecting in the cytoplasm vs. nucleus, and we have found that when used purely as nanoelectrodes CNPs are extremely sensitive to cell penetration depth and capillary rise, opening the possibility for feedback of subcellular nanoelectrode placement and electrochemical nanosampling of small volumes, respectively. The behavior of these feedback signals are well characterized by an equivalent circuit model.

Solid CNPEs are suitable for use as pure nanoelectrodes. The template-based batch fabrication results in CNPEs being inexpensive, geometrically tunable, of nanoscale dimensions, and compatible with existing micropipette fittings for amplifiers, pumps, and micromanipulators, thereby readily adaptable by laboratories equipped with standard electrophysiology equipment. We have worked with researchers at UVA to develop CNPEs for use in neurotransmitter detection in *Drosophila*, towards developing them as a model organism for neuroscience studies. CNPEs have a sharp geometry

that is advantageous for penetrating the tough glial sheath of the fly brain and performing *in vivo* localized measurements. The behavior of CNPEs for FSCV applications was characterized for dopamine, serotonin, and octopamine neurotransmitters.

As a target application for microinjection studies with CNPs we have been working with the Cooperman Lab to study the dynamics of tRNA subcellular trafficking via the microinjection of fluorescently tagged tRNA. We have successfully developed a simple model to capture membrane transport kinetics and have shown that tRNA labeling affects tRNA subcellular distribution, and that nutrient deprivation of amino acids results in significant subcellular localization of tRNA, on the order of 1.5X greater concentration in the nucleus relative to the cytoplasm. We were able to fit this data to our model to attain rate constants for tRNA nuclear/cytoplasmic trafficking during nutrient stress of MEF cells. To our knowledge this is the first known measure of tRNA nuclear trafficking kinetics.

We have developed a Matlab-based semi-automated injection system to facilitate microinjection studies such as these. The Matlab GUI interfaces with commercial microinjection equipment, amplifiers, and CCD cameras for semi-automated microinjection. The Matlab integration makes it easily adaptable to novel studies in a laboratory setting. We have further incorporated the amplifier's LockIn output to provide electrical feedback during microinjection or probing when using CNPs, and we have performed

proof-of-concept semi-automated microinjection with electrical feedback. The system can also perform traditional semi-automated microinjection using a z-datum plane to define injection trajectory if CNPs are not being used for feedback. We anticipate that advancements in such systems will lead to improved success, consistency, and throughput of microinjection studies, with less training and tedious manual manipulation required from experimentalists.

6.2 Future Possibilities

In this section, I will describe some potential projects and areas of research that could be explored as an extension of CNP technology.

6.2.1 Automated Micropipette and Microelectrode Schemes

This thesis lays out the framework for cell penetration detection schemes to automate cellular microinjection and probing, but systems are still at the proof-of-concept stage. The system could be further developed to optimize microinjection parameters to improve speed, throughput, and the electrical feedback for various studies of interest. This framework could also be adopted to other techniques that require micromanipulation of small electrodes or pipettes relative to cells, for example patch clamp electrophysiology (Kodandaramaiah et al., 2012), scanning electrochemical microscopy (Amemiya et al., 2008), single-cell electroporation (Kang et al., 2013), or more advanced microinjection studies. Interfacing and synchronizing the GUI with a programmable microscope stage and computer

vision (Becattini et al., 2014) could lead to fully-automated systems which can independently actuate both stage and micromanipulator. Different regions of cells on the same dish could be affected in various ways, such as injection with varying concentrations. Performing the injections in the same dish is a powerful tool for biological research, since there would be single cell resolution, with automated throughput, and built-in experimental controls within the same dish. This would eliminate questions of biological variability or experimental error in culture preparation for controls. Automation could also be achieved without computer vision using cellular patterning (Charrier et al., 2010; Delivopoulos, Murray, MacLeod, & Curtis, 2009; Lau, Hung, Wu, & Lee, 2006; Voldman, 2006), or working with suspended cells that can be immobilized with an aspiration pipette. If the location of the target cell is known because they are trapped/patterned at specified locations, then the user need not have a live camera feed of the cells and computer vision algorithms would not be necessary, which could be desirable from the perspective of both throughput and reduced complexity.

6.2.2 Functionalized Carbon Nanopipettes

The biosensing field has developed a number of methodologies for the functionalization of surfaces for various purposes (Actis et al., 2010; Jacobs, Vickrey, & Venton, 2011; Katz & Willner, 2003). Subcellular electrochemical and spectroscopic probing is becoming a reality, and the field is new enough that there is significant room for exploration (Singhal et al., 2011; Sun et al.,

2008). For example, it has been shown that CNPs can be functionalized with gold nanoparticles (Vitol et al., 2009), and that gold nanoparticles can be used for surface enhanced raman spectroscopy (SERS) for intracellular biosensing on carbon nanotubes (Singhal et al., 2011). We have also demonstrated that CNPs can be electroplated with silver with nanoscale nucleation sites, as shown in Figure 3. Silver nanoparticles can also be used for SERS (Meyer & Smith, 2011). CNPs functionalized with nanoparticles could be inserted into cells in a minimally invasive manner, and used for multifunctional biosensing. For example, a user could perform electrochemical characterization using the carbon as an electrode, and SERS could be used to look at local changes in the nanoparticle environment.

Other types of functionalization could be explored, such as the use of ion-selective coatings like Nafion (Cahill et al., 1996), antibodies/aptamers (Katz & Willner, 2003; Y. Xiao, Uzawa, White, Demartini, & Plaxco, 2009), or biotin/streptavidin (Thompson & Bau, 2012). If carbon chemistry is insufficient for functionalization, the tips can be metallized as previously described, since gold and silver chemistries are commonly used for electrode surfaces and treatments. Platinization of carbon is also possible (Hu et al., 2013). One could also functionalize the quartz itself in some biosensing modes (Actis et al., 2010).

The benefits to functionalization are that surface modifications can improve specificity and sensitivity of detection. In some cases the specificity

is broad, such as Nafion, which is a cation-conductive surface coating that will tend to enhance transport of any cationic species to the electrode. It has been used in FSCV commonly to enhance detection of cationic neurotransmitters like dopamine. In other cases binding has molecular specificity, such as with aptamers and antibodies that are adsorbed or bonded to the surface. Chemical engineering breakthroughs have led to some novel surface chemistry that can actually enhance the response from these specific binding events in a tunable manner by coupling folding of DNA or proteins to target-binding (Y. Xiao et al., 2009). This folding or unfolding can result in measurable electrochemical changes, for example by coupling the folding event to a redox reporter that can be oxidized or reduced based on proximity to a surface (Simon, Vallee-Belisle, Ricci, Watkins, & Plaxco, 2014; Y. Xiao et al., 2009). If there is a measurable change in the local electrode environment, we should be able to detect it using electrochemical methods such as electrochemical impedance spectroscopy, or simply by monitoring capacitance or current magnitude (Katz & Willner, 2003), which are sensitive to the local electrode environment. As single-cell and subcellular studies come to the forefront of biological research, it will be important to develop novel biosensing technologies to report on intracellular species with high sensitivity and specificity. Single-cell probes with novel functionalizations represent one potential method for performing such measurements.

6.2.3 Cellular Nanosampling

We demonstrated in Figure 14 that the capacitance signal of a CNP can be used for feedback of capillary uptake of solutions. Alternative nanosampling modes have also been characterized (Yu et al., 2014). CNPs can target individual cells and subcellular regions, and electrochemical characterization of nanosampling behavior opens the possibility for extracting sub-femtoliter volumes of intracellular fluid for analysis. This could also scale up to provide electrical feedback for larger fluidic sampling, or even feedback for applications like nanoprinting to keep track of fluid levels within a nozzle/pipette.

6.3.4 Multiplexed Electrodes

The use of multiple CNPs or fabrication of CNPs and CNPEs from multi-bore capillaries opens up the possibility of recording multiple channels in parallel. Systems such as these have been explored (Lin et al., 2012; Schrlau, 2009), but not extensively used. The benefits to such an electrode array would be the ability to map local electrochemical responses, or to use different electrodes to measure different phenomena. For example, in FSCV, electrodes could be used with different optimized waveforms to detect multiple species simultaneously, for example, oxygen, dopamine, and serotonin. Electrodes could also be functionalized differently for multiplexed measurement of specific species. More advanced control schemes could also perform complex electrokinetic techniques, for example using

dielectrophoresis to manipulate cells or particles in proximity of the tip (Hunt, Issadore, & Westervelt, 2008), or applying electrical stresses to nearby cells for electroporation (Khine, Ionescu-Zanetti, Blatz, Wang, & Lee, 2007). Having control over an entire electrode array at such a small scale allows for very careful tuning of the local electric field, and very large fields can be attained at reasonable potentials. The difficulty in the successful implementation of such a system would be coordinating and acquiring data from multiple electrodes at the same time, selectively functionalizing different electrodes, and preventing cross-talk between adjacent electrodes that can obscure and complicate measurements and modeling.

6.2.5 Process Modeling

Chemical Vapor Deposition (CVD) and Chemical Vapor Infiltration (CVI) are relatively simple processes in practice, involving the flow of a precursor gas through a hot furnace with a sample in it. There are only a few parameters to adjust (temperature, flow rates, duration). The precursor decomposes and deposits material onto the sample. Understanding trends in the behavior and optimizing process conditions has proved elusive however, due to significant complexity in the process details. First, for CNP fabrication, the furnace is being operated in a reaction-limited temperature regime, which is inherently highly sensitive to temperature due to typical Arrhenius type dependence on rate constants. A small change in temperature can result in a large change in deposition rate. Secondly, the decomposition of

methane at high temperatures involves in excess of 200 intermediary reactions of varying importance, each with its own reaction rates (Norinaga & Deutschmann, 2007). All of these reactions are coupled and required for mass conservation. Lastly, it is important to consider the flow and geometric effects of the gas flowing through the tube furnace and the CNPs. This is complicated by the fact that a room temperature gas mixture is being flowed through a high temperature furnace. The heat transfer and temperature-dependence of gas properties such as density, pressure, and viscosity need to be considered, which is not trivial at high temperature, and relationships for gas mixtures must also be considered. There are also additional effects that play a role in deposition, for example hydrogen byproducts of the decomposition can inhibit carbon deposition (Li, Norinaga, Zhang, & Deutschmann, 2008). The model is further complicated by the scale of CNPs. At one end the CNP is nanoscale, while at the other it is millimeter-scale, and the furnace tube is centimeter-scale. This introduces numerical difficulties in producing an adequate mesh that is still computationally tractable for finite element models.

A robust computer model of CNP fabrication that could be verified with experimental results would be a major step forward in optimization of process parameters, in particular towards commercialization of CNP technology. It may be possible to make reduced-reaction models, with equivalent geometries, mutli-scale meshing, or hybrid methodologies that can capture

the deposition behavior of carbon from methane decomposition onto quartz capillaries and micropipettes (Birakayala & Evans, 2002). If such a model were successfully verified, it could provide a simple means for analyzing the parameter space of CNP fabrication to examine the effect of process conditions on carbon deposition characteristics and inform the fabrication process.

6.2.6 tRNA Studies

The tRNA microinjection technique described in Chapter 5 provides many possibilities for the study of tRNA subcellular dynamics. We dedicated a significant amount of time to optimization of the experimental setup, in particular moving to a stage incubation system on a spinning disc confocal microscope that minimizes phototoxicity and maintains the necessary temperature and pH for long-term cellular viability and imaging. Temperature control is important for both cell viability, and for ensuring accurate kinetic measurements. Experiments on a laser-scanning confocal confirmed that phototoxicity is a significant concern, and a spinning disc confocal is designed for improved time resolution and minimization of phototoxicity.

We focused our kinetic study on nutrient deprivation because other groups have shown it to result in nuclear accumulation of tRNA (Kramer & Hopper, 2013), and we were able to consistently confirm this fact in our experiments. There are a number of other factors of interest for trafficking, in

terms of their effects on normal behavior, including stresses such as heat shock, translation inhibitors, and apoptosis-inducing factors. It would also be interesting to explore differences in tRNA trafficking at different stages of the cell cycle, among different cell lines, at different tRNA concentrations, and any differences in isoacceptors or modified tRNA. One example would be to study the degradation of unmethylated tRNA. Cytochrome C is known to bind to tRNA and it could be interesting to look at apoptosis in cells with labeled CytC and tRNA, for example using cells with GFP-CytC and Cy3-tRNA. Apopotosis could be induced and the subcellular distribution of both could be monitored, including any FRET signal that may be indicative of binding.

6.2.7 Concentric Pipettes

Microinjection of suspended cells involves two pipettes, one larger polished pipette for aspiration, and a smaller, sharp pipette for injection. A small amount of suction is applied to the aspiration pipette while in proximity to a cell, causing the cell to be immobilized on the tip. Once immobilized, the injection pipette is moved into position and used to pierce and inject the cell. It would be beneficial if these two pipettes could be combined in a concentric fashion such that the injection pipette need not be moved relative to the aspiration pipette. This concept is depicted in Figure 33.

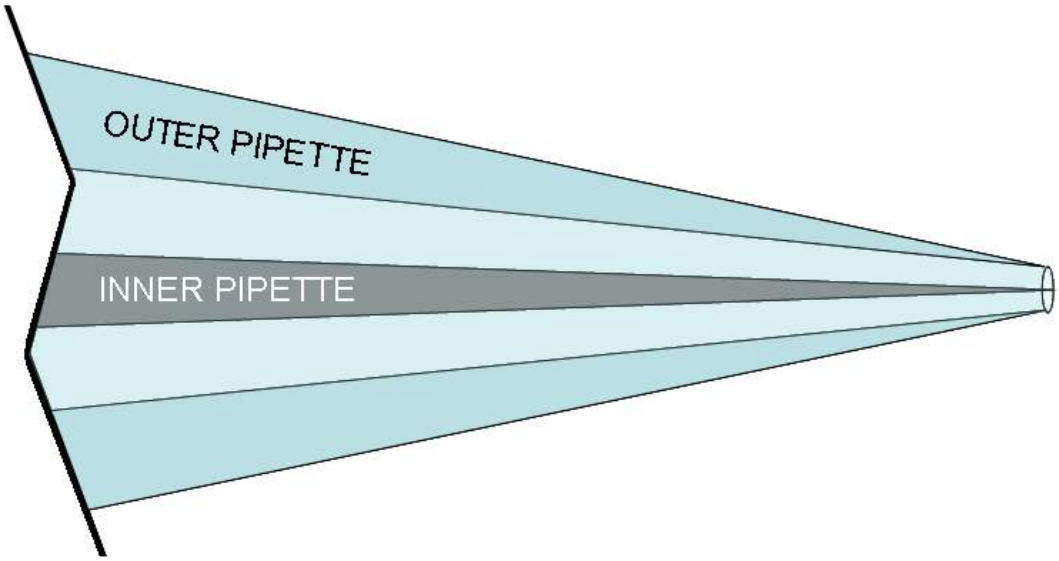

Figure 33. Concentric CNP concept. Not to scale.

If pipettes could be arranged concentrically, the outer suction pipette could pull nearby cells onto the sharp tip of the inner injection pipette. At this point the injection pipette could be triggered to inject the cell, and suction could be changed to a slight positive pressure to release the injected cell from the tip. This design is beneficial because it doesn't require coordinated motion of two separate pipettes. If there were sufficient cells in close proximity of the suction pipette then the system would not require coordinated motion at all. It could be inserted into a suspension of cells without the need for careful micromanipulation or even a microscope. An ionic current signal could be used to detect when a cell is properly trapped on the suction pipette, or our penetration detection scheme could be used as previously described to detect when the inner CNP penetrated a cell. This system could be easily scaled up,

and arrays of these pipettes could be used in parallel for improved throughput of single-cell microinjection of suspended cells.

Due to the electrode capabilities of CNPs the concentric orientation also opens some interesting options because a large outer CNP could be used as one electrode, with the inner CNP used as the other. This dot-ring arrangement could be used for DEP to manipulate cells or particles based on dielectric properties, or could be used for single-cell electroporation by applying a highly localized field with reasonable potentials.

The difficulty in implementing this concentric pipette design comes from pipette tip alignment. Several prototypes were fabricated that could couple these pipettes and provide independent fluidic access. However significant difficulty was encountered trying to align concentric pipette tips with accuracy of a few microns. If this hurdle could be overcome it could be a major step to a simple and high throughput injection system. Initial prototypes were fabricated from aluminum, but later designs used 3D-printing which allows for simple, inexpensive rapid prototyping of some of the small and complex geometries desired.

Appendix A: CNP Fabrication Protocol

A.1 Materials

- Capillaries
- Sutter P-2000 Pipette Puller
- Tweezers
- Quartz Boat
- CVD Furnace
- Methane/Argon w/ Flow Controllers
- Manipulator
- Pipette Friction Grip
- Hydrofluoric Acid
- Personal Protective Equipment

A.2 Method

A.2.1 Pulling Pipettes

1. Use pipette puller, Figure 34, to pull capillary into a micropipette
2. Typical program for quartz capillary 1.0mm OD X 0.7mm ID: HEAT 800 FIL 4 VEL 60 DEL 128 PULL 100
3. Program parameters can be incrementally adjusted to attain desired micropipette geometry per Sutter P-2000 manual

Figure 34. Sutter P-2000 Pipette Puller.

A.2.2 Loading the Furnace

1. Using tweezers, carefully place micropipettes in a stack on the quartz boat as shown in Figure 35A through D.
2. Quartz boats can be stacked if necessary. Select the boat configuration that results in pipette tips being close to the radial center of the furnace tube. Gradients in flow velocity and temperature are minimized at the tube center and will result in more uniform CNP batches.
3. In dry conditions (commonly in winter), static charge will tend to accumulate on pipettes, causing electrostatic repulsion. Care should

be taken in placing pipettes such that the tips are not contacted. This is not a significant concern in moderate/high humidity.

4. After placement in the boat, the distal ends of the pipettes should be roughly aligned. This can be done by tapping the flat end of the tweezers against the distal end of the stack carefully as shown in Figure 35C.
5. After alignment, pipettes should be shifted in the axial direction such that the tips extend well past the edge of the quartz boat, but obviously not so far that they fall out, as shown in Figure 35D. The logic behind this is that it will minimize flow disruption near the tips due to the presence of the boat and so the flow profile experienced by different batches of pipettes will be consistent.
6. Retrieve our lab's 1.5" quartz furnace tube from its storage location and load it into the furnace. Secure the seal on the inlet end of the tube. Ensure that the tube is fully inserted into the coupling, that the O-ring has some vacuum grease on it, and that the collar is tightened snugly. Do not force anything, the couplings are a common source of tube chipping and breakage. Check the alignment if you have trouble with the fittings.
7. Place the loaded quartz boat(s) into the furnace tube and use the available welding rod to push it into the center of the furnace heating zones as shown in Figure 35E. A good reference is to align the

beginning of the micropipette taper with the center of the furnace. Keep this position consistent among batches, the temperature profile in the tube varies axially.

8. Once in position, remove the welding rod and secure the flow coupling at the outlet end of the tube in the same manner as described for the inlet. The loaded furnace should resemble Figure 35E.

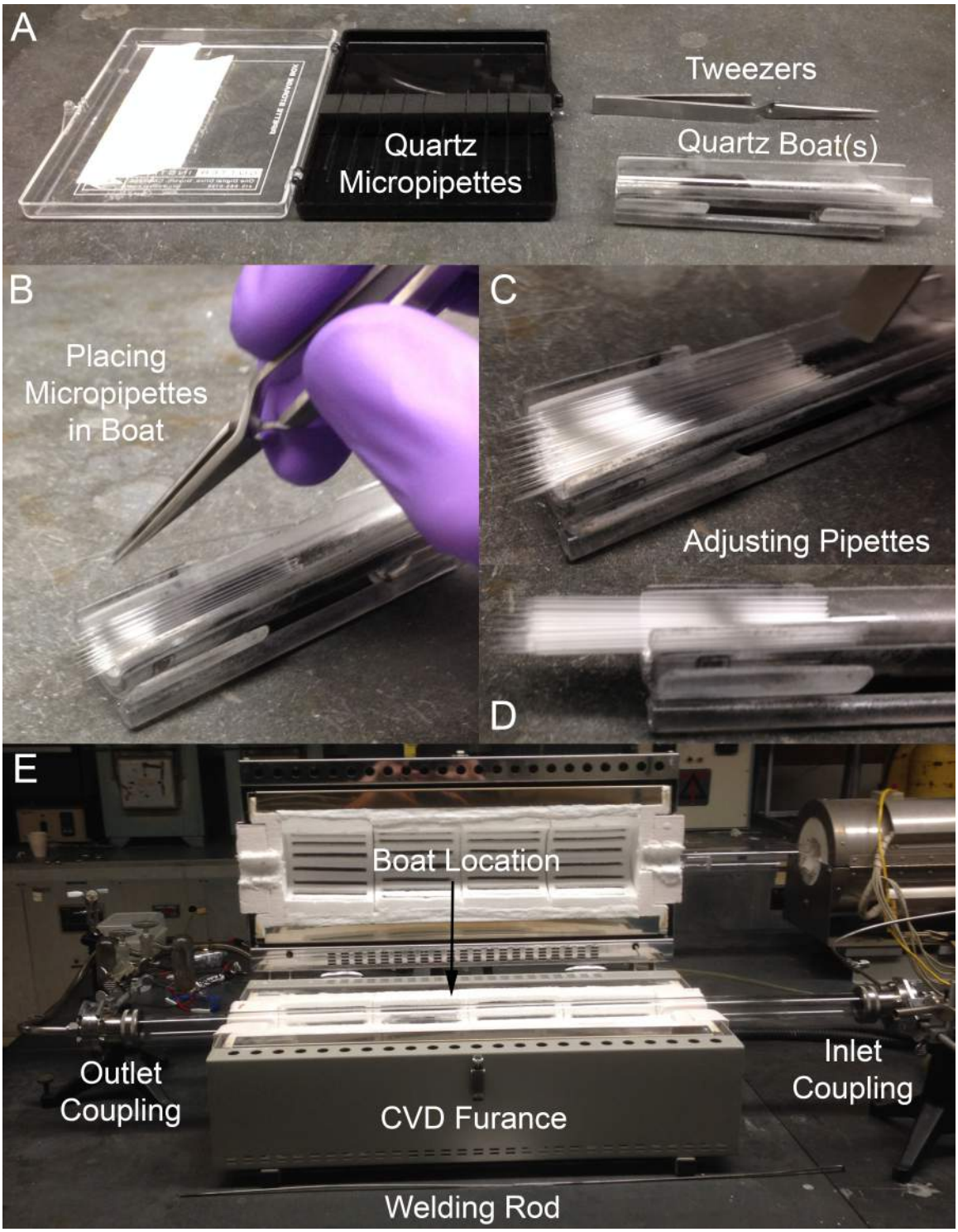

Figure 35. Loading the CVD Furnace. (A) Micropipettes, tweezers and quartz boats appropriately stacked and ready to load. (B) Loading micropipettes into boat. (C)

Adjusting micropipettes in the boat to the desired location, (D). (E) CVD Furnace with inlet/outlet couplings, boat, and welding rod labeled.

A.2.3 Furnace Operation

1. Check that the vent status light shown in Figure 36A is indicating green to indicate that the exhaust is properly vented.
2. Check that there is sufficient silicon oil in the exhaust trap. The exhaust gas bubbles through this oil and the interface prevents backflow of exhaust gasses into the tube. If there is insufficient oil for the gas to form bubbles, then add more.
3. Turn on both switches on the left side of the furnace controller shown in Figure 36B. The top switch controls the main power, the lower switch controls the power to the heating elements. Adjust the settings on the furnace controllers. There are three controllers corresponding to each heating zone (left, middle, right) with LCD readouts (they are reading "900" in Figure 36B). The left two controllers are type 201, the right was replaced several years ago with a type 301 controller. They have similar settings but different interface with the buttons on the front. The 201 controllers use the circular button to cycle through options and the up/down buttons to change/set the options. The 301 controller uses the page button to cycle through the options and up/down to change/set. Details of the operation of each are in the manuals in the drawer below the furnace controller. To start the 301

controller push the circular button which starts the heat and timer process. To start the 201 controllers, cycle the “Strt” setting to “run”. Settings of interest:

a. °C – 900 , Temperature in Centigrade
b. Sprr – 35, Ramp rate in degrees Centigrade per minute
c. tOpt – Opt 1, Timer option 1: see manual for discussion on timer options. Only for 201 controller.
d. duEll – 90, Dwell time in minutes. This is how long the furnace stays at the target temperature. Only for 201 controller.
e. Strt – run/off, Starts the heat when cycled to run. Only for 201 controller.
f. tnr – 90, Time remaining in minutes. Only for 201 controller.
g. t1 – 1.30, Dwell time in hours.minutes for timer option 1. This is only for controller 301.

4. Once the setpoint, ramp rate, and dwell time are set, start the heating. The square wave indicator light will begin to blink indicating that the heating element is being activated periodically.
5. You don’t want the tube heating without gas flow for too long.
6. Turn on the main power to the flow controller panel using the main On/Off switch on the panel above the furnace controller, see Figure 36B. This powers the emergency purge system. If a leak is detected, the purge will flush the system with argon to prevent any fires. The

purge also can be activated manually with the large red stop button. For this system to work, the argon must be connected with valves open. If this system is operation when you are hooking up the furnace tube, it will purge argon while the couplings are not fitted, and you will waste a lot of gas. Make sure it is off or the tank valves are closed when connecting and loading the furnace tube.

7. Open the main valve and needle valve on the Argon regulator on the tank (Figure 36A). Ensure that the regulator pressure is set to between 20-30psi. The flow rate will change with regulator pressure, if the argon tank pressure is low it may cause the regulator pressure to drop as the tank empties during deposition, be wary of this fact when fabricating batches with low argon levels.
8. Turn on the argon flow on the flow-control panel, and then adjust the flow rate with the needle valve connected to the argon flowmeter. The flowmeter calibration curve is located in the inside cover of the CVD logbook in the drawer below the furnace. I fit a curve to the calibration data and the best-fit equation is written next to it if you need to interpolate the data.
9. We typically operate at 600 sccm Argon flow, which is ~18.5 on the flowmeter scale. Read the scale at the centerline of the floating sphere. Ensure that the argon is bubbling through the silicon oil properly at the exhaust trap.

10. Use leak-check solution to check all major connections on the regulator for gas leaks.
11. Let the furnace reach the set point while under argon flow, and then wait a half hour at the set point for the temperature and flow to reach steady state. This half hour needs to be added to the duEll or t1 setting in addition to the target deposition time.
12. Once the remaining time reaches your target deposition time (you can check the remaining time with the tnr option on the 201 controllers), turn on the methane flow. Open the methane tank valve, set the regulator pressure to 20-30psi, and then open the needle valve (Figure 36A).
13. Turn on the MKS flow controller main power switch. Ensure that the channel readout is set to methane (currently channel 4), and check the setpoint. We typically use 400 sccm methane, (40% by volume). To adjust the setpoint use a small flathead screwdriver to turn the screw next to the setpoint switch. Do not do this often if possible, since the adjustment is fairly sensitive. Flip the read switch for the channel to on and then open the methane valve on the flow-control panel (Figure 36B). Ensure that the flowmeter is reading close to the setpoint (400).
14. Use leak-check solution to check the methane regulator for gas leaks.
15. When the target time is reached, the furnace heating elements will turn off and the control panel will read “End”. Shut off the methane

flow controller, and close all methane valves. You can lower the argon flow to a slow trickle, but ensure that there is some flow going through the furnace as it cools to prevent thermal stress buildup.

16. The furnace will take approximately 3 hours to cool. The furnace should never be opened above 250-300 degrees Centigrade. Below this range, the furnace can be opened, and the tube it will cool very rapidly. Before disconnecting the furnace tube couplings, ensure that the argon flow is turned off, and all argon valves are closed. Turn off the flow control panel main power to prevent argon purge. You may now remove the coupling at the outlet end of the tube. Never remove this coupling when the furnace temperature is above 250. The exposure of carbon to oxygen at elevated temperatures will result in oxidation of your carbon layer. Do not touch the furnace interior or the hot portion of the quartz tube.
17. Use the welding rod with the hook at the end to fish out your quartz boat with CNPs. The carbon deposition should show as a dark grey or black appearance of your pipettes. You may need to let the quartz boat cool for several minutes before it can be removed from the furnace tube.
18. For CNPs fabricated from 10cm capillaries using these parameters, you can expect 50-60nm of carbon deposition per hour. 45-75 minutes is usually sufficient for microinjection pipettes, and 180 minutes is

usually sufficient to seal the tip for CNPEs as described in Chapter 3. The deposition is most sensitive to temperature and pipette length. Longer pipettes will have higher deposition rates, as described in Singhal et al. (Singhal et al., 2010). Pyrolytic carbon deposition can be expected to follow an Arrhenius-type rate dependence, which is exponential with temperature. Above a critical temperature, the kinetics will transition from reaction limited to mass-transfer limited. Most CVD processes operate in the mass-transfer limited regime because it is easier to control mass flow than local temperature. In order to attain selective deposition within the CNPs but not outside the CNPs, we must operate in the reaction-limited regime, which is very sensitive to small changes in temperature. Too far below 900° C (~875° or below) and the deposition will be prohibitively slow or nonexistent. Too far above 900° C (~925° or above), and carbon will deposit on the exterior of the pipettes as well as the furnace tube. Thus it is recommended that the temperature not be significantly changed between batches. Dependence of pipette properties on methane composition and flow rate have been explored as well (Schrlau & Bau, 2009; Singhal et al., 2010; Vitol et al., 2009).

19. Unload CNPs from the quartz boat using tweezers.
20. Decouple the inlet end of the furnace tube after it has cooled. Put the furnace tube back in our storage location. Turn off the furnace via the

two switches on the furnace controller. Ensure that all gas valves are closed, including valves on the tank, regulator, and flow control panel.

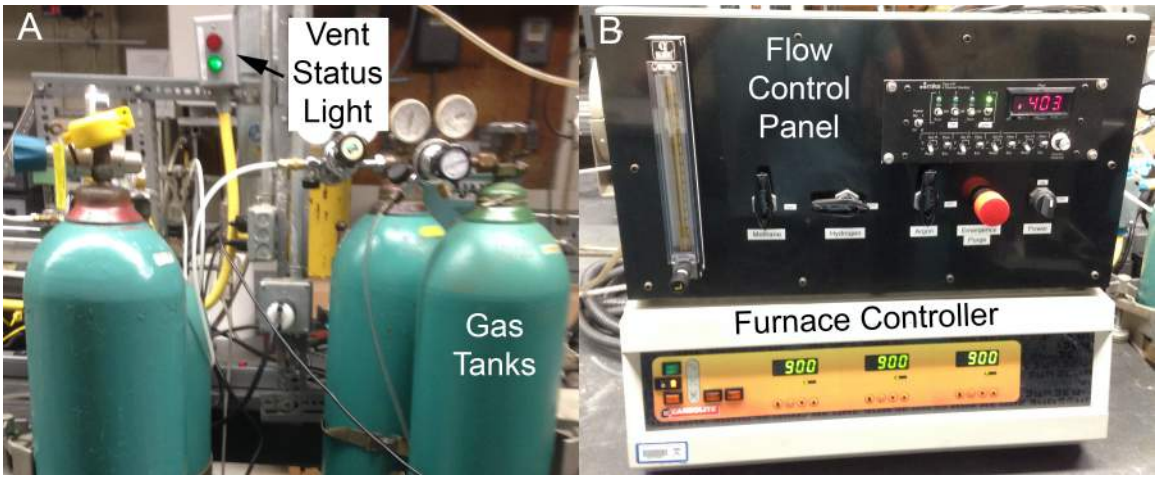

Figure 36. (A) Vent status light and gas tanks (Argon and Methane are used). (B) Flow control panel and furnace controller. Settings shown are during CVD of carbon.

A.2.4 Etching Pipettes

1. Load CNPs into the friction grip, and place the friction grip on the manipulator with tips pointing downwards. Place this setup in a fume hood. Wearing 2 layers of personal protective equipment (2x nitrile gloves, lab coat, apron, goggles, and face shield), retrieve a Nalgene container of Buffered Hydrofluoric Acid and place it in the hood. See Figure 37A for appropriate PPE.
2. HF Acid is one of the most dangerous chemicals to work with in any setting, it causes delayed deep tissue burns, and attacks calcium in bones and blood. Large exposures can cause cardiac arrest, and small

exposures can still result in deep tissue damage and necessitate amputation of digits and limbs. Treat HF with extreme respect, and ensure that you are always operating with every possible safety precaution in place, that you are aware of the dangers of HF, that there is an HF exposure kit nearby and that it is up to date and that you know how to use it. Know the location of eye washes and safety showers. Let others in the lab know when you are working with HF, and label all containers meticulously. Never work with HF alone or outside of normal work hours. Ensure that the hood is clear of any spill hazards and that you have a comfortable range of motion etc.… Perform a proper risk assessment before use.

3. Open the HF container and place below the pipette tips. Use the manipulator to lower the tips into the HF. When the desired etch time is reached, use the manipulator to retract the CNP tips from the HF and reseal the HF container. The manipulator and friction grip setup used to lower pipettes into HF is shown in Figure 37B.
4. Exposed length of carbon is linear with etch time for a given pipette geometry. Temperature and HF quality can affect this relationship but it is fairly consistent (~10% tolerance) for a given batch. Between batches the etch rate should be checked. A rough rule of thumb is 5-15 μm/min for the pipette program specified earlier.

5. Use the manipulator to lower the CNPs into a beaker of DI water and let rinse for 10 minutes. This will serve to dilute any residual HF, let it react with the glass in the pipettes and beaker, and will help clear some residual debris or salts if there are any on the tip.
6. Let CNPs sit for 1-2 days prior to use for microinjection.

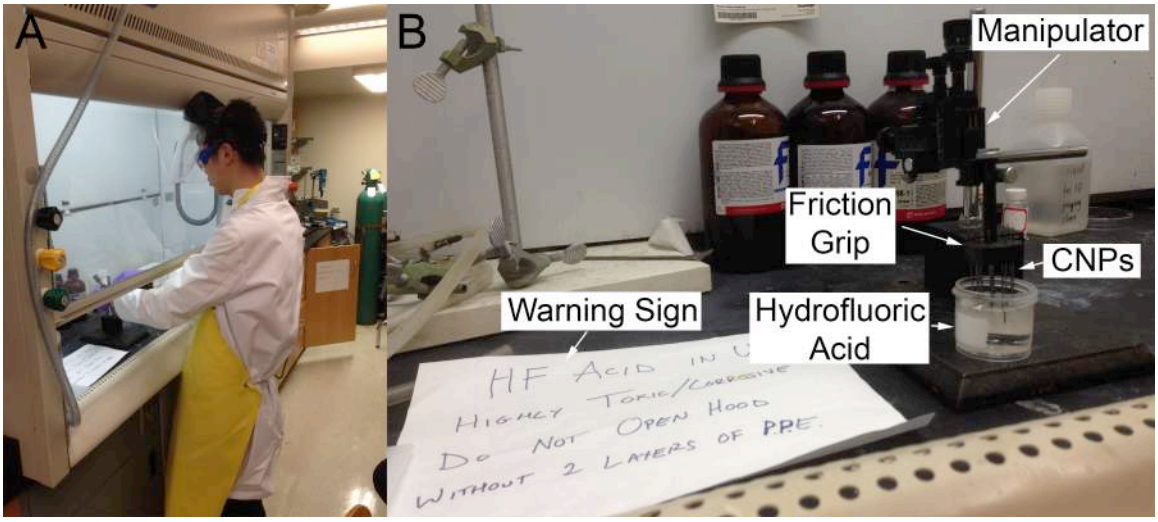

Figure 37. CNP Etch Process. (A) Researcher wearing appropriate PPE working in fume hood with Hydrofluoric Acid. (B) Etch setup. Manipulator holds a friction grip with 14 CNPs and lowers them into a container of HF Acid. A warning sign is present to notify other workers in the lab of the presence of HF.

Appendix B: CNP Characterization

B.1 Materials

- CNPs
- HEKA EPC 10 Amplifier
- Eppendorf Femtojet Microinjection Pump
- Eppendorf Transferman NK2 Micromanipulator
- Olympus BX-51 upright scope with 100X objective
- Olympus IX-71 inverted scope
- FEI Quanta 600 ESEM
- Carbon Tape

B.2 Methods

B.2.1 Optical Microscopy

1. Place the CNP tip under the scope at 100x magnification and focus on the tip.
2. Adjust the upper and lower illumination.
3. The thin quartz layer near the quartz/carbon interface will appear with a rainbow pattern, possibly due to constructive/destructive interference with light when the quartz thickness is on the same order of magnitude as the light wavelength. This is depicted in Figure 38. The carbon will appear bright white. The tip can be imaged and

measured with proper calibration in ImageJ using the known pixel size of the CCD camera and scope magnification.

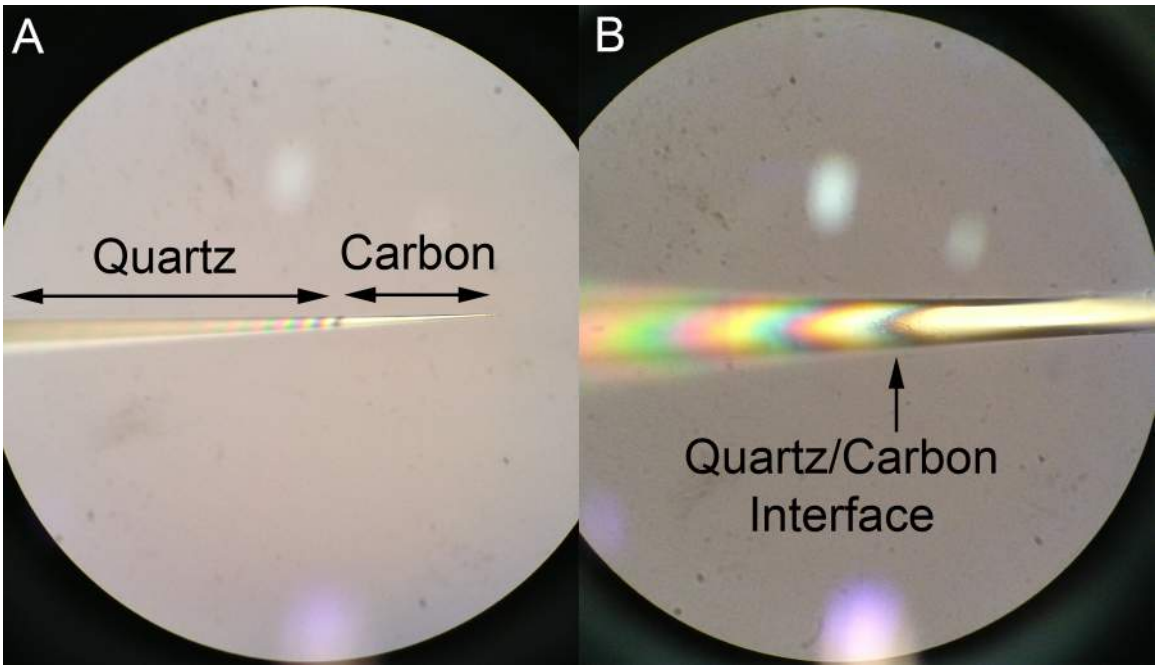

Figure 38. Optical microscopy characterization of CNPs. (A) CNP tip with quartz and carbon labeled. (B) Higher magnification micrograph of same CNP in (A), with quartz/carbon interface labeled.

B.2.2 Electron Microscopy

1. Lay down two parallel strips of double-sided tape on a disc-shaped Quanta sample-mount with stem.
2. Place CNPs on the double sided tape. Ensure that tips are roughly aligned. The CNPs should be supported just below the beginning of the tip taper. Pipettes should be spaced at ~1mm intervals. Typically 6-10 pipettes can be secured to a single sample holder.

3. Apply two strips of double-sided carbon tape over the top of the CNPs. Using tweezers, ensure that the carbon tape is in good contact with the top surface of the CNPs, and is in contact with the sample holder in between pipettes.
4. Load the pipettes into the SEM.
5. SEM should be operated in high vacuum mode, with low accelerating voltage of 2keV, and a low working distance of 5mm. The low accelerating voltage reduces charging effects and enhances surface detail (Joy & Joy, 1996) as depicted in Figure 39. Follow standard focusing and stage movement protocols to prevent sample contact with the electron source column or any other hardware.

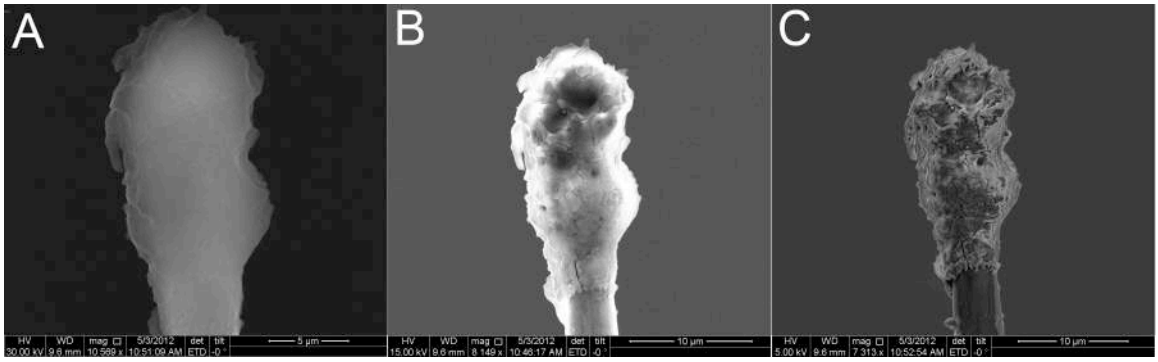

Figure 39. Effect of accelerating voltage on charging and surface detail. Fouled CNP tip shown. (A) 30 keV. (B) 15 keV. (C) 5 keV. The low accelerating voltage provides the best surface detail and least amount of charging.

6. Basic focusing protocol:
    a. Perform lens-align. The screen will flash between two images of the field of view, adjust the alignment until the images are

perfectly aligned and appear to be “pulsing”. Up/down movement between flashing images requires left/right adjustment of the alignment, and vice versa which can be counter-intuitive.

b. Focus.

c. Adjust left/right stigmation. Move left until out of focus, move right until out of focus, and then set the stigmation in the middle where the image is most in foucs.

d. Adjust up/down stigmation. Same procedure as left/right.

e. Repeat stepts b-d, in that order, as many times as necessary.

f. Zooming in on a smaller feature and optimizing focus and stigmation will provide a better image. A smaller scan region and higher dwell time can also help with focusing by making smaller features more clear.

7. Artifacts and effects to be aware of:

a. At low magnification adjusting the field of view triggers the stage to move via motor. At high magnification it moves via beam deflection. If the beam deflection is near the extrema then there will be artifacts in the motion and the image will jump around as you try to move by double-clicking. If this happens, re-center the beam deflection and adjust the field of view via stage motor using the middle mouse button.

b. If there are periodic noise effects in the image (wavy distortion), reset the EM field cancellation system in the room.

c. Charging is minimized by good grounding and low accelerating voltage, but is still a common issue. Focusing must often be done dynamically, "chasing" the pipette as it drifts out of the field of view. Dwell times need to be carefully selected such that you get good image quality but not too much drift. Charging can often affect brightness and contrast over time, and they must be compensated accordingly. If longer dwell times are causing charging issues, try using shorter dwell times with image averaging or integration to get clearer images. The one benefit to charging is that it tends to provide nice contrast between the dielectric quartz and the conductive carbon.

8. Typical imaging will include the quartz/carbon interface, the entire exposed carbon tip, and a higher magnification image of the CNP tip to measure the tip diameter. Image anything strange. A sample SEM image is depicted in Figure 40.
9. To image the tip opening, CNPs can be mounted vertically in the SEM. Extra Care should be taken to set the working distance and adjust the viewing angle.

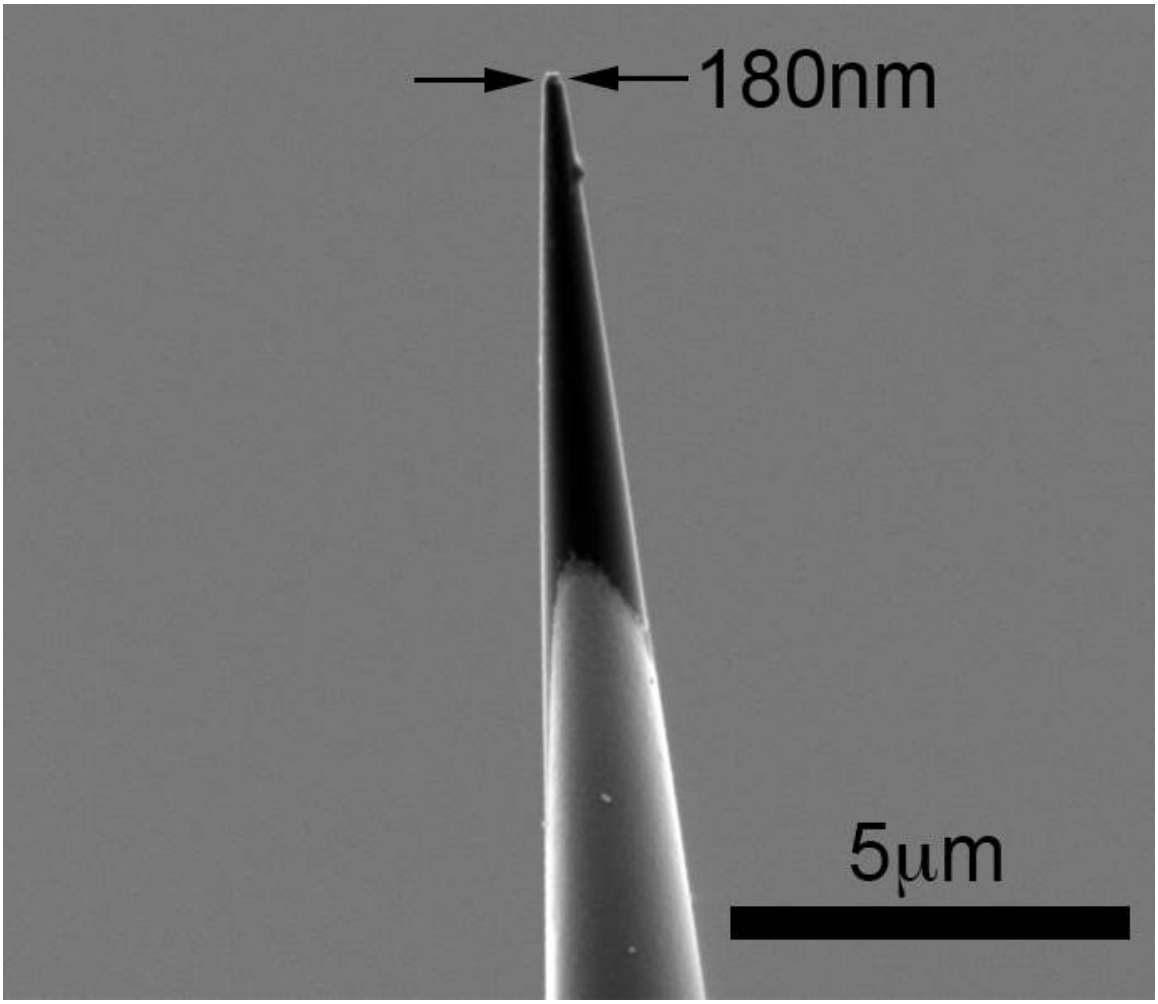

Figure 40. Sample CNP SEM image of a ~10μM exposed CNPE tip of 180nm tip diameter. There is clear contrast between the bright quartz and dark carbon.

B.2.3 Capacitance Characterization

1. Secure a CNP to the headstage of the HEKA EPC 10 patch clamp amplifier using the 1.0mm pipette holder. The wire connection should be in contact with the carbon layer. The headstage should be mounted on the micromanipulator. The manipulator should be mounted to the IX71 inverted scope, and the pipette holder should be connected to the

Eppendorf Femtojet microinjection pump. This setup is depicted in Figure 41.

2. The ground connection of the headstage should be made to a Ag/AgCl wire which will serve as a counter and reference electrode.
3. A petri dish with salt solution, typically PBS1X, should be placed on the inverted scope. The CNP tip should be lowered into the solution via micromanipulator, and the counterelectrode should be inserted into the solution. The CNP capacitance characterization setup is pictured in Figure 41.
4. A burst of pressure, between 100-300 kPa for 1s, should be applied to the CNP and the CNP tip should be observed. If any bubbles emanate from the tip, it is indicative of an open, and likely broken CNP tip.
5. If no bubbles are seen, measure the capacitance of the CNP tip interface using the LockIn module of the HEKA EPC 10's PATCHMASTER software. Apply a burst of pressure and observe the capacitance signal. If the pipette is open, the burst of pressure will force fluid out of the pipette and result in a drop in the capacitance due to the reduction of the interfacial electrode area. If no capacitance change is observed, then it is indicative of a sealed pipette.
6. The fluid-free pipette capacitance can be used as a measure of exposed electrode area. Under similar experimental conditions, CNPs can be normalized by this capacitance, which is analogous to surface area.

The surface area can also be calculated based on the capacitance from GCS theory (Bard & Faulkner, 2000). A common method for accurate surface area measurement is the Parsons-Zobel plot which requires measurements of capacitance in varying salt concentrations (Trasatti & Petrii, 1992).

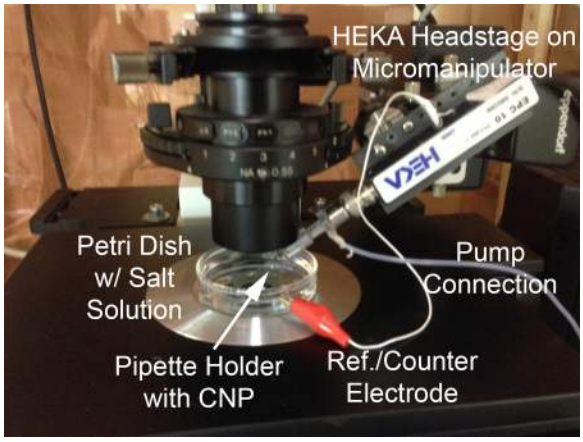

Figure 41. Capacitance characterization setup. A CNP is mounted on a HEKA headstage which is mounted on a micromanipulator which is mounted on an inverted microscope. The pipette coupling is connected to a microinjection pump and the ground is connected to a reference/counter electrode in solution. The CNP tip is immersed in a petri dish filled with PBS or other simple salt solution such as KCl.

Appendix C: Cell Culture Protocol

C.1 Materials

- Culture Medium
- Fetal Bovine Serum
- Penicillin/Streptomycin Antibiotics
- 10mL serological pipettes
- 2mL aspiration pipettes
- 70% Ethanol
- 15mL Centrifuge Tubes
- Paper Towels
- Dimethyl Sulfoxide (DMSO)
- Cryostorage tubes
- Centrifuge
- Heated water bath
- CO2 Incubator
- Cell culture flask
- Inverted microscope
- Gloves

C.2 Methods

C.2.1 Sterile Technique

1. Wear basic PPE (lab coat, gloves, goggles).

2. Wipe down all surfaces in the sterile hood with 70% ethanol. Spray and wipe down any items being brought into the hood. Spray gloves regularly and after any contact with non-sterile surfaces.
3. Use UV sterilization for 15-30 minutes before and after hood use if sterile environment is extremely important. This is not always necessary, but should be done on occasion, and when sterile environment is especially important.
4. Do not disrupt airflow near incubator or in the hood. Use slow controlled motions. Do not cough, sneeze, or breathe in the direction of the hood or incubator. Hold your breath when the incubator door is open.
5. Spray down aspiration tube with ethanol after use to prevent bacterial growth inside the tube.
6. Disinfect the waste-flask with bleach and empty regularly.
7. Check cell cultures for bacteria and mycoplasma regularly.
8. Never use “cloudy” media. Turbidity indicates contamination.
9. Disinfect and clean all biological spills.
10. Do not store general lab supplies in the hood.
11. Label and date all cell cultures and supplies.
12. Leave things cleaner than you found them.

C.2.2 Media Preparation

1. Warm 500mL of media, 50mL of FBS, and 5mL of antibiotics in a water bath.
2. Remove 50mL of media. Add 50 mL of FBS and 5mL of antibiotics. The removed 50mL may be discarded or saved for future use.
3. Prior to first use you may want to UV-sterilize media for 30 minutes. I have had previous issues with purchased media having antibiotic-resistant bacterial contamination that ruined my cultures for several weeks.

C.2.3 Starting a Culture

1. Retrieve frozen culture from cold storage. Wear PPE to avoid skin or eye contact with liquid nitrogen.
2. Hold frozen culture in warm water bath for 30-60s. Do not submerge the cap. Wear eye protection, the rapid temperature change can sometimes result in a splash of liquid nitrogen being ejected from the cryotube.
3. Transfer cell solution to a 15mL tube using a serological pipette. Slowly add warmed cell culture media one drop at a time to prevent thermal shock of the cells. Add media until there is ~10mL in the tube.
4. Centrifuge the cell solution at 3000-4000 rpm for 3-4 minutes.

5. Aspirate the supernatant, avoiding the pellet of cells at the bottom of the tube.
6. Resuspend the cells in warmed cell culture media and transfer to a cell culture flask.
7. Incubate overnight, and change the media the following day.

C.2.4 Splitting Cells

1. Remove media and rinse cell flask twice with 5ml of PBS1X without calcium and magnesium. These ions interfere with Trypsin activity.
2. Remove PBS and add 5mL of 0.25% warmed Trypsin EDTA solution. Incubate for 5 minutes. Note that extended exposure to Trypsin will result in cell death.
3. Ensure that all cells are detached from the surface with the inverted microscope.
4. Add 5mL of cell culture media. Ions in the cell culture media will inactivate the Trypsin. Transfer the suspension of cells to a 15mL tube and centrifuge at 3000-4000 rpm for 3-4 minutes.
5. Aspirate the supernatant and resuspend cells in warmed cell culture media.
6. Transfer cell solution to a new flask with cell culture media. Cells are typically split 1:10 or 1:20. The ratio at which cells are split is dependent on cell line and desired seed density. This can be calculated

using a cytometer and measuring how much of the cell suspension is transferred to the new flask using a micropipette.

7. An easy way to split cells is based on drops of solution. A typical water droplet is 1/16th of a mL. So from a confluent cell culture, a single droplet from 1mL of cell suspension will be a 1:16 split. This is not as accurate and should not be used for more controlled biological studies.
8. Change cell media the following day. Splitting cells is stressful to cells and many will die, changing the media eliminates contamination of the culture with dead cell waste.

C.2.5 Freezing Cells

1. Prepare freezing media, consisting of cell media with 10%FBS and 10%DMSO, no antibiotics. DMSO is a cryopreservant. It is damaging to cells at normal temperatures.
2. Perform a normal cell splitting procedure, however resuspend cells in freezing media, rather than regular cell culture media.
3. Aliquot cell suspension with DMSO to cryotubes.
4. Place these cryotubes into cold storage either in a -80^{o} C freezer, or liquid nitrogen tanks. Some people will recommend freezing cells incrementally, first placing them in a freezer at -20^{o} C, and then moving them to -80^{o} C. My experience is that going directly to -80^{o} C works just as well.

Bibliography

Actis, P., Mak, A. C., & Pourmand, N. (2010). Functionalized nanopipettes: toward label-free, single cell biosensors. *Bioanal Rev, 1*(2-4), 177-185. doi: 10.1007/s12566-010-0013-y

Adamo, A., & Jensen, K. F. (2008). Microfluidic based single cell microinjection. *Lab on a Chip, 8*(8), 1258-1261. doi: 10.1039/b803212b

Adams, K. L., Puchades, M., & Ewing, A. G. (2008). In Vitro Electrochemistry of Biological Systems. *Annu Rev Anal Chem (Palo Alto Calif), 1*, 329. doi: 10.1146/annurev.anchem.1.031207.113038

Alberts, B., Bray, D., Hopkin, K., Johnson, A., Lewis, J., Raff, M., . . . Walter, P. (2013). *Essential Cell Biology, Fourth Edition*: Taylor & Francis Group.

Alberts, B., Johnson, A., Lewis, J., Raff, M., Roberts, K., & Walter, P. (2007). *Molecular Biology of the Cell*: Taylor & Francis Group.

Amatore, C., Arbault, S., Bouton, C., Coffi, K., Drapier, J. C., Ghandour, H., & Tong, Y. (2006). Monitoring in real time with a microelectrode the release of reactive oxygen and nitrogen species by a single macrophage stimulated by its membrane mechanical depolarization. *Chembiochem, 7*(4), 653-661. doi: 10.1002/cbic.200500359

Amemiya, S., Bard, A. J., Fan, F. R. F., Mirkin, M. V., & Unwin, P. R. (2008). Scanning Electrochemical Microscopy. *Annual Review of Analytical Chemistry, 1*, 95-131. doi: Doi 10.1146/Annurev.Anchem.1.031207.112938

Anderson, S. E., & Bau, H. H. (2014). Electrical detection of cellular penetration during microinjection with carbon nanopipettes. *Nanotechnology, 25*(24). doi: Artn 245102
Doi 10.1088/0957-4484/25/24/245102

Anderson, S. E., & Bau, H. H. (2015). Carbon Nanoelectrodes for Single-Cell Probing. *Nanotechnology, 26*, 185101. doi: 10.1088/0957-4484/26/18/185101

Ansorge, W., & Pepperkok, R. (1988). Performance of an Automated-System for Capillary Microinjection into Living Cells. *Journal of Biochemical and Biophysical Methods, 16*(4), 283-292. doi: Doi 10.1016/0165-022x(88)90062-0

Arbuthnott, G. W., & Wickens, J. (2007). Space, time and dopamine. *Trends in neurosciences, 30*(2), 62-69.

Babcock, H. P., Chen, C., & Zhuang, X. (2004). Using single-particle tracking to study nuclear trafficking of viral genes. *Biophysical Journal, 87*(4), 2749-2758. doi: 10.1529/biophysj.104.042234

Bard, A. J., & Faulkner, L. R. (2000). *Electrochemical Methods: Fundamentals and Applications*: Wiley.

Barhoom, S., Farrell, I., Shai, B., Dahary, D., Cooperman, B. S., Smilansky, Z., . . . Ehrlich, M. (2013). Dicodon monitoring of protein synthesis (DiCoMPS) reveals levels of synthesis of a viral protein in single cells. *Nucleic Acids Research, 41*(18). doi: UNSP e177
DOI 10.1093/nar/gkt686

Barhoom, S., Kaur, J., Cooperman, B. S., Smorodinsky, N. I., Smilansky, Z., Ehrlich, M., & Elroy-Stein, O. (2011). Quantitative single cell monitoring of protein synthesis at subcellular resolution using fluorescently labeled tRNA. *Nucleic Acids Research, 39*(19). doi: ARTN e129
DOI 10.1093/nar/gkr601

Bath, B. D., Michael, D. J., Trafton, B. J., Joseph, J. D., Runnels, P. L., & Wightman, R. M. (2000). Subsecond adsorption and desorption of dopamine at carbon-fiber microelectrodes. *Analytical Chemistry, 72*(24), 5994-6002. doi: 10.1021/ac000849y

Becattini, G., Mattos, L. S., & Caldwell, D. G. (2014). A fully automated system for adherent cells microinjection. *IEEE J Biomed Health Inform, 18*(1), 83-93. doi: 10.1109/jbhi.2013.2248161

Berg, J. C. (2010). *An Introduction to Interfaces & Colloids: The Bridge to Nanoscience*: World Scientific.

Bergner, S., Vatsyayan, P., & Matysik, F. M. (2013). Recent advances in high resolution scanning electrochemical microscopy of living cells - A review. *Analytica Chimica Acta, 775*, 1-13. doi: Doi 10.1016/J.Aca.2012.12.042

Betteridge, T., Liu, H., Gamper, H., Kirillov, S., Cooperman, B. S., & Hou, Y. M. (2007). Fluorescent labeling of tRNAs for dynamics experiments. *Rna-a Publication of the Rna Society, 13*(9), 1594-1601. doi: Doi 10.1261/Rna.475407

Birakayala, N., & Evans, E. A. (2002). A reduced reaction model for carbon CVD/CVI processes. *Carbon, 40*(5), 675-683.
Borue, X., Cooper, S., Hirsh, J., Condron, B., & Venton, B. J. (2009). Quantitative evaluation of serotonin release and clearance in Drosophila. *Journal of Neuroscience Methods, 179*(2), 300-308. doi: Doi 10.1016/J.Jneumeth.2009.02.013

Brennan, L. D., Roland, T., Morton, D. G., Fellman, S. M., Chung, S. Y., Soltani, M., . . . Wang, M. D. (2013). Small Molecule Injection into Single-Cell C. elegans Embryos via Carbon-Reinforced Nanopipettes. *Plos One, 8*(9). doi: ARTN e75712
DOI 10.1371/journal.pone.0075712

Brown, K. T., & Flaming, D. G. (1986). *Advanced micropipette techniques for cell physiology*: Wiley.

Cahill, P. S., Walker, Q. D., Finnegan, J. M., Mickelson, G. E., Travis, E. R., & Wightman, R. M. (1996). Microelectrodes for the measurement of catecholamines in biological systems. *Analytical Chemistry, 68*(18), 3180-3186. doi: Doi 10.1021/Ac960347d

Campbell, J. K., Sun, L., & Crooks, R. M. (1999). Electrochemistry using single carbon nanotubes. *Journal of the American Chemical Society, 121*(15), 3779-3780.
Chadchankar, H., & Yavich, L. (2012). Characterization of a 32 μ m diameter carbon fiber electrode for in vivo fast-scan cyclic voltammetry. *Journal of Neuroscience Methods, 211*(2), 218-226. doi: http://dx.doi.org/10.1016/j.jneumeth.2012.09.011

Charrier, A., Martinez, D., Monette, R., Comas, T., Movileanu, R., Py, C., . . . Mealing, G. (2010). Cell Placement and Guidance on Substrates for Neurochip Interfaces. *Biotechnology and Bioengineering, 105*(2), 368-373.

Chen, P., & Gillis, K. D. (2000). The noise of membrane capacitance measurements in the whole-cell recording configuration. *Biophysical Journal, 79*(4), 2162-2170.

Chen, S., & Kucernak, A. (2002). Fabrication of carbon microelectrodes with an effective radius of 1 nm. *Electrochemistry communications, 4*(1), 80-85.

Cooper, S. E., & Venton, B. J. (2009). Fast-scan cyclic voltammetry for the detection of tyramine and octopamine. *Analytical and Bioanalytical Chemistry, 394*(1), 329-336. doi: Doi 10.1007/S00216-009-2616-0

Delivopoulos, E., Murray, A. F., MacLeod, N. K., & Curtis, J. C. (2009). Guided growth of neurons and glia using microfabricated patterns of parylene-C on a SiO2 background. *Biomaterials, 30*(11), 2048-2058. doi: Doi 10.1016/J.Biomaterials.2008.12.049

Esmaeilsabzali, H., Sakaki, K., Dechev, N., Burke, R. D., & Park, E. J. (2012). Machine vision-based localization of nucleic and cytoplasmic injection sites on low-contrast adherent cells. *Med Biol Eng Comput, 50*(1), 11-21. doi: 10.1007/s11517-011-0831-2

Fernandez-Suarez, M., & Ting, A. Y. (2008). Fluorescent probes for super-resolution imaging in living cells. *Nat Rev Mol Cell Biol, 9*(12), 929-943.

Fritzsch, F. S., Dusny, C., Frick, O., & Schmid, A. (2012). Single-cell analysis in biotechnology, systems biology, and biocatalysis. *Annu Rev Chem Biomol Eng, 3*, 129-155. doi: 10.1146/annurev-chembioeng-062011-081056

Geddes, L. A. (1972). *Electrodes and the measurement of bioelectric events*: Wiley-Interscience.

Gehl, J. (2003). Electroporation: theory and methods, perspectives for drug delivery, gene therapy and research. *Acta Physiol Scand, 177*(4), 437-447. doi: 10.1046/j.1365-201X.2003.01093.x

Gillis, K. D. (2000). Admittance-based measurement of membrane capacitance using the EPC-9 patch-clamp amplifier. *Pflugers Archiv-European Journal of Physiology, 439*(5), 655-664. doi: Doi 10.1007/S004240050990

Hamill, O. P., Marty, A., Neher, E., Sakmann, B., & Sigworth, F. J. (1981). Improved Patch-Clamp Techniques for High-Resolution Current Recording from Cells and Cell-Free Membrane Patches. *Pflugers Archiv-European Journal of Physiology, 391*(2), 85-100. doi: Doi 10.1007/Bf00656997

Heien, M. L., Phillips, P. E., Stuber, G. D., Seipel, A. T., & Wightman, R. M. (2003). Overoxidation of carbon-fiber microelectrodes enhances dopamine adsorption and increases sensitivity. *Analyst, 128*(12), 1413-1419.

Heller, I., Kong, J., Heering, H. A., Williams, K. A., Lemay, S. G., & Dekker, C. (2005). Individual single-walled carbon nanotubes as nanoelectrodes for electrochemistry. *Nano Letters, 5*(1), 137-142.

Hopper, A. K. (2013). Transfer RNA Post-Transcriptional Processing, Turnover, and Subcellular Dynamics in the Yeast Saccharomyces cerevisiae. *Genetics, 194*(1), 43-67. doi: Doi 10.1534/Genetics.112.147470

Hopper, A. K., & Shaheen, H. H. (2008). A decade of surprises for tRNA nuclear-cytoplasmic dynamics. *Trends in Cell Biology, 18*(3), 98-104. doi: Doi 10.1016/J.Tcb.2008.01.001

Hou, Y. M., & Yang, X. L. (2013). Regulation of Cell Death by Transfer RNA. *Antioxidants & Redox Signaling, 19*(6), 583-594. doi: Doi 10.1089/Ars.2012.5171

Hu, K. K., Gao, Y., Wang, Y. X., Yu, Y., Zhao, X., Rotenberg, S. A., . . . Gogotsi, Y. (2013). Platinized carbon nanoelectrodes as potentiometric and amperometric SECM probes. *Journal of Solid State Electrochemistry, 17*(12), 2971-2977. doi: Doi 10.1007/S10008-013-2173-5

Huang, H. Y., & Hopper, A. K. (2014). Separate responses of karyopherins to glucose and amino acid availability regulate nucleocytoplasmic transport. *Molecular Biology of the Cell, 25*(18), 2840-2852. doi: Doi 10.1091/Mbc.E14-04-0948

Huang, W.-H., Pang, D.-W., Tong, H., Wang, Z.-L., & Cheng, J.-K. (2001). A Method for the Fabrication of Low-Noise Carbon Fiber Nanoelectrodes. *Analytical Chemistry, 73*(5), 1048-1052. doi: 10.1021/ac0008183

Huang, W. H., Pang, D. W., Tong, H., Wang, Z. L., & Cheng, J. K. (2001). A method for the fabrication of low-noise carbon fiber nanoelectrodes. *Analytical Chemistry, 73*(5), 1048-1052. doi: Doi 10.1021/Ac0008183

Huffman, M. L., & Venton, B. J. (2008). Electrochemical Properties of Different Carbon-Fiber Microelectrodes Using Fast-Scan Cyclic Voltammetry. *Electroanalysis, 20*(22), 2422-2428. doi: Doi 10.1002/Elan.200804343

Hughes, L. D., Rawle, R. J., & Boxer, S. G. (2014). Choose Your Label Wisely: Water-Soluble Fluorophores Often Interact with Lipid Bilayers. *Plos One, 9*(2), e87649. doi: 10.1371/journal.pone.0087649

Hunt, T. P., Issadore, D., & Westervelt, R. M. (2008). Integrated circuit/microfluidic chip to programmably trap and move cells and droplets with dielectrophoresis. *Lab on a Chip, 8*(1), 81-87. doi: 10.1039/b710928h

Ilegems, E., Pick, H. M., & Vogel, H. (2002). Monitoring mis-acylated tRNA suppression efficiency in mammalian cells via EGFP fluorescence recovery. *Nucleic Acids Research, 30*(23), e128-e128.

Image Aquisition Toolbox. (2015). Retrieved April 20th, 2015, from http://www.mathworks.com/products/imaq/

Jackson, B. P., Dietz, S. M., & Wightman, R. M. (1995). Fast-scan cyclic voltammetry of 5-hydroxytryptamine. *Analytical Chemistry, 67*(6), 1115-1120.

Jacobs, C. B., Vickrey, T. L., & Venton, B. J. (2011). Functional groups modulate the sensitivity and electron transfer kinetics of neurochemicals at carbon nanotube modified microelectrodes. *Analyst, 136*(17), 3557-3565. doi: Doi 10.1039/C0an00854k

Johnson, S. L., & Woodbury, J. W. (1964). Membrane Resistance of Human Red Cells. *Journal of General Physiology, 47*(5), 827-&. doi: Doi 10.1085/Jgp.47.5.827

Joy, D. C., & Joy, C. S. (1996). Low voltage scanning electron microscopy. *Micron, 27*(3), 247-263.

Kahsai, L., & Winther, Å. M. E. (2011). Chemical neuroanatomy of the Drosophila central complex: Distribution of multiple neuropeptides in relation to neurotransmitters. *The Journal of Comparative Neurology, 519*(2), 290-315. doi: 10.1002/cne.22520

Kallio, P., Ritala, T., Lukkari, M., & Kuikka, S. (2007). Injection guidance system for cellular microinjections. *International Journal of Robotics Research, 26*(11--12), 1303-1313. doi: Doi 10.1177/0278364907084985

Kang, W. M., Yavari, F., Minary-Jolandan, M., Giraldo-Vela, J. P., Safi, A., McNaughton, R. L., . . . Espinosa, H. D. (2013). Nanofountain Probe Electroporation (NFP-E) of Single Cells. *Nano Letters, 13*(6), 2448-2457. doi: Doi 10.1021/Nl400423c

Katz, E., & Willner, I. (2003). Probing biomolecular interactions at conductive and semiconductive surfaces by impedance spectroscopy: Routes to impedimetric immunosensors, DNA-Sensors, and enzyme biosensors. *Electroanalysis, 15*(11), 913-947. doi: Doi 10.1002/Elan.200390114

Kawagoe, K. T., Jankowski, J. A., & Wightman, R. M. (1991). Etched carbon-fiber electrodes as amperometric detectors of catecholamine secretion from isolated biological cells. *Analytical Chemistry, 63*(15), 1589-1594. doi: 10.1021/ac00015a017

Khine, M., Ionescu-Zanetti, C., Blatz, A., Wang, L. P., & Lee, L. P. (2007). Single-cell electroporation arrays with real-time monitoring and feedback control. *Lab on a Chip, 7*(4), 457-462. doi: Doi 10.1039/B614356c

Kim, B. M., Murray, T., & Bau, H. H. (2005). The fabrication of integrated carbon pipes with sub-micron diameters. *Nanotechnology, 16*(8), 1317-1320. doi: Doi 10.1088/0957-4484/16/8/056

Klapoetke, N. C., Murata, Y., Kim, S. S., Pulver, S. R., Birdsey-Benson, A., Cho, Y. K., . . . Tian, Z. (2014). Independent optical excitation of distinct neural populations. *Nat Methods, 11*(3), 338-346.

Kodandaramaiah, S. B., Franzesi, G. T., Chow, B. Y., Boyden, E. S., & Forest, C. R. (2012). Automated whole-cell patch-clamp electrophysiology of neurons in vivo. *Nat Methods, 9*(6), 585-587. doi: 10.1038/nmeth.1993

Koehne, J. E., Marsh, M., Boakye, A., Douglas, B., Kim, I. Y., Chang, S.-Y., . . . Andrews, R. (2011). Carbon nanofiber electrode array for electrochemical detection of dopamine using fast scan cyclic voltammetry. *Analyst, 136*(9), 1802-1805.

Kramer, E. B., & Hopper, A. K. (2013). Retrograde transfer RNA nuclear import provides a new level of tRNA quality control in Saccharomyces cerevisiae. *Proceedings of the National Academy of Sciences of the United States of America, 110*(52), 21042-21047. doi: Doi 10.1073/Pnas.1316579110

Lau, A. Y., Hung, P. J., Wu, A. R., & Lee, L. P. (2006). Open-access microfluidic patch-clamp array with raised lateral cell trapping sites. *Lab on a Chip, 6*(12), 1510-1515. doi: Doi 10.1039/B608439g

Li, A., Norinaga, K., Zhang, W. G., & Deutschmann, O. (2008). Modeling and simulation of materials synthesis: Chemical vapor deposition and infiltration of pyrolytic carbon. *Composites Science and Technology, 68*(5), 1097-1104. doi: Doi 10.1016/J.Compscitech.2007.07.00

Lin, Y. Q., Trouillon, R., Svensson, M. I., Keighron, J. D., Cans, A. S., & Ewing, A. G. (2012). Carbon-Ring Microelectrode Arrays for Electrochemical Imaging of Single Cell

Exocytosis: Fabrication and Characterization. *Analytical Chemistry, 84*(6), 2949-2954. doi: Doi 10.1021/Ac3000368

Lindau, M., & Neher, E. (1988). Patch-Clamp Techniques for Time-Resolved Capacitance Measurements in Single Cells. *Pflugers Archiv-European Journal of Physiology, 411*(2), 137-146. doi: Doi 10.1007/Bf00582306

Liu, C., Sun, T., Zhai, Y., & Dong, S. (2009). Evaluation of ferricyanide effects on microorganisms with multi-methods. *Talanta, 78*(2), 613-617. doi: 10.1016/j.talanta.2008.12.019

Lukkari, M., & Kallio, P. (2005, 27-30 June 2005). *Multi-purpose impedance-based measurement system to automate microinjection of adherent cells.* Paper presented at the Computational Intelligence in Robotics and Automation, 2005. CIRA 2005. Proceedings. 2005 IEEE International Symposium on.

Lützenkirchen, J. (2006). Parsons–Zobel plots: An independent way to determine surface complexation parameters? *Journal of Colloid and Interface Science, 303*(1), 214-223. doi: http://dx.doi.org/10.1016/j.jcis.2006.07.037

Makos, M. A., Han, K.-A., Heien, M. L., & Ewing, A. G. (2009). Using in Vivo Electrochemistry To Study the Physiological Effects of Cocaine and Other Stimulants on the Drosophila melanogaster Dopamine Transporter. *Acs Chemical Neuroscience, 1*(1), 74-83. doi: 10.1021/cn900017w

Makos, M. A., Kim, Y.-C., Han, K.-A., Heien, M. L., & Ewing, A. G. (2009). In Vivo Electrochemical Measurements of Exogenously Applied Dopamine in Drosophila melanogaster. *Analytical Chemistry, 81*(5), 1848-1854. doi: 10.1021/ac802297b

Mao, Z., & Davis, R. L. (2009). Eight Different Types of Dopaminergic Neurons Innervate the Drosophila Mushroom Body Neuropil: Anatomical and Physiological Heterogeneity. *Frontiers in Neural Circuits, 3*, 5. doi: 10.3389/neuro.04.005.2009

Matsuoka, H., Komazaki, T., Mukai, Y., Shibusawa, M., Akane, H., Chaki, A., . . . Saito, M. (2005). High throughput easy microinjection with a single-cell manipulation supporting robot. *J Biotechnol, 116*(2), 185-194. doi: 10.1016/j.jbiotec.2004.10.010

Mattos, L. S., Grant, E., Thresher, R., & Kluckman, K. (2009). Blastocyst Microinjection Automation. *Ieee Transactions on Information Technology in Biomedicine, 13*(5), 822-831. doi: Doi 10.1109/Titb.2009.2023664

McCreery, R. L. (2008). Advanced carbon electrode materials for molecular electrochemistry. *Chem. Rev, 108*(7), 2646-2687.

Mei, Y. D., Stonestrom, A., Hou, Y. M., & Yang, X. L. (2010). Apoptotic regulation and tRNA. *Protein & Cell, 1*(9), 795-801. doi: Doi 10.1007/S13238-010-0107-X

Mei, Y. D., Yong, J., Liu, H. T., Shi, Y. G., Meinkoth, J., Dreyfuss, G., & Yang, X. L. (2010). tRNA Binds to Cytochrome c and Inhibits Caspase Activation. *Molecular Cell, 37*(5), 668-678. doi: Doi 10.1016/J.Molcel.2010.01.023

Mei, Y. D., Yong, J. S., Stonestrom, A., & Yang, X. L. (2010). tRNA and cytochrome c in cell death and beyond. *Cell Cycle, 9*(15), 2936-2939. doi: Doi 10.4161/Cc.9.15.12316

Mellander, L., Cans, A. S., & Ewing, A. G. (2010). Electrochemical Probes for Detection and Analysis of Exocytosis and Vesicles. *Chemphyschem, 11*(13), 2756-2763. doi: Doi 10.1002/Cphc.201000258

Meyer, M. W., & Smith, E. A. (2011). Optimization of silver nanoparticles for surface enhanced Raman spectroscopy of structurally diverse analytes using visible and near-infrared excitation. *Analyst, 136*(17), 3542-3549. doi: Doi 10.1039/C0an00851f

Michelakis, E. D., Webster, L., & Mackey, J. R. (2008). Dichloroacetate (DCA) as a potential metabolic-targeting therapy for cancer. *Br J Cancer, 99*(7), 989-994.

Minaschek, G., Bereiterhahn, J., & Bertholdt, G. (1989). Quantitation of the Volume of Liquid Injected into Cells by Means of Pressure. *Experimental Cell Research, 183*(2), 434-442. doi: Doi 10.1016/0014-4827(89)90402-3

Murthi, A., Shaheen, H. H., Huang, H. Y., Preston, M. A., Lai, T. P., Phizicky, E. M., & Hopper, A. K. (2010). Regulation of tRNA Bidirectional Nuclear-Cytoplasmic Trafficking in Saccharomyces cerevisiae. *Molecular Biology of the Cell, 21*(4), 639-649. doi: Doi 10.1091/Mbc.E09-07-0551

Nagai, M., Torimoto, T., Miyamoto, T., Kawashima, T., & Shibata, T. (2013). Electrokinetic Delivery of Biomolecules into Living Cells for Analysis of Cellular Regulation. *Japanese Journal of Applied Physics, 52*(4R), 047002.

Navidi, W. (2008). *Statistics for Engineers and Scientists*: McGraw-Hill Education.

Nebel, M., Grutzke, S., Diab, N., Schulte, A., & Schuhmann, W. (2013). Microelectrochemical visualization of oxygen consumption of single living cells. *Faraday Discussions, 164*, 19-32. doi: Doi 10.1039/C3fd00011g

Nguyen, M. D., Lee, S. T., Ross, A. E., Ryals, M., Choudhry, V. I., & Venton, B. J. (2014). Characterization of Spontaneous, Transient Adenosine Release in the Caudate-Putamen and Prefrontal Cortex. *Plos One, 9*(1). doi: ARTN e87165

DOI 10.1371/journal.pone.0087165

Norinaga, K., & Deutschmann, O. (2007). Detailed kinetic modeling of gas-phase reactions in the chemical vapor deposition of carbon from light hydrocarbons. *Industrial & Engineering Chemistry Research, 46*(11), 3547-3557.

Paterson, L., Agate, B., Comrie, M., Ferguson, R., Lake, T., Morris, J., . . . Dholakia, K. (2005). Photoporation and cell transfection using a violet diode laser. *Opt Express, 13*(2), 595-600.

Pavon-Eternod, M., Gomes, S., Geslain, R., Dai, Q., Rosner, M. R., & Pan, T. (2009). tRNA over-expression in breast cancer and functional consequences. *Nucleic Acids Research, 37*(21), 7268-7280. doi: 10.1093/nar/gkp787

Pillarisetti, A., Pekarev, M., Brooks, A. D., & Desai, J. P. (2007). Evaluating the effect of force feedback in cell injection. *Ieee Transactions on Automation Science and Engineering, 4*(3), 322-331. doi: Doi 10.1109/Tase.2006.888051

Polk, B. J., Stelzenmuller, A., Mijares, G., MacCrehan, W., & Gaitan, M. (2006). Ag/AgCl microelectrodes with improved stability for microfluidics. *Sensors and Actuators B-Chemical, 114*(1), 239-247. doi: Doi 10.1016/J.Snb.2005.03.121

Potter, H., & Heller, R. (2010). Transfection by electroporation. *Curr Protoc Mol Biol, Chapter 9*, Unit9 3. doi: 10.1002/0471142727.mb0903s92

Potts, R. O., Ford, N. C., Jr., & Fournier, M. J. (1981). Changes in the solution structure of yeast phenylalanine transfer ribonucleic acid associated with aminoacylation and magnesium binding. *Biochemistry, 20*(6), 1653-1659.

Probstein, R. F., & Brenner, H. (2013). *Physicochemical Hydrodynamics: An Introduction*: Elsevier Science.

Qi, C., & Anderson, S. E. (2015, April 10th, 2015). GitHub - Matlab-based Semi-automated Injection System. Retrieved 4/21/2015, from https://github.com/seanderson12/2015_04_21-AutoInj_GUI

Randviir, E. P., & Banks, C. E. (2013). Electrochemical impedance spectroscopy: an overview of bioanalytical applications. *Analytical Methods, 5*(5), 1098-1115. doi: Doi 10.1039/C3ay26476a

Rees, H. R., Anderson, S. E., Privman, E., Bau, H. H., & Venton, B. J. (2015). Carbon nanopipette electrodes for dopamine detection in Drosophila. *Analytical Chemistry*. doi: 10.1021/ac504596y

Robinson, D. L., Hermans, A., Seipel, A. T., & Wightman, R. M. (2008). Monitoring Rapid Chemical Communication in the Brain. *Chemical reviews, 108*(7), 2554-2584. doi: 10.1021/cr068081q

Rubio, M. A. T., & Hopper, A. K. (2011). Transfer RNA travels from the cytoplasm to organelles. *Wiley Interdisciplinary Reviews-Rna, 2*(6), 802-817. doi: Doi 10.1002/Wrna.93

Sakaki, K., Esmaeilsabzali, H., Dechev, N., Burke, R. D., & Park, E. J. (2012). A Generalized Tip-Membrane Contact Detection Algorithm for Automated Single Cell Electroporation Using Statistical Process Control. *Automation Science and Engineering, IEEE Transactions on, 9*(2), 226-236. doi: 10.1109/TASE.2012.2188027

Satpati, A. K., & Bard, A. J. (2012). Preparation and Characterization of Carbon Powder Paste Ultramicroelectrodes as Tips for Scanning Electrochemical Microscopy Applications. *Analytical Chemistry, 84*(21), 9498-9504.

Schrlau, M. G. (2009). *CARBON-BASED NANOPROBES FOR CELL NANOSURGERY & BIOLOGICAL APPLICATIONS*. (Ph.D.), University of Pennsylvania.

Schrlau, M. G., & Bau, H. H. (2009). Carbon-based nanoprobes for cell biology. *Microfluidics and Nanofluidics, 7*(4), 439-450. doi: Doi 10.1007/S10404-009-0458-X

Schrlau, M. G., Brailoiu, E., Patel, S., Gogotsi, Y., Dun, N. J., & Bau, H. H. (2008). Carbon nanopipettes characterize calcium release pathways in breast cancer cells. *Nanotechnology, 19*(32). doi: Artn 325102
Doi 10.1088/0957-4484/19/32/325102

Schrlau, M. G., Dun, N. J., & Bau, H. H. (2009). Cell Electrophysiology with Carbon Nanopipettes. *Acs Nano, 3*(3), 563-568. doi: Doi 10.1021/Nn800851d

Schrlau, M. G., Falls, E. M., Ziober, B. L., & Bau, H. H. (2008). Carbon nanopipettes for cell probes and intracellular injection. *Nanotechnology, 19*(1). doi: Artn 015101
Doi 10.1088/0957-4484/19/01/015101

Shan, J., Lang, D., & Dimotakis, P. (2004). Scalar concentration measurements in liquid-phase flows with pulsed lasers. *Experiments in Fluids, 36*(2), 268-273. doi: 10.1007/s00348-003-0717-7

Sharei, A., Zoldan, J., Adamo, A., Sim, W. Y., Cho, N., Jackson, E., . . . Jensen, K. F. (2013). A vector-free microfluidic platform for intracellular delivery. *Proceedings of the National Academy of Sciences, 110*(6), 2082-2087. doi: 10.1073/pnas.1218705110

Simon, A. J., Vallee-Belisle, A., Ricci, F., Watkins, H. M., & Plaxco, K. W. (2014). Principles for the Rational Design of Allosterically Cooperative Biomolecular Receptors. *Biophysical Journal, 106*(2), 614A-614A.

Singhal, R., Bhattacharyya, S., Orynbayeva, Z., Vitol, E., Friedman, G., & Gogotsi, Y. (2010). Small diameter carbon nanopipettes. *Nanotechnology, 21*(1). doi: Artn 015304
Doi 10.1088/0957-4484/21/1/015304

Singhal, R., Orynbayeva, Z., Sundaram, R. V. K., Niu, J. J., Bhattacharyya, S., Vitol, E. A., . . . Gogotsi, Y. (2011). Multifunctional carbon-nanotube cellular endoscopes. *Nature Nanotechnology, 6*(1), 57-64. doi: Doi 10.1038/Nnano.2010.241

Stevenson, D. J., Gunn-Moore, F. J., Campbell, P., & Dholakia, K. (2010). Single cell optical transfection. *Journal of the Royal Society Interface, 7*(47), 863-871. doi: Doi 10.1098/Rsif.2009.0463

Strand, A. M., & Venton, B. J. (2008). Flame etching enhances the sensitivity of carbon-fiber microelectrodes. *Analytical Chemistry, 80*(10), 3708-3715. doi: Doi 10.1021/Ac8001275

Strein, T. G., & Ewing, A. G. (1992). Characterization of submicron-sized carbon electrodes insulated with a phenol-allylphenol copolymer. *Analytical Chemistry, 64*(13), 1368-1373. doi: 10.1021/ac00037a012

Sun, P., Laforge, F. O., Abeyweera, T. P., Rotenberg, S. A., Carpino, J., & Mirkin, M. V. (2008). Nanoelectrochemistry of mammalian cells. *Proceedings of the National Academy of Sciences of the United States of America, 105*(2), 443-448. doi: Doi 10.1073/Pnas.0711075105

Sun, P., Laforge, F. O., & Mirkin, M. V. (2007). Scanning electrochemical microscopy in the 21st century. *Physical Chemistry Chemical Physics, 9*(7), 802-823. doi: Doi 10.1039/B612259k

Takmakov, P., Zachek, M. K., Keithley, R. B., Walsh, P. L., Donley, C., McCarty, G. S., & Wightman, R. M. (2010). Carbon microelectrodes with a renewable surface. *Analytical Chemistry, 82*(5), 2020-2028. doi: 10.1021/ac902753x

Takmakov, P., Zachek, M. K., Keithley, R. B., Walsh, P. L., Donley, C., McCarty, G. S., & Wightman, R. M. (2010). Carbon microelectrodes with a renewable surface. *Analytical Chemistry, 82*(5), 2020-2028.

Tan, K. K., Huang, S., & Tang, K. Z. (2009). Robust computer-controlled system for intracytoplasmic sperm injection and subsequent cell electro-activation. *International Journal of Medical Robotics and Computer Assisted Surgery, 5*(1), 85-98. doi: Doi 10.1002/Rcs.239

Thompson, J. A., & Bau, H. H. (2012). Porous bead-based microfluidic assay: theory and confocal microscope imaging. *Microfluidics and Nanofluidics, 12*(1-4), 625-637. doi: Doi 10.1007/S10404-011-0904-4

Trasatti, S., & Petrii, O. A. (1992). Real Surface-Area Measurements in Electrochemistry. *Journal of Electroanalytical Chemistry, 327*(1-2), 353-376. doi: Doi 10.1016/0022-0728(92)80162-W

Tuller, T. (2012). The Effect of Dysregulation of tRNA Genes and Translation Efficiency Mutations in Cancer and Neurodegeneration. *Front Genet, 3*, 201. doi: 10.3389/fgene.2012.00201

Venton, B. J., & Wightman, R. M. (2003). Psychoanalytical electrochemistry: Dopamine and behavior. *Analytical Chemistry, 75*(19), 414A-421A. doi: Doi 10.1021/Ac031421c

Vickrey, T. L., Condron, B., & Venton, B. J. (2009). Detection of Endogenous Dopamine Changes in Drosophila melanogaster Using Fast-Scan Cyclic Voltammetry. *Analytical Chemistry, 81*(22), 9306-9313. doi: Doi 10.1021/Ac901638z

Vickrey, T. L., & Venton, B. J. (2011). Drosophila Dopamine2-like Receptors Function as Autoreceptors. *Acs Chemical Neuroscience, 2*(12), 723-729. doi: Doi 10.1021/Cn200057k

Vihinen-Ranta, M., Yuan, W., & Parrish, C. R. (2000). Cytoplasmic Trafficking of the Canine Parvovirus Capsid and Its Role in Infection and Nuclear Transport. *Journal of Virology, 74*(10), 4853-4859.

Vitol, E. A., Schrlau, M. G., Bhattacharyya, S., Ducheyne, P., Bau, H. H., Friedman, G., & Gogotsi, Y. (2009). Effects of Deposition Conditions on the Structure and Chemical Properties of Carbon Nanopipettes. *Chemical Vapor Deposition, 15*(7-9), 204-208. doi: Doi 10.1002/Cvde.200906784

Voldman, J. (2006). Electrical forces for microscale cell manipulation. *Annual Review of Biomedical Engineering, 8*, 425-454. doi: Doi 10.1146/Annurev.Bioeng.8.061505.095739

Wang, C., Chen, Y., Wang, F., & Hu, X. (2005). Fabrication of nanometer-sized carbon electrodes by the controllable electrochemical deposition. *Electrochimica Acta, 50*(28), 5588-5593. doi: http://dx.doi.org/10.1016/j.electacta.2005.03.031

Wang, D., & Bodovitz, S. (2010). Single cell analysis: the new frontier in 'omics'. *Trends Biotechnol, 28*(6), 281-290. doi: 10.1016/j.tibtech.2010.03.002

Wang, H. N., & Pilon, L. (2011). Accurate Simulations of Electric Double Layer Capacitance of Ultramicroelectrodes. *Journal of Physical Chemistry C, 115*(33), 16711-16719. doi: Doi 10.1021/Jp204498e

Wang, W., Zhang, S. H., Li, L. M., Wang, Z. L., Cheng, J. K., & Huang, W. H. (2009). Monitoring of vesicular exocytosis from single cells using micrometer and nanometer-sized electrochemical sensors. *Analytical and Bioanalytical Chemistry, 394*(1), 17-32. doi: Doi 10.1007/S00216-009-2703-2

Wang, W. H., Liu, X. Y., Gelinas, D., Ciruna, B., & Sun, Y. (2007). A Fully Automated Robotic System for Microinjection of Zebrafish Embryos. *Plos One, 2*(9). doi: ARTN e862
DOI 10.1371/journal.pone.0000862

Wang, W. H., Sun, Y., Zhang, M., Anderson, R., Langille, L., & Chan, W. (2008). A system for high-speed microinjection of adherent cells. *Review of Scientific Instruments, 79*(10). doi: Artn 104302
Doi 10.1063/1.3006000

Whitney, M. L., Hurto, R. L., Shaheen, H. H., & Hopper, A. K. (2007). Rapid and reversible nuclear accumulation of cytoplasmic tRNA in response to nutrient availability. *Molecular Biology of the Cell, 18*(7), 2678-2686. doi: Doi 10.1091/Mbc.E07-10-0006

Wightman, R. M., May, L. J., & Michael, A. C. (1988). Detection of Dopamine Dynamics in the Brain. *Analytical Chemistry, 60*(13), A769-&. doi: Doi 10.1021/Ac00164a001

Wong, P. K., Tan, W., & Ho, C. M. (2005). Cell relaxation after electrodeformation: effect of latrunculin A on cytoskeletal actin. *Journal of Biomechanics, 38*(3), 529-535. doi: Doi 10.1016/J.Jbiomech.2004.04.008

Xiao, N., Privman, E., & Venton, B. J. (2014). Optogenetic Control of Serotonin and Dopamine Release in Drosophila Larvae. *Acs Chemical Neuroscience, 5*(8), 666-673. doi: Doi 10.1021/Cn500044b

Xiao, N., & Venton, B. J. (2012). Rapid, Sensitive Detection of Neurotransmitters at Microelectrodes Modified with Self-assembled SWCNT Forests. *Analytical Chemistry, 84*(18), 7816-7822. doi: Doi 10.1021/Ac301445w

Xiao, Y., Uzawa, T., White, R. J., Demartini, D., & Plaxco, K. W. (2009). On the Signaling of Electrochemical Aptamer-Based Sensors: Collision- and Folding-Based Mechanisms. *Electroanalysis, 21*(11), 1267-1271. doi: 10.1002/elan.200804564

Xie, Y., Sun, D., Liu, C., Tse, H. Y., & Cheng, S. H. (2010). A Force Control Approach to a Robot-assisted Cell Microinjection System. *International Journal of Robotics Research, 29*(9), 1222-1232. doi: Doi 10.1177/0278364909354325

Yu, Y., Noel, J. M., Mirkin, M. V., Gao, Y., Mashtalir, O., Friedman, G., & Gogotsi, Y. (2014). Carbon Pipette-Based Electrochemical Nanosampler. *Analytical Chemistry, 86*(7), 3365-3372. doi: Doi 10.1021/Ac403547b

Zachek, M. K., Takmakov, P., Moody, B., Wightman, R. M., & McCarty, G. S. (2009). Simultaneous Decoupled Detection of Dopamine and Oxygen using Pyrolyzed Carbon Microarrays and FSCV. *Analytical Chemistry, 81*(15), 6258-6265. doi: 10.1021/ac900790m

Zaitseva, L., Myers, R., & Fassati, A. (2006). tRNAs promote nuclear import of HIV-1 intracellular reverse transcription complexes. *Plos Biology, 4*(10), e332. doi: 10.1371/journal.pbio.0040332

Zaliapin, I., Semenova, I., Kashina, A., & Rodionov, V. (2005). Multiscale Trend Analysis of Microtubule Transport in Melanophores. *Biophysical Journal, 88*(6), 4008-4016. doi: 10.1529/biophysj.104.057083

Zappe, S., Fish, M., Scott, M. P., & Solgaard, O. (2006). Automated MEMS-based Drosophila embryo injection system for high-throughput RNAi screens. *Lab on a Chip, 6*(8), 1012-1019. doi: Doi 10.1039/B600238b

Zestos, A. G., Nguyen, M. D., Poe, B. L., Jacobs, C. B., & Venton, B. J. (2013). Epoxy insulated carbon fiber and carbon nanotube fiber microelectrodes. *Sensors and Actuators B-Chemical, 182*, 652-658. doi: Doi 10.1016/J.Snb.2013.03.066

Zhao, Y., Butler, E., & Tan, M. (2013). Targeting cellular metabolism to improve cancer therapeutics. *Cell death & disease, 4*(3), e532.

Zhao, Y., Inayat, S., Dikin, D. A., Singer, J. H., Ruoff, R. S., & Troy, J. B. (2008). Patch clamp technique: Review of the current state of the art and potential contributions from nanoengineering. *Proceedings of the Institution of Mechanical Engineers, Part N: Journal of Nanoengineering and Nanosystems, 222*(1), 1-11. doi: 10.1243/17403499jnn149